Moving Beyond First Generation Radial Imaging:
3D Rosette-like Acquisition
for Improved Articular Cartilage Assessment

By

Larry Hernandez

A dissertation submitted in partial fulfillment of

the requirements for the degree of

Doctor of Philosophy

(Medical Physics)

at the

UNIVERSITY OF WISCONSIN-MADISON

2016

Date of Final Oral Examination: July 14, 2016

The dissertation is approved by the following members of the Final Oral Committee:
Walter F. Block, PhD, Professor, Medical Physics, Biomedical Engineering
Richard Kijowski, MD, Professor, Radiology
M. Elizabeth Meyerend, PhD Professor, Medical Physics, Biomedical Engineering
Oliver Wieben, PhD, Associate Professor, Medical Physics, Radiology
Andy Alexander, PhD, Professor, Medical Physics, Psychiatry

Table of Contents

Abstract ... iii
Acknowledgements ... v
Chapter 1 Background ... 1
  1.1 Spoiled Gradient Echo Imaging ... 2
  1.2 Fully Balanced Steady-State Free Precession ... 4
  1.3 Fat Suppressed Alternating Repetition Time Imaging ... 7
  1.4 Three Dimensional Out-and-Back, Radial Trajectory ... 9
    1.4.1 B0 & Linear Eddy Current Corrections for 3D Radial MRI ... 10
    1.4.2 Efficiency Analysis ... 14
Chapter 2 High Resolution Hip Imaging with VIPR-ATR ... 19
  2.1 Introduction ... 19
  2.2 Materials and Methods ... 20
    2.2.1 Study Group and MR Protocol ... 20
    2.2.2 Arthroscopic Hip Surgery ... 22
    2.2.3 Image Quality Analysis ... 22
    2.2.4 Review of MR Hip Arthrograms ... 23
    2.2.5 Statistical Analysis ... 25
  2.3 Results ... 25
  2.4 Discussion ... 29
  2.5 Acknowledgements ... 32
Chapter 3 icones: 3D Isotropic, High Resolution, Rosette-like Sampling Pattern 33
  3.1 Introduction: Basic description of icones trajectory and potential benefits ... 33
  3.2 Methods: Designing the sampling pattern, data acquisition, and image reconstruction ... 35
    3.2.1 Creating the 2D petal ... 36
    3.2.3 Implementing icones as a pulse sequence on MR scanners ... 55
    3.2.4 Compatibility with multiple contrast mechanisms ... 59
    3.2.5 Image Reconstruction ... 59
  3.3 Results ... 64
    3.3.1 Examples of icones sampling patterns ... 64
    3.3.2 Impulse Response ... 70
    3.3.3 The Adapted Iterative Density Compensation Routine ... 79
    3.3.4 The Calibration Method in a Water Phantom ... 81
    3.3.5 T2-like Acquisition of the Human Knee ... 85
    3.3.6 T1-w Acquistion of the Human Brain ... 88
  3.4 Discussion ... 90
    3.4.1 Examples of icones trajectories ... 91
    3.4.2 Icones Impulse Response for a Narrow Petal Design ... 92
    3.4.3 Icones Impulse Response for a Wider Petal Design ... 93
    3.4.4 Adaptation of Iterative Density Algorithm ... 94
    3.4.5 Calibration Method ... 94
    3.4.6 T2-like Images of the Knee ... 95
    3.4.7 T1-w Images of the Brain ... 97
    3.4.8 Limitations of icones ... 98
    3.4.9 Potential Advantages of icones ... 99

Chapter 4 Summary and Future Work 101
4.1 Summary of contributions........ 101
4.2 Future Work 103
References 107

Abstract

Three-dimensional radial MRI trajectories using simple bipolar gradients allow rapid acquisition of very high spatial resolution within limited timing constraints used for fat/water separated imaging. The bipolar 3D radial trajectory has demonstrated a leading position in generating high resolution images of the knee, elbow, and breast, producing resolution as high as 0.3 mm in an 8-minute knee exam. We present preliminary results of a clinical research study conducted to assess the ability of the bipolar 3D radial trajectory for detecting hip joint degradation on symptomatic patients by comparison with the standard clinical MRI protocol.

Despite its high spatial resolution and high signal yields, the bipolar 3D radial trajectory samples data somewhat inefficiently. In particular, its velocity must slow to zero before reversing directions. We have developed a more efficient out-and-back 3D rosette-like trajectory, termed icones for the shape's similarity to an ice cream cone, for use in time-limited data acquisition applications. The trajectory has the potential to achieve reductions in scan time or undersampling by 30% when compared to the bipolar 3D radial trajectory. This increased efficiency can be harnessed to either reduce undersampling artifacts or acquisition time when compared to out-and-back, 3D radial imaging.

We present an algorithm for calculating a 2D rosette-like petal and unique 3D rotation matrices to generate the full 3D trajectory from the 2D petal. We provide descriptions of an efficient implementation on MR systems, a calibration method to correct k-space trajectory deviations and phase errors induced by eddy-currents, and adaptation of an iterative density compensation routine for gridded image reconstruction.

Images of the impulse response show promise of the technique, which is still in need of refinement. Corresponding images of gridded k-space reveal appropriateness of the density compensation and symptoms of unresolved issues with the trajectory. Feasibility of the icones trajectory is provided, including T1-weighted acquisition of the brain, and T2-like acquisitions of the knee. The main limitation is the challenge of keeping the calibration at a reasonable duration. Future work includes optimizing the 3D sampling strategy, in vivo measurement of reduced undersampling, and comparison with the bipolar 3D radial trajectory.

Acknowledgements

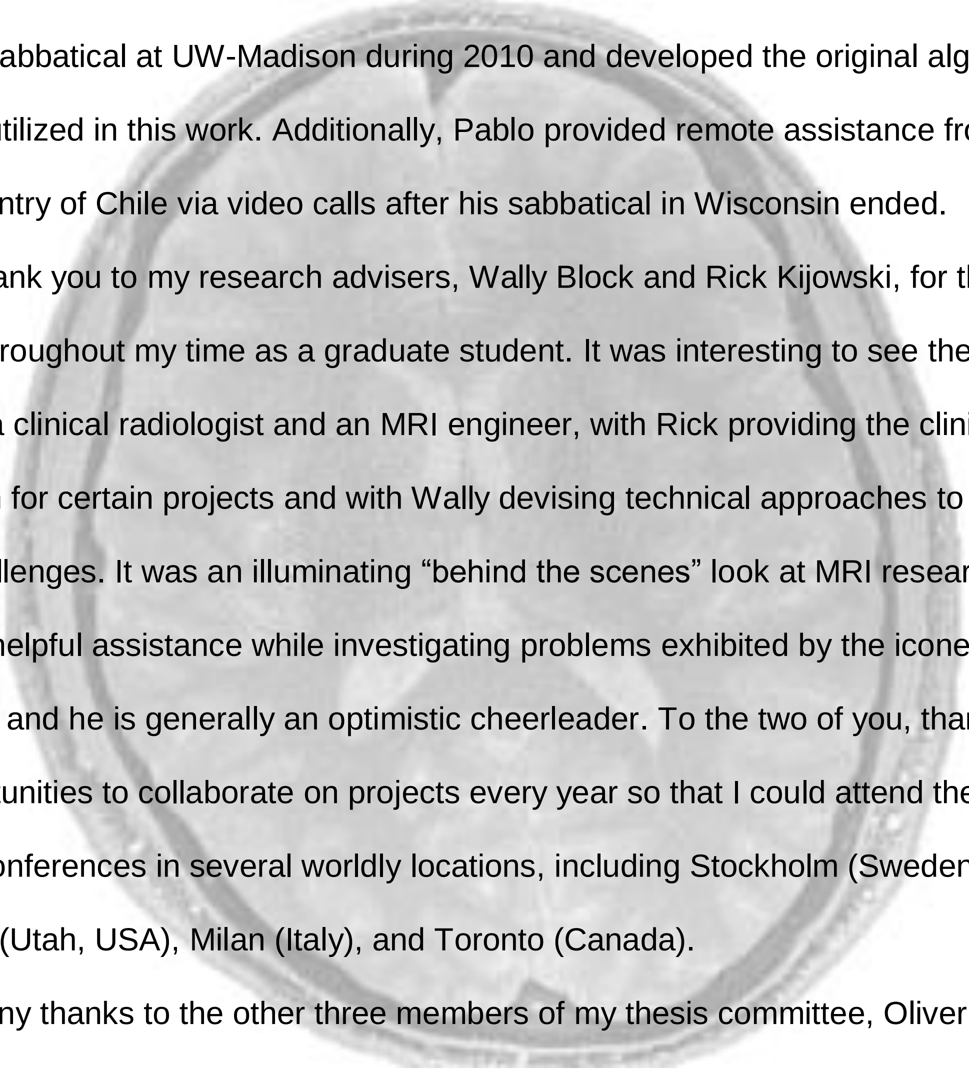

This work would have been much more difficult to complete without the support of many notable people. Thank you all!

Many thanks to Pablo Irarrazaval, for contributions to the main component of this thesis project: the 3D icones sampling pattern. Pablo developed the icones trajectory while on sabbatical at UW-Madison during 2010 and developed the original algorithm that was utilized in this work. Additionally, Pablo provided remote assistance from his home country of Chile via video calls after his sabbatical in Wisconsin ended.

Thank you to my research advisers, Wally Block and Rick Kijowski, for their support throughout my time as a graduate student. It was interesting to see the interplay between a clinical radiologist and an MRI engineer, with Rick providing the clinical motivation for certain projects and with Wally devising technical approaches to address those challenges. It was an illuminating “behind the scenes” look at MRI research. Wally provided helpful assistance while investigating problems exhibited by the icones trajectory, and he is generally an optimistic cheerleader. To the two of you, thanks for the opportunities to collaborate on projects every year so that I could attend the ISMRM Annual Conferences in several worldly locations, including Stockholm (Sweden), Salt Lake City (Utah, USA), Milan (Italy), and Toronto (Canada).

Many thanks to the other three members of my thesis committee, Oliver Wieben, Andy Alexander, and Beth Meyerand, who provided counsel on my research plan and also taught courses about fundamental and advanced topics in magnetic resonance imaging. The knowledge I gained in your courses served as a great foundation for conducting MRI research.

I am especially thankful to Kevin Johnson for his support in implementing the icones trajectory on the GE Healthcare scanners. Kevin was always very patient, understanding, and provided excellent tips on debugging the pulse sequence throughout the life-cycle of its implementation on the scanners and during development of image reconstruction software for this particular trajectory. Without Kevin's assistance this project would have taken much longer to arrive at its current stopping point. The GE scanner code is so lengthy that it is practically an entire universe of its own. Kevin, I cannot thank you enough for your help.

Thanks to my lab mates, including Leah Henze Bancroft, Jorge Jimenez, and Habib Al saleh, for your help with projects, including thoughtful discussions, technical support, and for allowing me to resonate your protons on several occasions. Thanks to other members of the MR Group for help with MRI research, especially when I broke the scanner, Karl Vigen, Orhan Unal, Kelli Hellendbrand, Sara John, Jenelle Fuller. And of course, I hold a lot of gratitude for my scan volunteers!

Thanks to my friends and grappling buddies of the Jujitsu Club, especially Sophie, Andrew, and Sensei Brant for providing a fun evening activity during which I could release a long, hard day's worth of frustration and also teach basic self-defense to others. To my teacher friends at Bliss Flow Yoga & Wellness—Kelly Fox, Sarah Mathis, Heather Last, Allie Waldera—your yoga classes were extremely beneficial to my physical and mental health, helping me to stay centered and focused during times of struggle. Plus, I'm more "stretchy" now! I will continue to practice even after I leave Madison.

Thank you, Abbey Thompson and Sara Patterson, for making the Science & Medicine Graduate Research Scholars (SciMedGRS) organization a warm and nurturing community that offered professional development, social activities, and several friendship opportunities with graduate students from other departments. And thank you for the continuous moral support from day one. Additionally, thanks to the graduate school and the SciMedGRS organizations for providing financial support so that some of this work could be completed.

I am grateful for the advice and encouragement received from long-distance friends and family, especially to Patrick Wong, Suzy Esquivel, Yvonne Lee Richardson, Waine Tam, Thanh Le, Luz Rosales, and Kerri Hernandez. Pat, our phone chats provide comic relief from the seriousness of everyday life. I look forward to our travels!

Thanks to all my graduate school friends for the fun times exploring Wisconsin and the Midwest, river rafting, various concerts, game nights, cook outs, outings to Devil’s Lake, softball practices & games, etc. A special shout-out to my teammates on the Medical Physics softball team, Annihilation in Flight. It only took 26 games, played over the course of several seasons, for us to finally claim a victory: perseverance!

Your friendships have meant a lot to me: Ana Cristina Fulladolsa-Palma, Christine Muganda, Deb Horng, Dave Niles, MariaJose Bedoya, Laura Bell, Mike Loecher, Anna Cotter and Courtney Morrison. MJ, I appreciated our many funny workplace dialogues, various outings about Madison, and your endless supply of gum! Laura, thank you for introducing me to yoga & Bliss Flow, and for being a friendly, positive, insightful person. Dave, our “man-dates” were entertaining, especially when peppered with wild ideas like intentionally setting our garden plots ablaze to enrich the

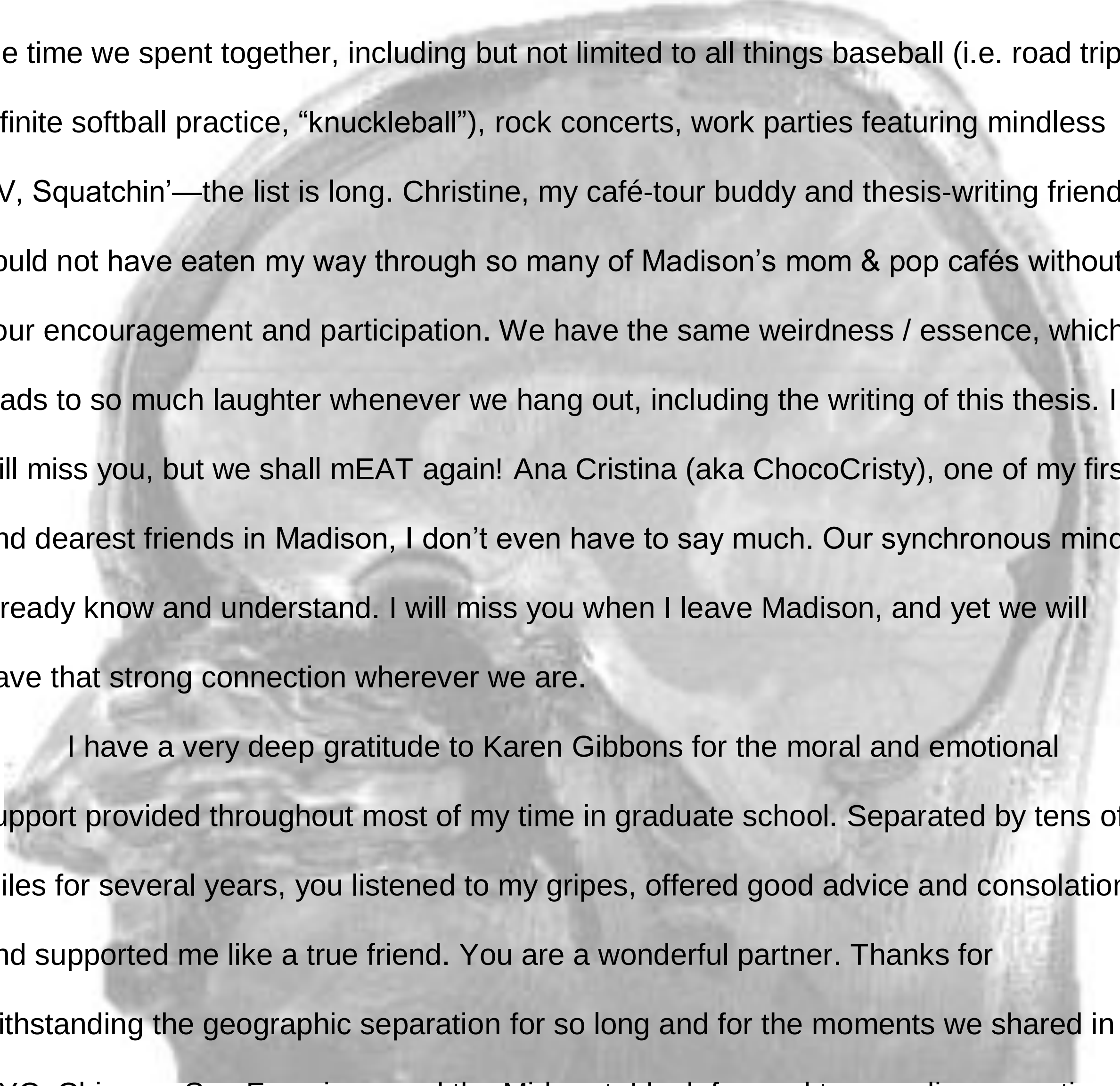

soil and salting the earth of nearby plots as a form of weed-control. Deb, thanks for your regular support and willingness to help me with just about anything, including popping over to Brasserie V on a whim! “MAnna”, thanks for letting me be the third wheel on so many dinner & movie nights and for your unwavering companionship. Courtney, I value the time we spent together, including but not limited to all things baseball (i.e. road trips, infinite softball practice, “knuckleball”), rock concerts, work parties featuring mindless TV, Squatchin’—the list is long. Christine, my café-tour buddy and thesis-writing friend, I could not have eaten my way through so many of Madison’s mom & pop cafés without your encouragement and participation. We have the same weirdness / essence, which leads to so much laughter whenever we hang out, including the writing of this thesis. I will miss you, but we shall mEAT again! Ana Cristina (aka ChocoCristy), one of my first and dearest friends in Madison, I don’t even have to say much. Our synchronous minds already know and understand. I will miss you when I leave Madison, and yet we will have that strong connection wherever we are.

I have a very deep gratitude to Karen Gibbons for the moral and emotional support provided throughout most of my time in graduate school. Separated by tens of miles for several years, you listened to my gripes, offered good advice and consolation, and supported me like a true friend. You are a wonderful partner. Thanks for withstanding the geographic separation for so long and for the moments we shared in NYC, Chicago, San Francisco, and the Midwest. I look forward to spending more time with you in person after graduating.

May the love and support that you all you provided to me during these years be granted upon each of you seven-fold.

Chapter 1 Background

This dissertation is divided into two projects within the field of diagnostic magnetic resonance imaging. The first project is a preliminary study comparing the efficacies of several two-dimensional conventional clinical Cartesian-based acquisition schemes and a recently developed three-dimensional, non-Cartesian, acquisition scheme in detecting hip joint abnormalities. The second project comprises the primary work of this dissertation and focuses on the development and implementation of a novel, rapid, three-dimensional, non-Cartesian MRI acquisition scheme that is applied in musculoskeletal (MSK) imaging. The emphases on achieving rapid, high resolution, volumetric musculoskeletal imaging using 3D non-Cartesian data acquisition are the unifying themes of these two projects.

The four primary topics presented in this chapter collectively provide a foundation of the core imaging concepts that are utilized and studied in this work. The first two topics, Spoiled Gradient Echo (SPGR) imaging and Fully Balanced Steady-State Free Precession (SSFP), are two standard MRI pulse sequences that are widely employed in musculoskeletal and body imaging. The third topic, Fat Suppressed Alternating Repetition Time (FS-ATR) [1], is a technique which has yielded excellent visualizations of the cartilage surfaces of the elbow and knee joints due to its ability to suppress lipid signal emanating from surrounding structures. The fourth topic is a brief overview of the three-dimensional, out-and-back radial sampling pattern named Vastly Undersampled Isotropic Projection Reconstruction (VIPR) [2] that has recently gained attention for its ability to provide high resolution images of the knee, hip, and breast in short scan time. This particular 3D, radial sampling pattern is the primary motivation for all of the work completed here. It is the focus of the hip arthroscopy study presented in Chapter 2 (the first project mentioned above). Inefficiencies in this sampling pattern have provided motivation for the development of a novel 3D sampling pattern that is described in Chapter 3 and which forms the bulk of this dissertation.

1.1 Spoiled Gradient Echo Imaging

Gradient echo (GRE) pulse sequences are employed in routine, clinical MRI of joints due to their ability to provide adequate fluid-cartilage and cartilage-bone contrasts in short scan times. These sequences utilize low flip angle excitation pulses that leave most of the longitudinal magnetization undisturbed while generating considerable transverse magnetization, allowing for short TRs and thus short scan times.

GRE sequences that spoil the transverse magnetization at the end of each TR are termed Spoiled Gradient Echo (SPGR) sequences (Figure 1). There are several methods for spoiling magnetization, including selection of TRs that are five times T_2, or employing end-of-sequence gradient spoilers with areas that vary between TR intervals, but the fastest and most effective technique incorporates scheduled phase changes in the radiofrequency excitation pulse and utilizes spoiler gradients at the end of each TR after readout. The combination of the spoiler gradient and RF phase cycling effectively eliminates pathways by which transverse magnetization from one TR can be refocused during a later TR. Radiofrequency spoiling also reduces the trajectory deviations that result from eddy currents that build up to various degrees across each TR when spoiling is attempted through the sole use of area-varying spoiler gradients.

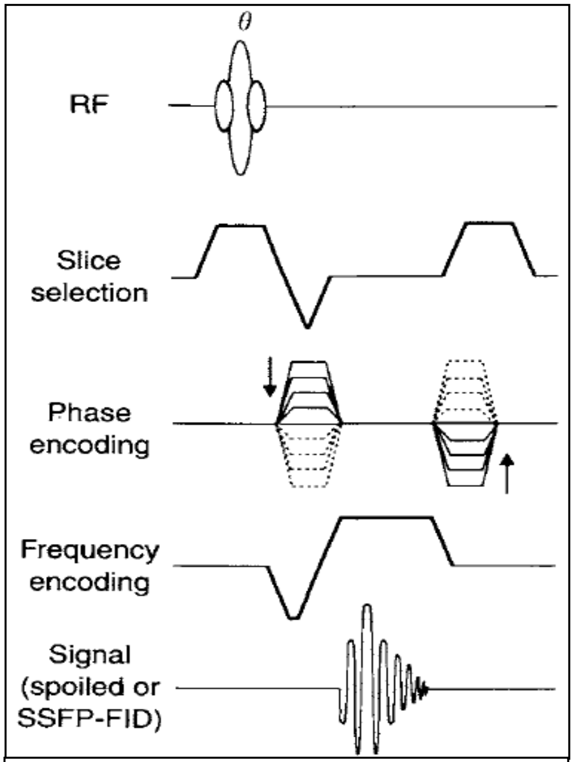

Figure 1: Spoiled Gradient Pulse Sequence

In SPGR imaging the signal for a single T1 species is formed by gradient refocusing of the free induction decay (FID) at the echo time (TE). An analytical form for the signal can be derived from physical principles [3]:

$$S_{spoil} = \frac{M_0 \sin\theta\left(1 - e^{-TR/T1}\right)}{\left(1 - \cos\theta e^{-TR/T1}\right)} e^{-TE/T2*} \tag{1}$$

The Ernst angle, θ_E, which maximizes this signal for a tissue with a specific T1 is:

$$\theta_E = \arccos(e^{-TR/T_1}) \tag{2}$$

and resides between 0° and 90°, monotonically increasing as TR/T1 increases. From this equation it can be seen that when the flip angle is less than θ_E, then an increase in the flip angle results in increased signal because the creation of more transverse magnetization outweighs the loss in longitudinal magnetization that can be used in subsequent TRs.

SPGR sequences can be employed as 2D or 3D acquisitions. Routine, clinical evaluation of knee cartilage during an MRI exam often utilizes 3D spoiled gradient sequences, usually with the in-plane dimension in the sagittal or coronal planes. Scan time and SNR constraints often force acquisitions with anisotropic voxels. Acquisitions in multiple planes and orientations are then used to counteract partial volume averaging, magic angle effect, and to provide the clinician with multiple views of the curved surfaces of the knee joint.

Fat-suppression techniques are typically employed with SPGR sequences when imaging joints. This helps remove unwanted bright lipid signal, ameliorating the partial volume effect, chemical shift artifact, and improving contrast at cartilage-bone and fluid-bone interfaces. Two commonly used methods are frequency-selective fat saturation and iterative decomposition of fat and water with echo asymmetry and least squares (IDEAL) [4].

1.2 Fully Balanced Steady-State Free Precession

Fully balanced steady-state free precession (SSFP) sequences are employed in musculoskeletal imaging [5-7] due to their high signal levels, bright fluid, versatile T2/T1 soft-tissue contrast, and ability to highlight the fluid-bone and fluid-cartilage interfaces that are important for diagnosing disease or acute injury of joints. Steady state sequences employ self-balanced gradients along all axes to re-phase spins prior to subsequent RF excitation and constant TRs in order to maintain the steady states of the transverse and longitudinal magnetization. Figure 2 depicts an example of a 3D radial SSFP sequence which has been used for imaging the elbow. A 180° incremental phase shift of the RF pulse is incorporated for each excitation and leads to a 0°-180° phase cycling scheme and higher signal magnitude. Without these incremental 180° RF phase shifts, the null of the spectral response occurs on-resonance and leads to low signal (Figure 3).

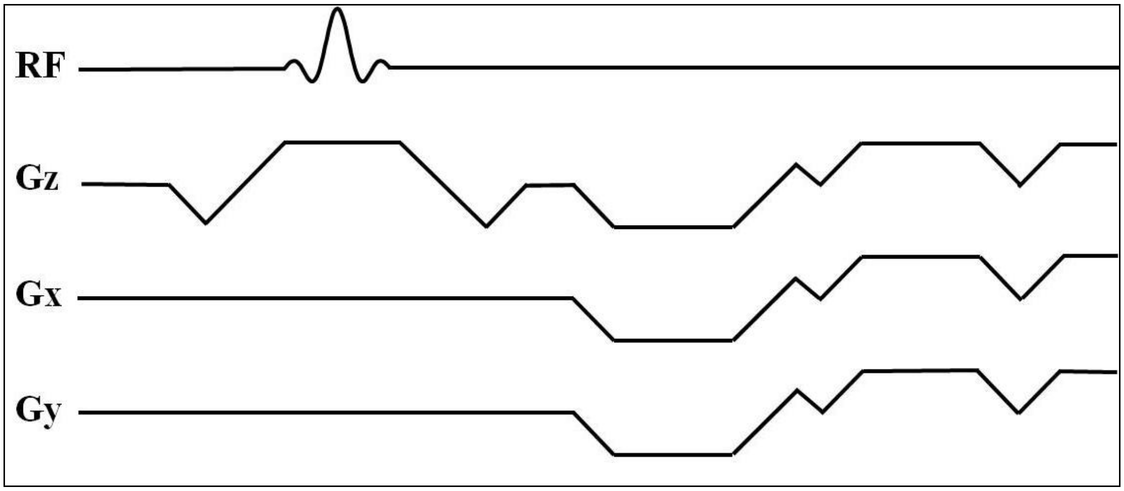

Figure 2: Pulse sequence for 3D projection imaging with SSFP. All gradients are fully rewound to refocus transverse magnetization during each TR.

The SSFP signal magnitude largely depends on the flip angle, longitudinal recovery time T_1, transverse decay time T_2, and TR interval [3]. SSFP sequences incorporating sign-alternating RF excitation phase produce signals with the largest magnitude and can be expressed as:

$$S_{ssfp} = \frac{M_0 \sin\theta \left(1 - e^{-TR/T1}\right)}{\left(1 - (e^{-TR/T1} - e^{-TR/T2})\cos\theta - e^{-TR/T1} e^{-TR/T2}\right)} e^{-TE/T2*} \qquad (3)$$

For the case TR << T2 < T1 and θ=90°, this formula simplifies to:

$$S_{ssfp} = \frac{M_0 T_2}{T_1 + T_2} e^{-TE/T2^*} \tag{4}$$

When T2 << T1, this formula can be further reduced to:

$$S_{ssfp} \approx \frac{M_0 T_2}{T_1} e^{-TE/T2^*} \tag{5}$$

explaining why SSFP sequences are said to exhibit T2/T1-weighted contrast. This type of contrast is said to be “T2-like” since the respective T2 and T1 values of fluid, muscle, and fat yield relative signal intensities that are comparable to those of T2-weighted images, with fat exhibiting very high signal intensity, fluid having high signal, and muscle exhibiting intermediate signal.

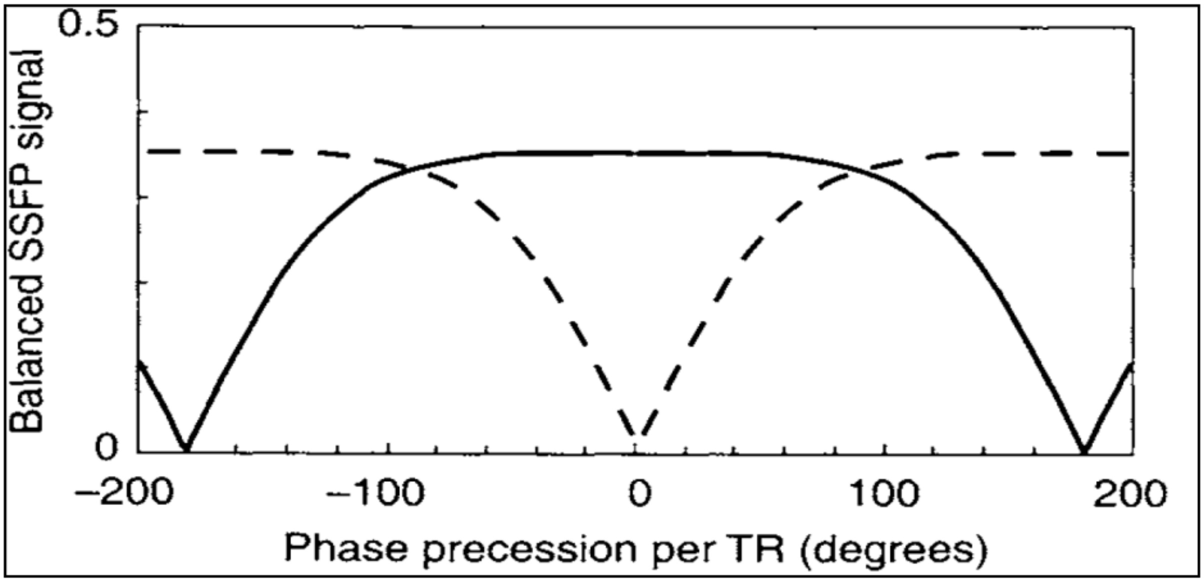

Figure 3: SSFP spectral response versus phase precession per TR of transverse magnetization. Sign alternated RF pulses yield strong on-resonance signal (solid line) and minimum at 180°. Without sign alternation (dashed line), the response shifts so that the minimum occurs on resonance.

SSFP acquisitions suffer from banding artifacts (Figure 3) that occur when phase shifts of π occur in each TR. The width of the signal pass-band is inversely proportional to the TR. Decreasing the TR reduces banding artifact, but also reduces time for encoding, thereby limiting the spatial resolution that can be achieved. Thus, rapid imaging with SSFP requires a trade-off between the desire to obtain high spatial resolution and tolerating an acceptable degree of banding artifact.

An immediate consequence of the SSFP spectral response is a bright lipid signal which may reduce signal contrast at bone-tissue and tissue-fluid interfaces, confounding image quality in regions of interest to radiologists. Methods like fat-suppressed alternating repetition time (FS-ATR), Fluctuating Equilibrium Magnetic Resonance (FEMR) [8], Linear Combination SSFP (LC-SSFP) [9], and IDEAL have been developed to separate or suppress this characteristically bright lipid signal. Recently, the out-and-back, 3D radial SSFP sampling pattern has been combined with IDEAL and FS-ATR to yield high quality, fat-suppressed images of the elbow, knee, and breast [10-13].

1.3 Fat Suppressed Alternating Repetition Time Imaging

Fat Suppressed Alternating Repetition Time (FS-ATR) imaging is an acquisition scheme that combines radiofrequency phase cycling over two different TR intervals to modify the spectral frequency response in a way that places a stop-band over the off-resonant lipid frequencies (Figure 4) while placing a moderately broad pass-band over the resonant water frequency [1]. The TR1:TR2 ratio for optimal fat suppression is 3:1. Data acquisition occurs during the longer TR1 interval; only RF excitation occurs during the shorter TR2 interval.

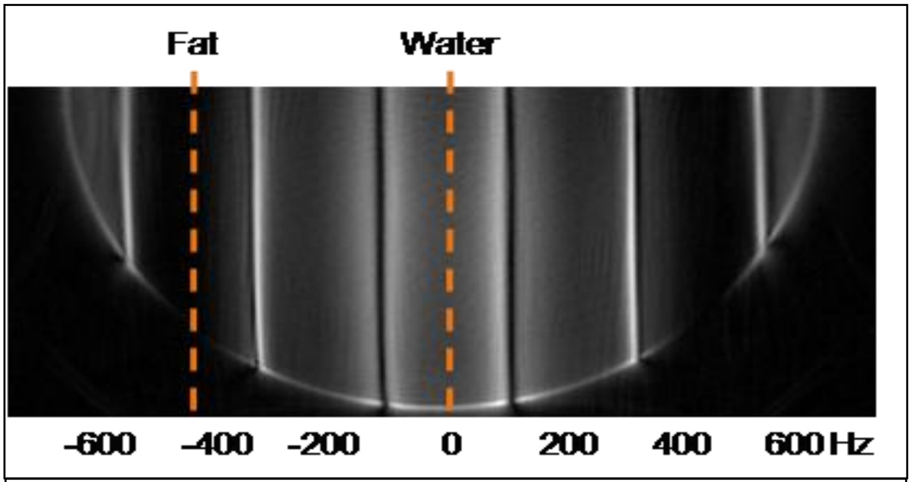

Figure 4: FS-ATR spectral profile with stop-band centered on fat resonance. Off resonance signal generated with linear gradient field across spherical water phantom.

Figure 5 depicts VIPR-ATR, a dual half-echo 3D radial SSFP pulse sequence that incorporates the FS-ATR method. The TR1 and TR2 values are chosen in a 3:1 ratio to achieve the desired spectral response, with a TR1 of 3.45ms and TR2 of 1.15ms combining to yield an effective TR of 4.6ms. As previously mentioned, data acquisition occurs only during TR1. The RF excitation during the second short TR interval is only used to change the shape of the frequency response profile, which for a TR1:TR2 ratio of 3:1 and an appropriately chosen RF phase cycling scheme results in a broadened pass-band for the water signal and a symmetric stop-band for the lipid signal. The phase of the second RF pulse is set to 180° and when combined with the traditional SSFP phase cycling of 0°-180° for the first RF pulse results in a 0°-180°-180°-0°-0° phase cycling schedule [13]. This particular implementation has yielded 0.4 mm isotropic resolution in 5 minutes and 0.3mm isotropic resolution in 8 minutes [10] in eight channel whole knee coil imaging exams at 3.0T.

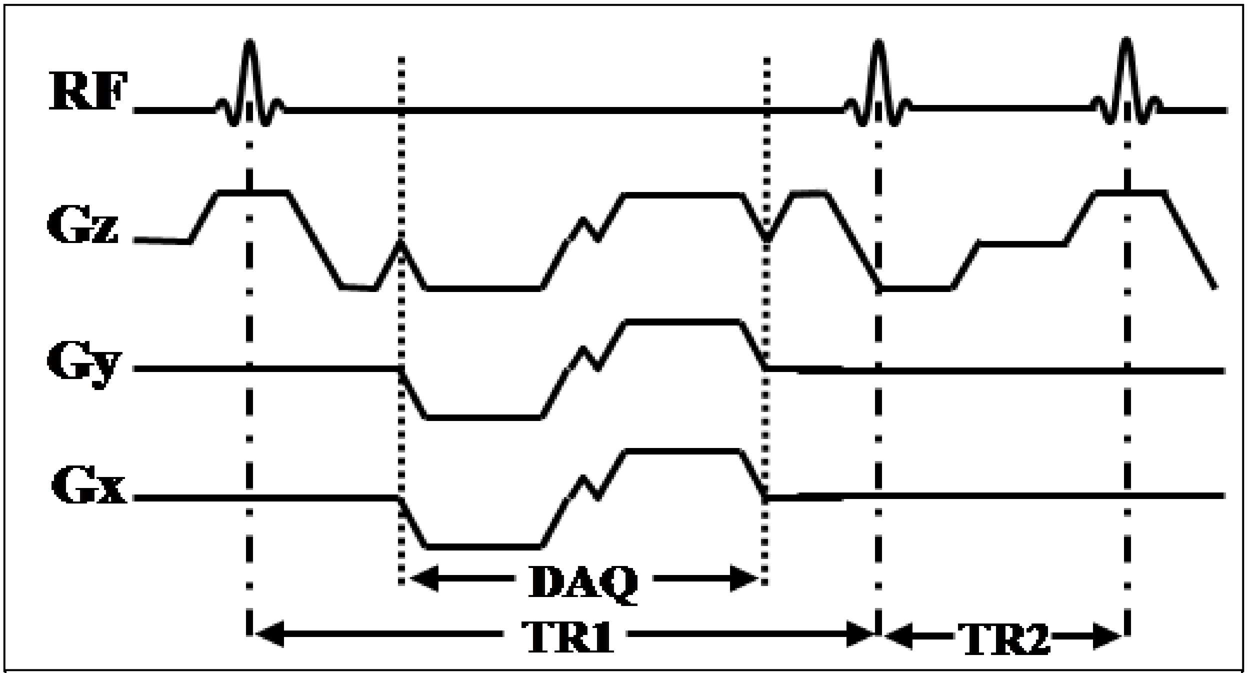

Figure 5 FS-ATR method employed with a dual half-echo 3D radial pulse sequence.

1.4 Three Dimensional Out-and-Back, Radial Trajectory

Achieving the short TRs characteristic of steady state imaging has been possible due to the high slew-rate achievements of modern gradient systems. While these gradient systems provide spatial encoding time for Cartesian SSFP sequences, the onset of peripheral nerve stimulation limits the slew-rates to lower usable values. This imposes an upper limit on the available time for spatial encoding and consequently restricts spatial resolution and SNR.

For a given TR, increases in resolution are achievable with out-and-back, 3D radial acquisitions such as Vastly Undersampled Isotropic Projection Reconstruction (VIPR, [2]) (Figure 6a). This sequence utilizes bipolar gradients to encode the dephasing and rephasing gradients as two distinct, adjacent radial lines separated by a small angle, resulting in a dual, half-echo trajectory that begins and ends at the origin of k-space (Figure 6b).

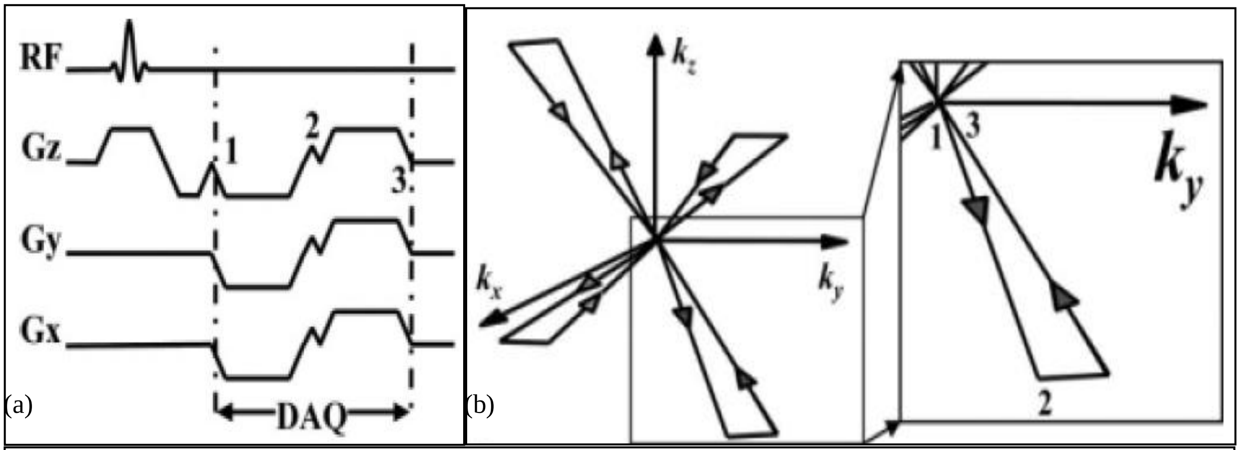

Figure 6 (a) Out-and-back 3D radial VIPR pulse sequence. (b) Two radial lines are sampled per TR, with the trajectory starting and ending at the center of k-space. Four TRs are shown here. The insert depicts one TR.

Employment of a thick slab excitation reduces refocusing time, the first echo time, and the repetition time. This sampling pattern doubles the acquisition efficiency relative to Cartesian [14], leading to increased readout time, higher spatial resolution and higher SNR.

1.4.1 B0 & Linear Eddy Current Corrections for 3D Radial MRI

Time varying gradient fields within the MRI system create eddy currents within the cryostat which generate magnetic fields that attenuate the gradients generating them. The most significant aspects of these eddy currents affecting image quality are the time-varying, spatially independent B0 component and the linear component. The B0 component imposes unwanted phase accrual on the imaging data, whereas, the linear component causes k-space trajectory deviations. The deleterious effects of eddy currents are typically addressed through the use of gradient coil shielding, waveform pre-emphasis compensation, real-time dynamic phase adjustment to the center frequency generator, self-encoding gradient pulses [15], reference scans using specialized phantoms, trajectory-specific schemes [16], and simple, quick calibration scans, such as the Duyn Method [17-19].

1.4.1.1 B0 Eddy Current Corrections

B0 currents are particularly problematic for sequences utilizing ramp sampling and multi-echo bipolar readouts at various azimuthal angles. Brodsky adapted a quick & simple method [19] to measure and correct unwanted B0-eddy current induced phase accruals for the 3D radial, dual, half-echo bipolar readout sequence [17]. This method measures B0 eddy current phase variations due to a single bipolar gradient waveform, with measurements made on two thin, parallel slices equidistant from isocenter (Figure 7) and perpendicular to the axis of the gradient. Each slice is acquired twice, once with the test waveform and again with an inverted version of it.

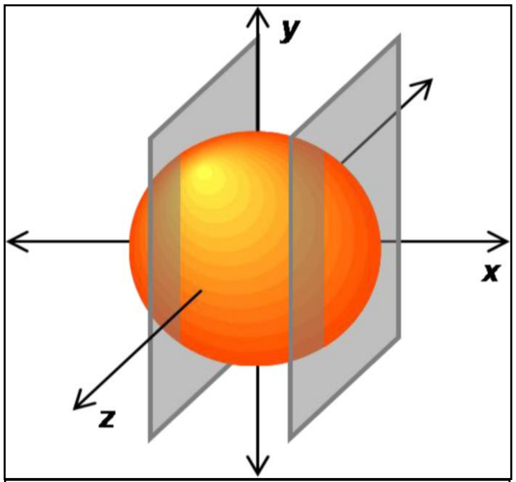

Figure 7 In the extended Duyn method, data are acquired from test slices situated on opposite sides of a phantom placed at isocenter.

Appropriate combination of these measurements (Figure 8) removes phase errors due to off-resonance & self-squared concomitant terms, as well as linear eddy current effects, isolating the B0 phase variations. The process is the following: (1) Phase unwrap each data set (2) for each slice & axis, calculate the phase difference between the data with positive and negative polarity, eliminating off-resonance & self-squared concomitant terms, to yield $\Phi_{S1} = 2\Phi_{B0} + 4\pi kx$ and $\Phi_{S2} = -2\Phi_{B0} + 4\pi kx$, where $2x$ is the physical separation of the slices. (3) Compute the difference of these two results to yield the net phase between the two oppositely placed slices, thereby removing the desired phase accumulation from the gradient itself and undesired phase due to linear eddy currents. (4) Division by four yields the phase accumulation due to the remaining B0 eddy currents.

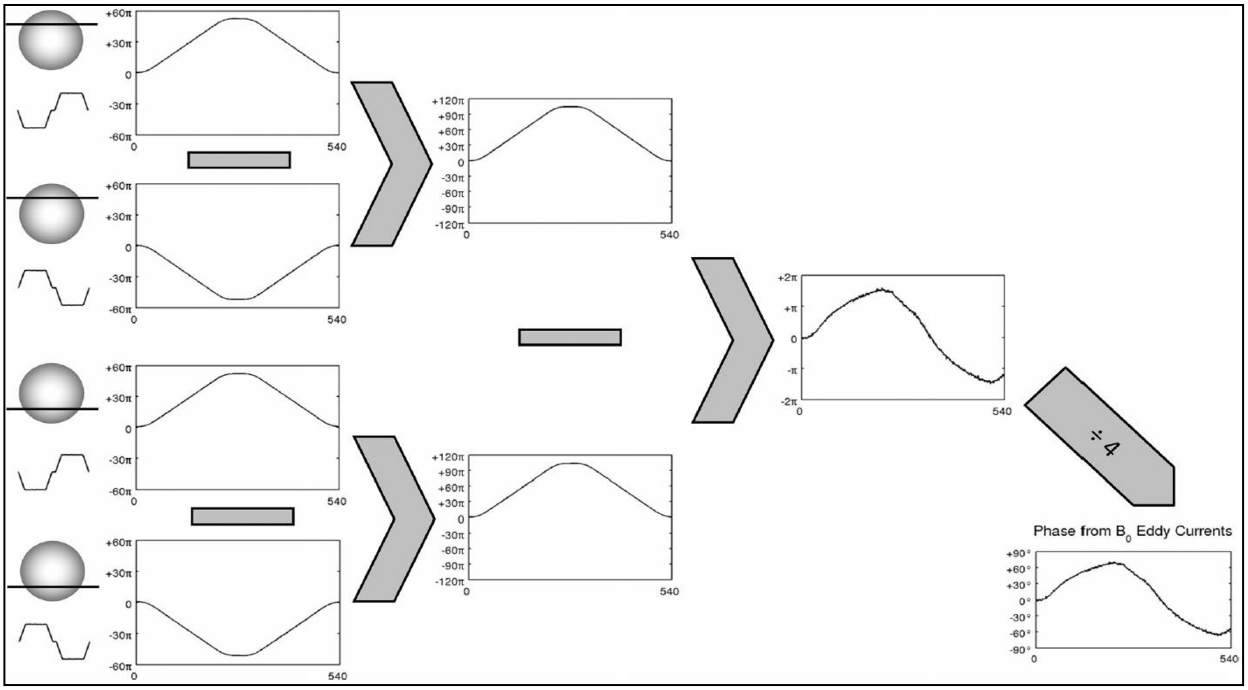

Figure 8: B0 phase correction for bipolar gradient, 3D projection reconstruction (3D PR) acquisition. For each slice location, the difference in phase for data acquired with positive and negative gradient polarity eliminates off-resonance and concomitant terms. The difference between the data acquired at opposite slice locations reduces effects due to the test gradient, including linear eddy currents. Division by 4 yields phase accumulation primarily due to B0 eddy currents.

When independent measures of this single waveform are performed on all three orthogonal axes, appropriate linear combinations of the results may be used to predict the B0 phase variations that would result from a gradient field that is generated when different scalar versions of this waveform are played simultaneously on the three orthogonal axes, thereby producing B0 phase error corrections for all projections of a 3D radial sequence. In particular, the ith projection data are phase corrected using the following equation:

$$\Delta\Phi_{B0}(j,i) = M_x(j)P_x(i) + M_y(j)P_y(i) + M_z(j)P_z(i) \qquad (6)$$

where $M_x(j)$, $M_y(j)$, $M_z(j)$ are the measured B0 eddy current phase errors at sample *j*, and $P_x(i)$, $P_y(i)$, $P_z(i)$ are the gradient strengths along the x, y, and z axes, respectively, for projection *i*.

1.4.1.2 Trajectory Corrections due to Linear Eddy Currents

The trajectory correction scheme for 3D, out-and-back radial imaging utilizes the same calibration data acquired for the point-by-point B0-phase accrual corrections. A slight difference in the processing—summing Φ_{S1} and Φ_{S2}, then dividing by $8\pi x$—results in a corrected k-space trajectory which accounts for gradient timing delays and linear eddy currents:

$$k_x = \frac{\Phi_{S1} + \Phi_{S2}}{8\pi x} \qquad (7)$$

1.4.2 Efficiency Analysis

Historically, variants of sampling patterns have been developed to exploit inefficiencies in k-space trajectories [20-24]. The spiral trajectory[21] was created to decrease scan time and cover k-space somewhat more efficiently than the Cartesian trajectory by requiring fewer excitations for similar k-space coverage. These trajectories exhibit reduced sensitivity to motion but may suffer from blurring and resolution loss for long acquisitions.

The twisting radial-line (TwiRL) [20] acquisition extended 2D projection (PR) by employing a twist to the radial trajectory at the outer edge of k-space to increase high spatial frequency sampling (Figure 9). This provided a more uniform k-space sampling density and reduction of necessary excitations by factors of three to four when compared to 2D PR.

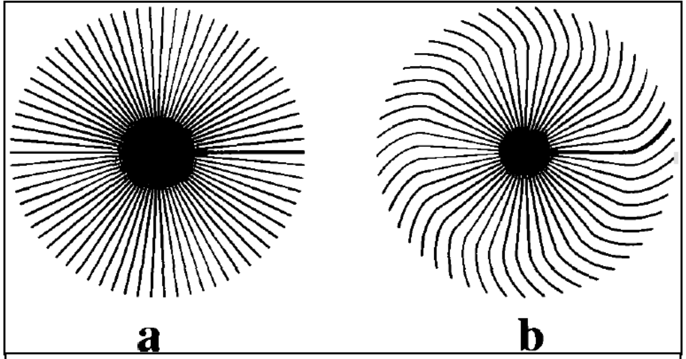

Figure 9: Altering the linear trajectory in (a) 2D PR at the end of each TR with a (b) twist (2D TwirRL) allows a reduction of 25% of the needed excitations in TwiRL relative to 2DPR.

Two-dimensional, multi-shot rosette sampling patterns [22] using sinusoidal gradients were developed by Noll for spectrally selective MRI. These multi-shot acquisitions (Figure 10) exhibited losses in image intensity but very little blurring from off-resonance spins which contribute to a pseudorandom distribution of energy in the image. These advantageous off-resonance properties are attributed to the self-crossing nature of the trajectory and high degree of sampling at the origin.

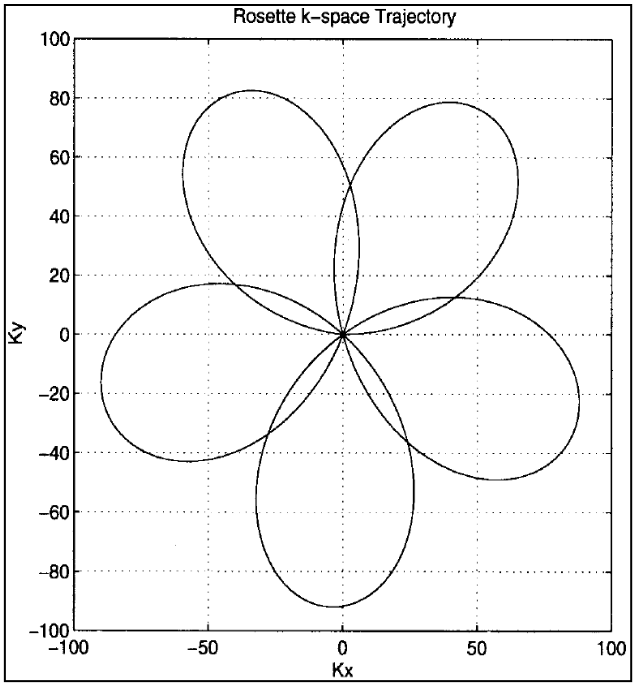

Figure 10 Single acquisition of 60-shot rosette pattern

In the realm of 3D imaging, the out-and-back, 3D radial trajectory samples k-space with higher efficiency than traditional 3DPR by acquiring data along two adjacent radial spokes during each excitation (Figure 6b). However, despite its high spatial resolution and high signal yields, this trajectory exhibits some inefficiency in k-space coverage, as k-space velocity must slow to zero before reversing directions. While ramp-sampling is employed to make efficient use of the time that the trajectory slows from maximum speed to zero and then back to maximum speed, a more efficient approach would take advantage of the gradient system to create a smooth turn of the trajectory at constant speed. Additionally, high spatial frequencies are disproportionately undersampled in comparison to the center of k-space, leading to a haze noise-like artifact from unsampled, aliased energy over the image.

We have developed an isotropic, dual half-echo 3D rosette-like sampling pattern (Figure 11), termed icones, that improves upon the sampling inefficiency of the out-and-back, 3D radial trajectory while maintaining the same tight TR or echo spacing constraints often used in SSFP imaging and robust fat/water separation methods. Icones exhibits freedom to change direction over wide curvatures while maintaining a higher speed than the out-and-back 3D-PR as it nears the edge of k-space, making efficient use of the available time for spatial encoding and consequently optimizing signal-to-noise ratio. A 2D petal-shaped sampling pattern (Figure 11c) is generated using a pair of fully balanced gradients (Figure 11a), denoted G_x and G_y in this document. This petal is then rotated in k-space, once for each TR, to generate a 3D sampling pattern that overlaps in the outer regions of k-space. This overlap reduces undersampling of high spatial frequencies compared to the out-and-back 3D radial trajectory.

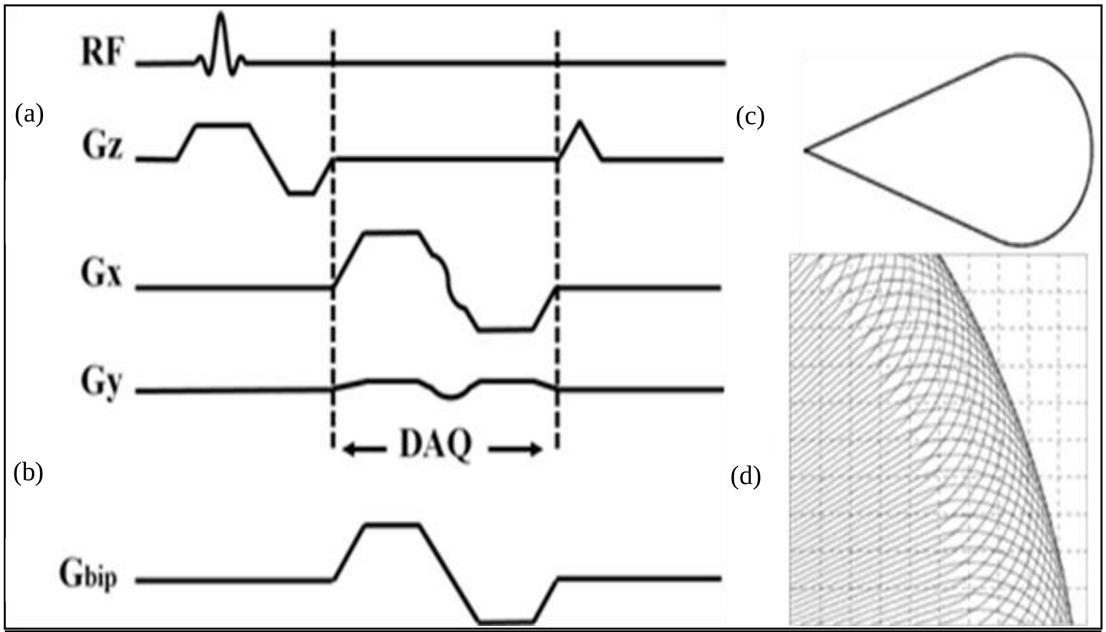

Figure 11 (a) SPGR implementation of icones, (b) bipolar gradient for comparison. icones gradients generate a trajectory (c) similar to one leaf of a rosette sampling pattern. A 2D depiction (d) of the overlapping trajectory is provided for illustration. Note, the parameter skip = 17 in (c) and (d).

A 2D rendition (Figure 11d) demonstrates the degree to which overlapping may be achieved. The G_x gradient is similar to a bipolar trapezoid (Figure 11b), but with a modified bridge, so that with G_y the trajectory curves along the arc of a circle before reaching the periphery of k-space to maintain nonzero velocity while sampling high frequencies. The expected benefits of this trajectory are a reduction in undersampling artifact for a given acquisition time or a reduction in sampling time for a given undersampling factor, when compared to the 3D, radial out-and-back trajectory. Details about this new sampling pattern are provided in Chapter 3.

Chapter 2 High Resolution Hip Imaging with VIPR-ATR

2.1 Introduction

Patients with femoracetabular impingement (FAI) and other hip disorders that are considered early triggers of osteoarthritis (OA) may benefit from surgical interventions if labral tears and cartilage degeneration are detected during the earlier stages of the disease process [25-29]. However, evaluating the hip joint with any imaging modality is extremely challenging due to the thin articular cartilage and spherical geometry of the femoral head and acetabulum [30-32]. Conventional two-dimensional fast spin-echo (FSE) MRI sequences that are typically used for MR arthography of the hip acquire anisotropic voxels and utilize relatively thick slices with large inter-slice gaps to produce images that suffer from suboptimal in-plane resolution and partial volume artifact. MR arthrography with these sequences has a relatively low diagnostic performance for detecting surgically confirmed cartilage lesions and labral tears, from 62-81% for chondral damage and 69-90% for labral tears. Specificity performance is better, ranging from 81-100% for cartilage lesions and 70-100% for labral tears [33-38].

Radial-ATR [10] is a recently-developed, rapid, 3D sequence that can address the challenges associated with imaging the hip joint. Al saleh *et al.* demonstrated in knee imaging that Radial-ATR generates high quality, fat-suppressed, 0.4mm isotropic, volumetric images in a five minute, non-contrast enhanced scan using an eight channel extremity coil. Radial-ATR acquires thin, continuous slices that reduce partial volume artifact, and, when coupled with its ability to generate reformatted images in any plane, would be extremely valuable for imaging the complex, spherical geometry of the hip joint. Furthermore, Radial-ATR generates high fluid signal, high cartilage signal, and good fat-suppression that altogether may increase conspicuity of cartilage defects and other soft-tissue abnormalities if the sequence were used during MR arthrography. We hypothesize that Radial-ATR may provide the high signal needed to produce 3D reformatted images with much smaller voxel volumes than is possible with 2D or 3D FSE. In this investigation, we compare Radial-ATR with currently used 2D FSE sequences for evaluating the articular cartilage of the hip joint in symptomatic patients undergoing MR arthrography.

2.2 Materials and Methods

2.2.1 Study Group and MR Protocol

This study was performed in compliance with regulations of the Health Insurance Portability and Accountability Act (HIPAA) and with approval from our institutional review board. All subjects signed written informed consent prior to participation in the study. The study group consisted of 20 symptomatic patients who underwent MR arthrography of the hip with our standard clinical protocol as well as with 3D Radial ATR, followed by arthroscopic hip surgery. Each MR arthrography utilized a 3.0T scanner (Discovery MR750, GE Healthcare, Waukesha, WI) with high-performance gradients (maximum gradient strength, 50 mT/m; maximum slew rate, 200 $mT{\cdot}m^{-1}{\cdot}s^{-1}$) and an 8-channel phased-array cardiac coil (GE Healthcare, Waukesha WI). There were 6 male and 14 female patients, with mean age of 35 years (range 24 - 46 years).

Each MR exam consisted of the following sequences acquired after the intra-articular administration of gadolinium contrast material: coronal fat-suppressed 2D T1-weighted FSE (T1-FSE); coronal fat-suppressed 2D T2-weighted FSE sequences (T2-FSE); sagittal fat-suppressed 2D proton density-weighted FSE (PD-FSE) sequence;

and axial Radial-ATR. Each FSE sequence utilized a spectral inversion recovery pulse to suppress fat signal; however, the Radial-ATR sequence utilized the fat-suppressed alternating repetition time (FS-ATR) method [39] to achieve fat-suppression. For reference, the imaging parameters used for each sequence are listed in **Table 1** below:

Table 1: Acquisition parameters of sequences used to image the hip joint

Imaging Parameters	T1-FSE	T2-FSE	PD-FSE	Radial-ATR
TR/TE (ms)	530 / 20.3	4026 / 87.4	2500 / 20.1	4.6 / 0.3
Flip Angle	111°	111°	111°	15°
Bandwidth (kHz)	31.25	41.67	31.25	250.0
Field of View (cm)	20	20	18	40
Matrix Size	320 × 224	320 × 224	320 × 224	800 × 800
Slice Thickness (mm)	4.0	4.0	4.0	1.5†
In-Plane Resolution (mm × mm)	0.63 x 0.89	0.63 x 0.89	0.56 x 0.80	0.50 x 0.50
Voxel Volume (mm^3)	2.24	2.24	1.81	0.31†
Scan Time (min)	3.8	3.5	4.3	7.7

† Three-slice averaging in multiple planes was used to obtain images with 0.5mm x 0.5mm in- plane resolution and 1.5mm slice thickness.

Radial-ATR rapidly acquires isotropic resolution, fat-suppressed images by combining an efficient dual half-echo, 3D radial k–space trajectory called Vastly Undersampled Isotropic Projection Reconstruction (VIPR) [2], with fat-suppressed alternating repetition time (FS-ATR). The out-and-back, 3D radial acquisition allows for almost continuous data acquisition and nearly twice the resolution achievable with a Cartesian trajectory during the constrained 4.6ms TR for fat-water imaging at 3.0T. To achieve fat suppression, the sequence combines two alternating repetition times with radiofrequency phase cycling [1, 39] to create a null for off–resonance fat signal during the bSSFP acquisition [1].

2.2.2 Arthroscopic Hip Surgery

Surgical characterization of cartilage surfaces during hip surgery was performed on the 20 patients in the study group within three months of their MR examination. All hip surgeries were performed by one orthopedic surgeon with 12 years of experience at our institution. During surgery all articular surfaces of the hip joint were graded using the Noyes classification system (grade 0=normal, grade 1 = cartilage softening, grade 2A = superficial partial-thickness cartilage lesion less than 50% of the total thickness of the articular surface, grade 2B = deep partial-thickness cartilage lesion greater than 50% of the total thickness of the articular surface, and grade 3 = full-thickness cartilage lesion). The locations of cartilage lesions were recorded as anterosuperior and posterosuperior in the acetabulum, and anteromedial, anterosuperior, posteromedial, and posterosuperior in the femoral head.

2.2.3 Image Quality Analysis

Normalized signal-to-noise ratio efficiency (SNR) of articular cartilage, synovial fluid, and bone marrow and normalized contrast-to-noise ratio (CNR) efficiency between cartilage and synovial fluid and bone marrow were calculated for 10 examinations, with regions of interest (ROIs) placed at equivalent locations on the MR images. The standard deviation of the background ROI was used as an estimate of image noise for each sequence. As no parallel imaging processing was used in any of the MR sequences, the noise signal in the background was not manipulated by the reconstruction process.

SNR and CNR in surrounding structures of the hip joint were calculated using the following equations:

$$SNR = \frac{Signal}{\sigma_{background}} \tag{8}$$

$$CNR = \frac{\left| Signal_{tissue1} - Signal_{tisssue2} \right|}{\sigma_{background}} \tag{9}$$

To adjust for differences in imaging time across sequences, the SNR and CNR values were divided by the square root of the scan time to obtain SNR efficiency and CNR efficiency values. The SNR efficiencies and CNR efficiencies for each sequence were then normalized by the acquired voxel volume to adjust for the larger signal intensity attributed to larger voxel volumes acquired by the Cartesian trajectories. These normalized efficiency values were used to make quantitative comparisons of image quality across all sequences.

2.2.4 Review of MR Hip Arthrograms

All MR arthrograms were independently reviewed by a single Fellowship-trained musculoskeletal radiologist who has 14 years of clinical experience. The radiologist had previous experience reviewing MR images acquired with the 3D Radial sequence from other research studies designed to assess the correlation between 3D Radial ATR images and arthroscopic findings. The radiologist reviewed the standard MR arthrograms and the 3D Radial ATR images on distinct occasions separated by at least one month in order to prevent recall bias. The radiologist was blinded to the arthroscopic findings during reviews of the MR exams.

During the first review, the radiologist utilized all images from the standard clinical MR protocol to detect hip joint abnormalities of all articular cartilage surfaces of the hip joint and surrounding soft tissue structures. The cartilage lesions were graded using the Noyes classification system (grade 0=normal, grade 1 = cartilage softening, grade 2A = superficial partial-thickness cartilage lesion less than 50% of the total thickness of the articular surface, grade 2B = deep partial-thickness cartilage lesion greater than 50% of the total thickness of the articular surface, and grade 3 = full-thickness cartilage lesion). The locations of cartilage lesions were recorded as anterosuperior and posterosuperior in the acetabulum, and anteromedial, anterosuperior, posteromedial, and posterosuperior in the femoral head. The presence and locations of any labral tears evident in the images from the standard protocol were also recorded.

During the second stage of image review, the radiologist interpreted the 3D Radial ATR images after they had been reformatted into the sagittal, coronal, axial, and axial-oblique planes with three-slice averaging. Radial reformat images with three-slice averaging were also created to provide views of all articular surfaces on the femoral head. Cartilage lesions were graded using the same Noyes classification that was used during the first review and during surgical arthroscopy. The location of each lesion was recorded using the same categories that were used in the first review. The presence and locations of any labral tears evident in the images from the Radial ATR exam were also recorded.

2.2.5 Statistical Analysis

Statistical analysis was performed using Microsoft Excel (Microsoft Corporation). Paired Student’s t-tests were used to compare normalized SNR efficiency and normalized CNR efficiency values across all sequences. Differences in normalized SNR efficiency and normalized CNR efficiency were considered to be statistically significant for p-values less than 0.05.

2.3 Results

Radial-ATR produced high quality, multi-planar images with 0.5mm x 0.5mm in-plane resolution following a single 7.7 minute acquisition (Figure 12 & Figure 13). Sagittal image reformat images generated by Radial-ATR sufficiently improve visualization (Figure 12 A, B) to allow for better classification of lesions. An axial-oblique Radial-ATR image reformat (Figure 12 C, D) depicts the presence of an additional small focal full-thickness cartilage lesion on the acetabulum. Sagittal and multi-angle oblique reformat images generated by Radial-ATR, whose orientations are shown in the cross reference image in Figure 13C, are provided in Figure 13B, D. These images demonstrate reduced partial volume artifact that obscures small focal lesions depicted in the sagittal PD-FSE image (Figure 13A).

Radial-ATR exhibited significantly higher ($p<0.05$) normalized SNR efficiency for cartilage and fluid when compared to the 2D FSE sequences (Figure 14a). The FSE sequences exhibited significantly lower ($p<0.05$) normalized SNR efficiency for bone marrow. Radial-ATR also demonstrated significantly higher ($p<0.05$) normalized CNR efficiency between cartilage and fluid as well as significantly higher ($p<0.05$) normalized

CNR efficiency between cartilage and bone when compared to T1-FSE, T2-FSE, and PD-FSE (Figure 14b).

VIPR had 75% sensitivity and 90% specificity for detecting 26 cartilage lesions within the hip joint. VIPR had 100% sensitivity for detecting 20 acetabular labral tears. All patients had labral tears at surgery so specificity could not be calculated.

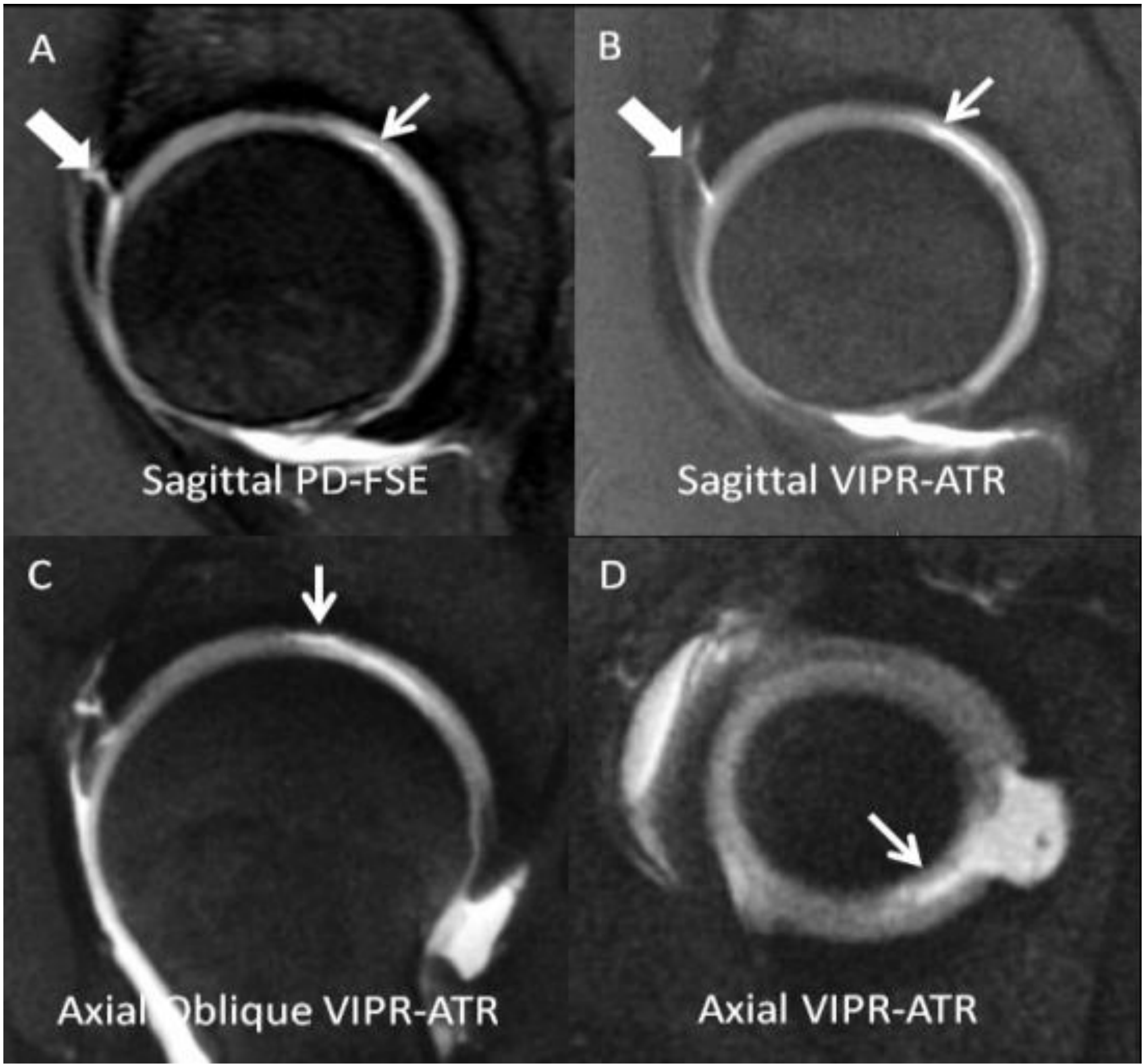

Figure 12 (A) Sagittal PD-FSE image with 4mm slice thickness shows a labral tear (large arrow) and contrast between the articular surfaces suggesting a cartilage lesion (small arrow). (B) Sagittal Radial-ATR reformatted image with 1.5mm slick thickness shows the labral tear (large arrow) and improved visualization of a small focal partial-thickness cartilage lesion on the femoral head (small arrow). (C) Axial-oblique and (D) axial Radial-ATR images (1.5mm slick thickness) show a small focal full-thickness cartilage lesion on the acetabulum (arrow in c) and small focal partial-thickness cartilage lesion on the femoral head (arrow in D). Note that while the (A) Sagittal PD-FSE image exhibits the highest SNR, due to the higher signal achieved with a 4mm slice, each of the (B-D) Radial-ATR reformatted images provide increased conspicuity of pathology due to reduced partial volume artifact from the acquisition of much thinner slices.

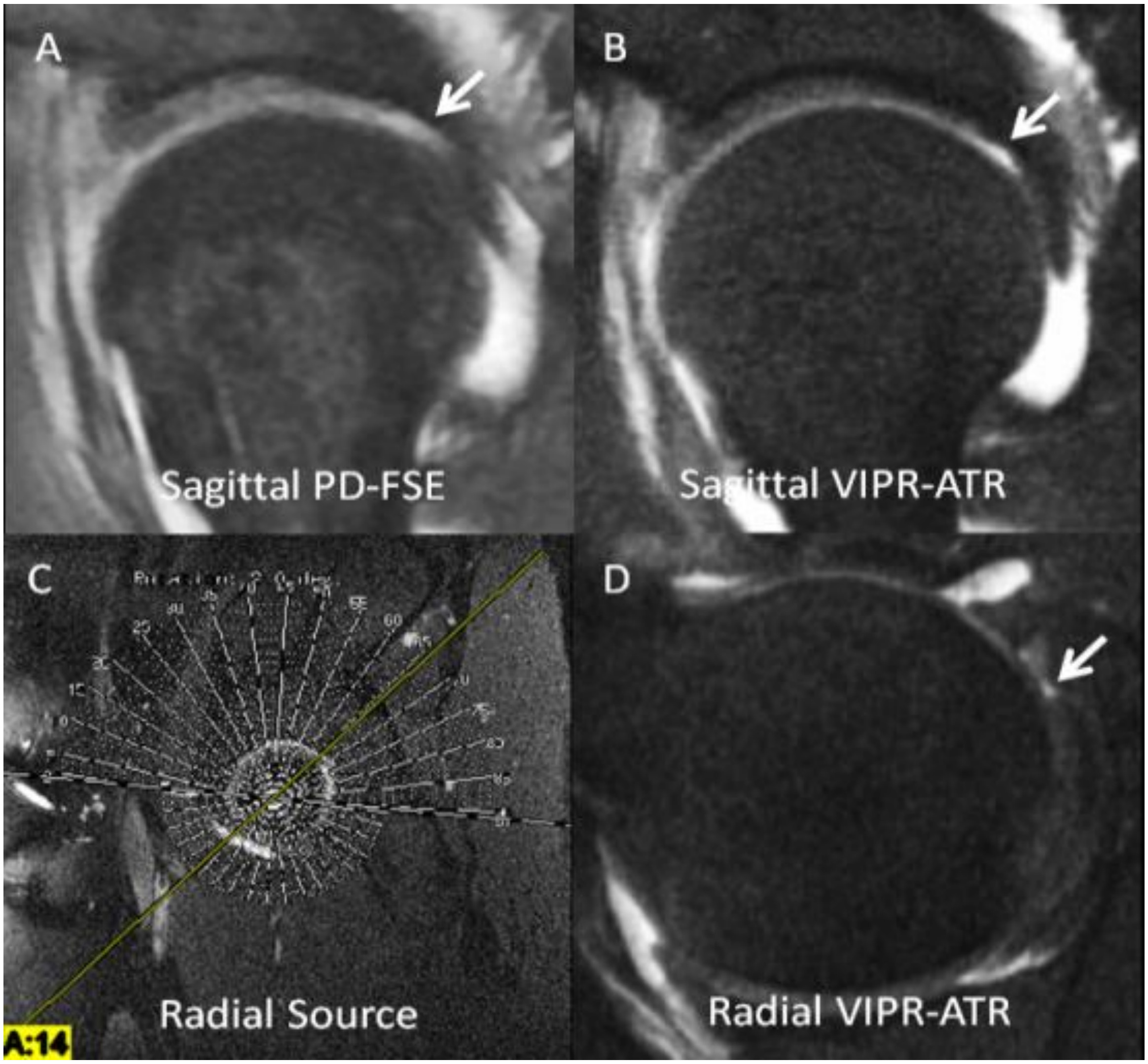

Figure 13: (A) Partial volume effect in this Sagittal PD-FSE image seems to depict healthy tissue (arrow) whereas the thinner slices of Sagittal (B) and radial (C,D) Radial ATR reformat images show a small focal full-thickness cartilage lesion on the acetabulum (arrows in B and D).

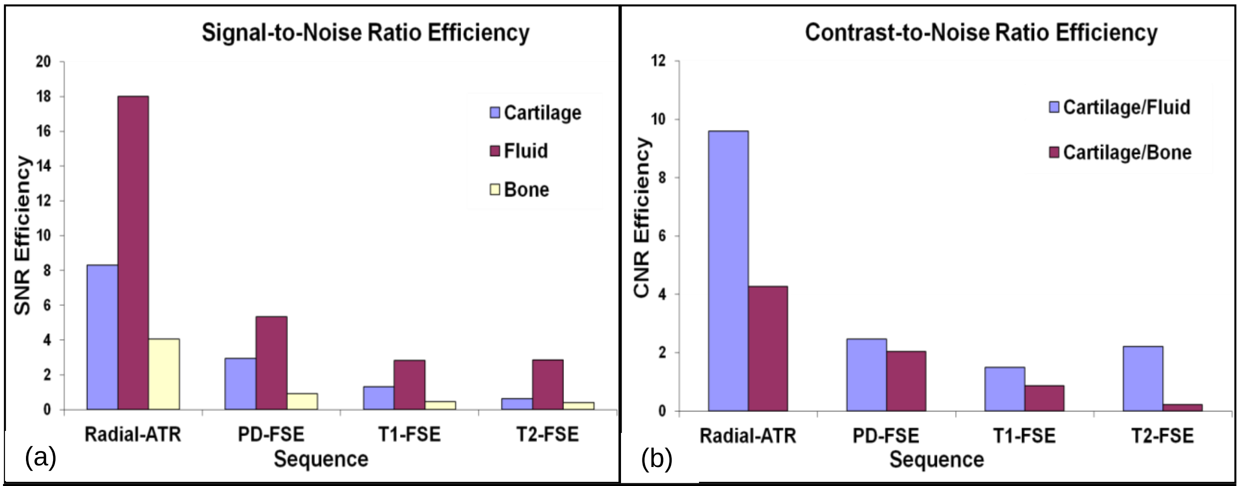

Figure 14: Comparison of (a) normalized SNR efficiency and (b) normalized CNR efficiency for the cartilage imaging sequences. Radial-ATR had significantly higher normalized SNR and CNR efficiency than the 2D FSE sequences.

2.4 Discussion

Radial-ATR ranked highest in normalized SNR efficiency for cartilage and fluid, followed by PD-FSE, then T1-FSE and T2-FSE. As a bSSFP acquisition, Radial-ATR is capable of providing much higher fluid and cartilage signal during each TR than the FSE sequences, explaining its highest rank in these two categories. The high SNR efficiency of Radial-ATR is also attributed to the fact that this sequence uses more of the available TR for data acquisition since it does not require separate prewinder or rewinder pulses [2, 10].

With the highest normalized SNR efficiency for bone marrow, Radial-ATR ranked last in ability to suppress bone marrow signal. The Radial-ATR sequence creates a narrow, frequency-selective stop-band over fat resonance that loses effectiveness in areas of increased field inhomogeneity, which possibly explains its lowest rank for fat-suppression. In the study presented here, the regions of the Radial-ATR images that suffered from suboptimal fat-suppression were those that were excluded from the shim volume; however, the hip joint and surrounding structures that were adequately shimmed demonstrated good fat-suppression.

Radial-ATR ranked highest for normalized CNR efficiency between cartilage and fluid due to its ability to generate high cartilage signal and very high fluid signal that together provide two to eight times as much contrast between these two structures of the hip joint as the FSE sequences. While the FSE sequences generate fluid signal that is about twice that of cartilage, the difference in these signals is not as large as that achieved by Radial-ATR. This substantially higher normalized CNR efficiency between cartilage and fluid led to increased depiction of small focal cartilage lesions.

Despite its low ranking for fat-suppression, Radial-ATR ranked highest for normalized CNR efficiency between cartilage and bone. This high ranking is probably a result of the substantially higher cartilage signal produced by this acquisition compared to the FSE sequences.

The Radial-ATR sequence acquired 0.5 x 0.5 x 0.5 mm^3 voxels that provided multi-planar reformat images with 0.5mm x 0.5mm in-plane resolution. The benefits of the high resolution, multi-planar reformats were substantial: they revealed small focal, full-thickness cartilage lesions that were obscured in the sagittal PD-FSE acquisitions. The ability of Radial-ATR to achieve high isotropic resolution, high SNR efficiency, and versatile bSSFP soft-tissue contrast increased visualization of the cartilage and surrounding structures of the hip joint when compared to the 2D FSE sequences.

There were several limitations in this study. First, Radial-ATR was the only 3D cartilage imaging sequence used in this study. The use of other isotropic, 3D imaging sequences such as FSE-Cube could have been useful; however, these sequences require substantially longer times to achieve spatial resolutions comparable to Radial-ATR [40]. Their use in this study would not have been feasible for this scan-time-limited clinical research study. Since this is the first study which utilizes Radial-ATR with symptomatic patients, a first comparison with the standard clinical imaging sequences was appropriate. This study was also limited by small sample size despite its use of cross-correlation metrics to compare the number, type, and severity of joint abnormalities observed in the MR images with those actually found during subsequent surgical arthroscopy. A study that includes a larger population size and surgical cross-correlation would exhibit higher statistical power and would better accurately determine the specificity and sensitivity of Radial-ATR to detect cartilage lesions, labral tears, and other deformities of the hip joint.

All previous studies describing the use of 3D sequences for evaluating the hip joint have used spoiled gradient-echo (SPGR) sequences with anisotropic resolution [34, 41]. Radial-ATR has been shown to have higher SNR efficiency than other currently used 3D techniques [10], and it can produce high quality multi-planar images of the hip joint with 0.5 mm isotropic resolution in 7.7 minute scan time. Radial-ATR has high cartilage SNR efficiency, high synovial fluid SNR efficiency, and high contrast between cartilage and adjacent joint structures, making it an attractive imaging sequence for MR arthrography of the hip.

In conclusion, Radial-ATR acquires thin continuous slices with high in-plane resolution, which reduces partial volume averaging, and its ability to create reformat images in any plane is especially useful when evaluating the complex, curved anatomic structures of the hip joint. The ability of Radial-ATR to acquire small voxel volumes and then reformat images in any orientation with minimal amounts of slice averaging produces 50% higher in-plane resolution, 90% reduction in voxel volume, and higher SNR and CNR efficiencies compared to 2D FSE sequences in exchange for a 100% increase in scan time. This trade-off may be acceptable, especially since the highly versatile bSSFP tissue contrast of Radial-ATR may allow radiologists to evaluate the menisci, ligaments, bone marrow, and other joint structures which could serve as sources of pain for patients with hip joint abnormalities. Additional studies are needed to determine the potential applications of Radial-ATR to provide “whole-volume” comprehensive assessment of the hip joint in clinical practice.

2.5 Acknowledgements

This work was supported by NIAMS U01 AR059514 and GE Healthcare.

Chapter 3 icones: 3D Isotropic, High Resolution, Rosette-like Sampling Pattern

As previously described in Chapter 1, the out-and-back, 3D-PR sampling scheme with bipolar gradient readout achieves nearly twice the data acquisition efficiency of Cartesian acquisitions, leading to increased readout time, higher spatial resolution, and higher SNR. Despite its performance achievements, the 3D-PR scheme also demonstrates some inefficiency in data acquisition since the speed of the encoding gradients must slow to zero at the edge of k-space before the trajectory returns to the k-space origin. We have developed an isotropic, dual half-echo 3D rosette-like sampling pattern (Figure 15), termed icones, which improves upon the sampling inefficiency of the out-and-back, 3D-PR trajectory while maintaining the same tight TR or echo spacing constraints. In this chapter, we provide a detailed description of the icones trajectory, including the algorithms for designing the 2D base icone petal, rotating the petal to sample 3D k-space, and implementation on the MR scanner system. Additionally, we provide high resolution images of the knee and brain.

3.1 Introduction: Basic description of icones trajectory and potential benefits

The 3D icones sampling pattern is an isotropic, dual half-echo acquisition that is more SNR efficient than the out-and-back, 3D radial trajectory while maintaining the same TR constraints. Icones exhibits freedom to change direction over wide curvatures as it nears the edge of k-space, making efficient use of the available time within the TR interval for spatial encoding. A 2D petal-shaped sampling pattern is generated using a pair of fully balanced gradients (Figure 15a), denoted G_x and G_y in this document. This petal is then rotated in k-space, once for each TR, to generate a 3D sampling pattern that overlaps in the outer regions of k-space. A 2D rendition (Figure 15d & Figure 16) demonstrates the degree to which overlapping may be achieved. The G_x gradient is similar to a bipolar trapezoid (Figure 15b), but with a modified bridge, so that with G_y the trajectory curves along the arc of a circle before reaching the periphery of k-space to maintain nonzero velocity while sampling high frequencies. With this gradient waveform design, icones can utilize the tight TR or echo spacing constraints often used respectively in SSFP imaging and robust fat/water separation methods.

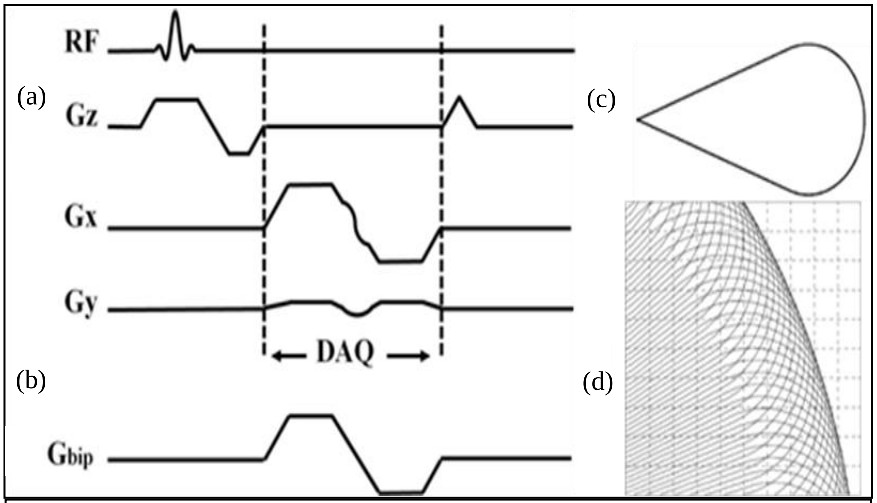

Figure 15 (a) SPGR implementation of iCones, (b) bipolar gradient for comparison. iCones gradients generate a trajectory (c) similar to one leaf of a rosette sampling pattern. A 2D depiction (d) of the overlapping trajectory is provided for illustration. Note, the parameter skip = 17 in (c) and (d).

The icones trajectory is characterized by an undersampling factor describing the separation of acquired k-space points relative to the Nyquist sampling criterion. For the 3D out-and-back radial trajectory, the region of highest undersampling occurs along the outermost edge of k-space at k_{max}. With icones, however, the greatest undersampling occurs near the radial distance where the petal transitions from a straight to circular path. We term this radius k_{spoke} (shown in Figure 16 & Figure 17).

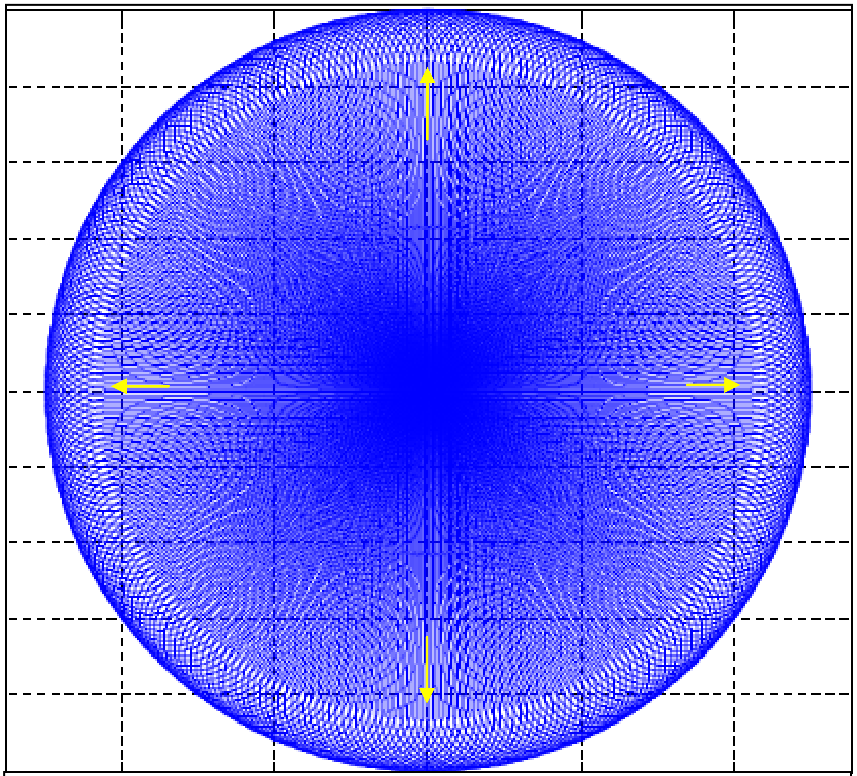

Figure 16 In icones, the most undersampling occurs near the spoke radius k_{spoke} (yellow arrows)

The expected benefits of this trajectory are a reduction in undersampling artifact for a given number of readouts (and hence acquisition time) or a reduction in acquisition time for a given undersampling factor, when compared to the 3D, radial out-and-back trajectory. It is the choice of the imaging scientist or prescribing clinician to determine which of these two performance benefits will be utilized.

3.2 Methods: Designing the sampling pattern, data acquisition, and image reconstruction

The icones pulse sequence waveforms are generated numerically using considerations based on the desired field of view, matrix size, undersampling factor (US), allowable overlap of the petals (referred as the integer-valued ‘skip’ parameter in this document), peak gradient amplitude (G_{max}) & slew-rate (S_{max}) limits, and temporal sampling interval, dt. The waveforms are designed to be as short as possible while adhering to a fixed spatial resolution and undersampling factor.

3.2.1 Creating the 2D petal

A single, 2D icones petal is composed of two straight, equal length spokes that are separated by an angle, θ, and are connected by the arc of a circle of radius R. Since the spokes are straight, we refer to this petal as rosette-like; whereas, a rosette pattern is curved along the entire path. The main ideas behind creating the 2D, out-and-back petal in the k_x-k_y plane, as illustrated in Figure 17, are (a) adherence to system hardware constraints to create an outbound trajectory with (b) the outermost sample located at $(k_x,k_y,k_z) = (k_{max},0,0)$ and (c) reflection about the k_x axis to obtain the inbound path.

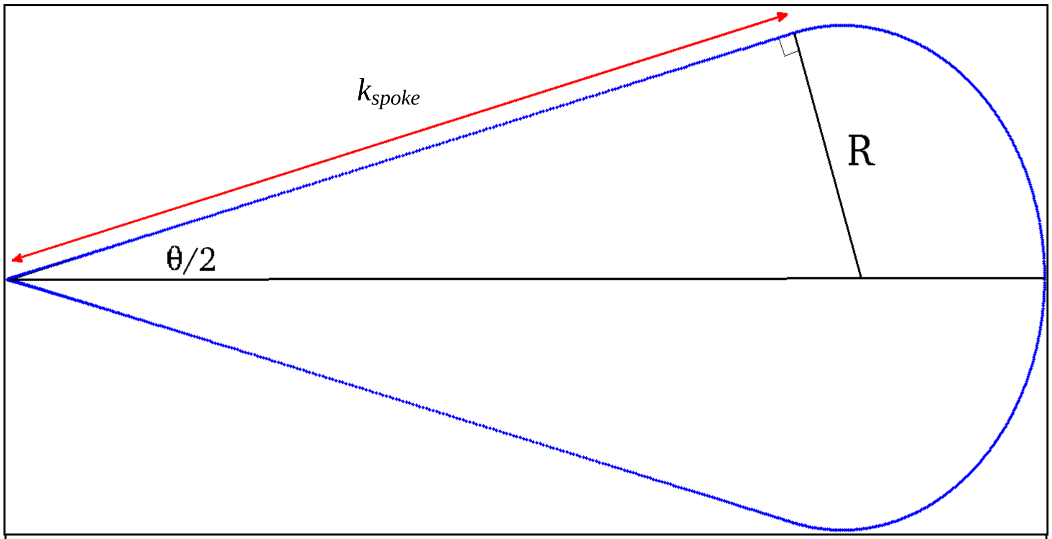

Figure 17: Design of the fundamental icone petal: the icones petal is composed of two radial-like spokes and a circular arc. The circular arc covers more unique k-space points (near k_{max}) per TR than the fundamental out-and-back 3D-PR trajectory.

Constructing a single petal, as illustrated in Figure 17, requires a spoke length k_{spoke}, desired undersampling factor (US), FOV, 'skip' factor (s), S_{max}, G_{max}, and dt. Using these parameters, the angle between the two spokes of the icones petal is calculated with the following equation:

$$\frac{\theta}{2} = \arctan\left(\frac{(1+2\cdot s)\cdot dk \cdot US}{2\cdot k_{spoke}}\right) \tag{10}$$

where dk is the step-size in frequency space and satisfies the relationship $dk = 1/FOV$. Since arctan(x) is an increasing function, this equation reveals that increasing dk, s, and/or US results in a larger angle θ, hence a wider petal with a longer arc along the edge of k-space, yielding more overlap at high frequencies. Increasing the spoke lengths, k_{spoke}, decreases the angle between them when all other variables are held constant.

Using the gradient system specifications and desired imaging parameters, one spoke and half of the circular arc are designed for the outbound portion of the petal. First, the radius of the circle is calculated, with $R = k_{spoke}\tan(\theta/2)$. Next, one determines if the k-space velocity along the arc will be limited by S_{max} or G_{max}. This constraint determines the time required to sample the arc, the speed along the spoke when connecting to the arc, and consequently the shape of the gradients generating the spoke. If $\sqrt{S_{\max} R/\gamma} < G_{\max}$ (i.e. slew-rate limited along the arc) and k_{spoke} dimension is sufficiently large, then a trapezoid-like pulse is used to generate the spoke (Figure 18a-b). Otherwise, for smaller k_{spoke} designs and / or faster slew rate gradient systems, when $\sqrt{S_{\max} R/\gamma} \geq G_{\max}$ along the arc, a triangular pulse generates the spoke (Figure 18c).

Once the gradients for the spoke are determined, sinusoidal gradient waveforms are generated for the arc. The outbound path is thus complete, with k-space traversal simply due to successive application of these spoke- and arc-generating waveforms. Finally, the inbound path is generated by reflection of the outbound trajectory about the k_x axis, generating a symmetric, 2D icones petal.

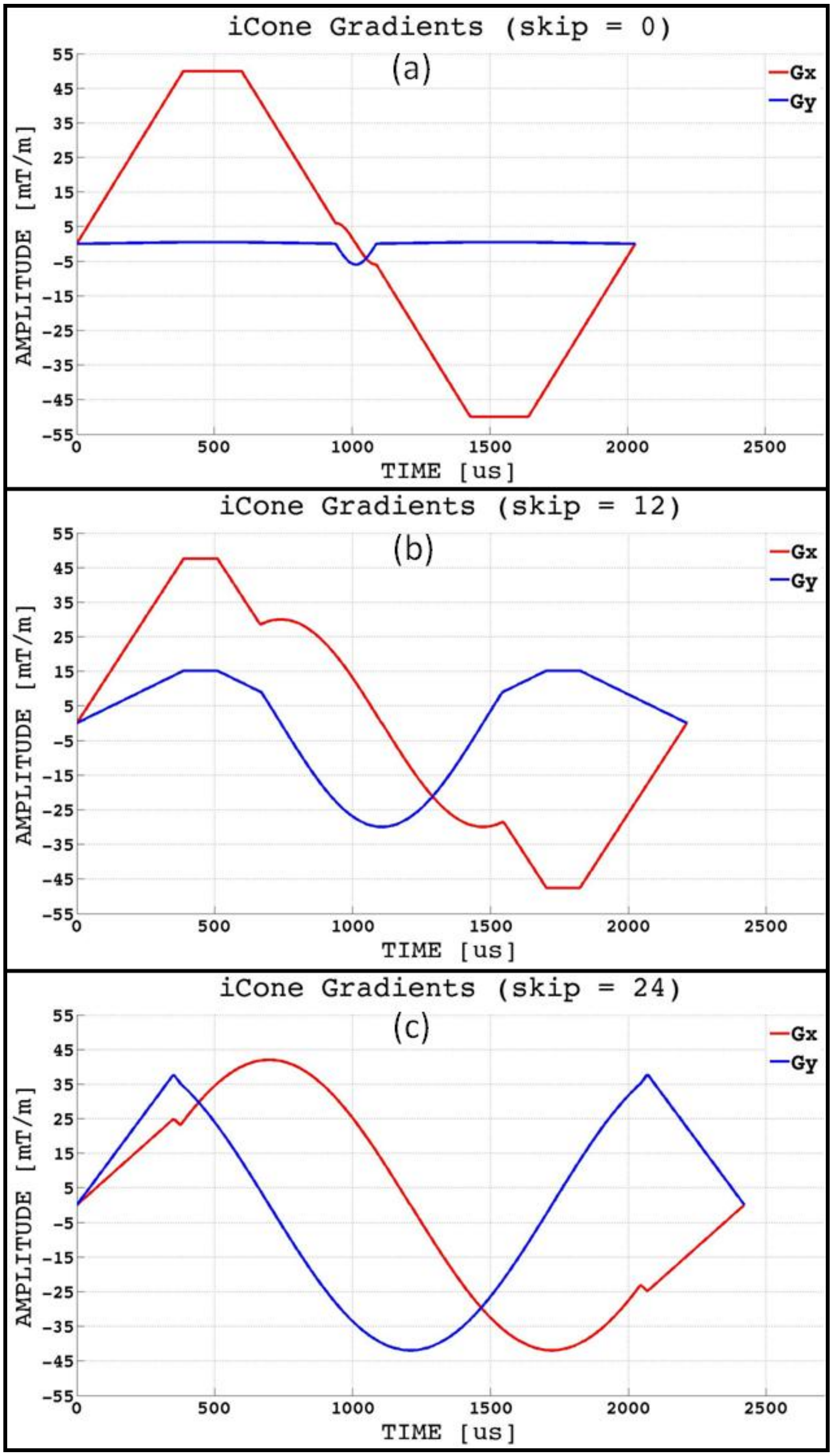

Figure 18: The spoke portion of the icones gradient waveforms (i.e. the two non-sinusoidal sections of each pulse) changes from (a, b) trapezoidal to (c) triangular as the allowable petal overlap (i.e. skip) increases. The arc portion of the gradient waveforms, represented by sinusoids, lengthens as the overlap / skip increases.

For any given set of imaging and hardware parameters, the icones petal is designed for the width defined by equation (10) by determining the optimal value of k_{spoke}. The optimal k_{spoke} is found through an exhaustive search process such that the petal will sample up to k_{max} but not beyond it. Using the aforementioned design method, the exhaustive search is accomplished by attempting to design petals whose values of k_{spoke} range from 1 to k_{max} where units are given in k-space samples beginning at the k-space origin. Since the maximum spatial frequency sampled on the arc is limited by the spoke length, k_{spoke}, the angular separation, θ, and the radius, R, of the circle along which the arc resides, most petals will not sample a large enough frequency to achieve the desired spatial resolution (**Figure 19**b), others will achieve higher resolution than requested (**Figure 19** f), and a few will nearly achieve the desired resolution (**Figure 19**d). From the subset of petals achieving spatial resolutions close to the desired value, the petal with maximum k_x component closest in value to k_{max} is determined to be the optimal petal.

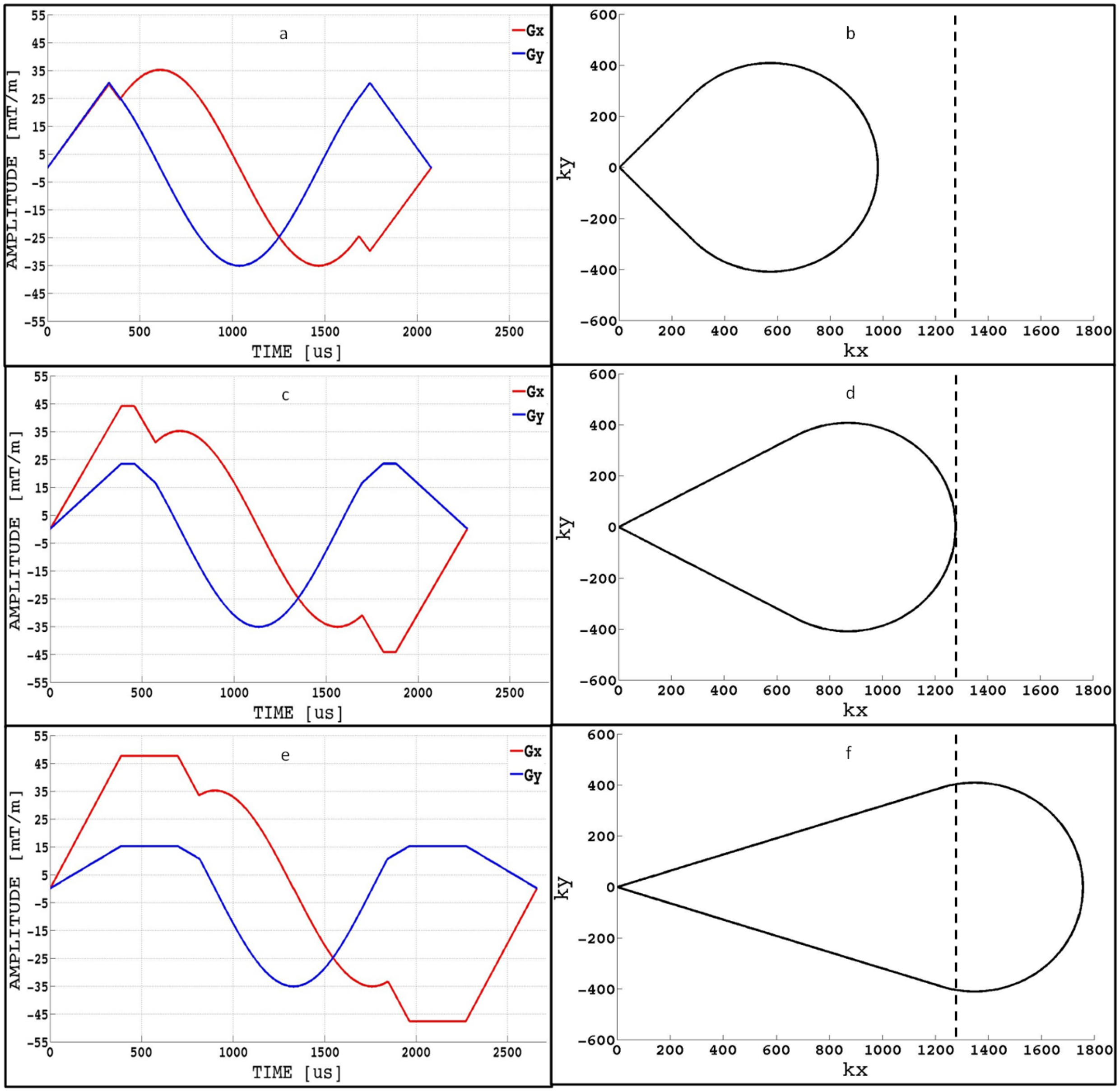

Figure 19: The icones algorithm determines the optimal petal size using an exhaustive search approach. Many trial petals have a largest sampled frequency that is too low (b) or too high (f) compared to the desired maximum spatial frequency, indicated by the black dashed vertical line. The petal with a maximum frequency that achieves the desired spatial resolution (d) is chosen. For each trial icones base petal (b,d,f) the corresponding pair of gradients creating the 2D trajectory is displayed on the left (a,c,e).

3.2.2 Developing a 3D Trajectory from the 2D petal

3.2.2.1 Strategy for distributing anchor points on sphere of radius k_{rad}

Icones effectively cover a k-space sphere in fewer excitations than the out-and-back 3D-PR trajectory by moving the point of lowest sampling density from k_{max} in to k_{spoke}. To determine how to rotate the icones petal to sample the 3D space, a set of N "anchor points" are distributed on the sphere of radius k_{spoke} whose surface is defined by $k_x^2 + k_y^2 + k_z^2 = k_{spoke}^2$. This sphere resides in the region where the sampling density is a minimum, so the distribution of the anchor points at this k-space radius is important to achieving the level of undersampling desired by the user. The coordinates of these anchor points are determined by a parameterization process with dimensionless parameter, *t,* which varies in small, constant increments, *dt*, between -1 and 1-*dt.* The parameter, *t*, is then utilized to calculate spherical polar angles, ϕ, and azimuthal angles, η, for the anchor points. The spherical coordinates (k_{spoke}, ϕ, η) of these anchor points are then transformed into Cartesian coordinates (k*x*,k*y*,k*z*). More details about this parameterization process are provided below.

3.2.2.2 Parameterization of the anchor points

The parameterization of *t* begins with determination of an appropriate step size, denoted *dt*. The step size is calculated from the undersampling factor (*US*), field-of-view (FOV), and the radius, k_{spoke}, of the sphere upon which the anchor points reside:

$$dt = \frac{dk^2 \cdot US}{2\pi \cdot k_{spoke}^2} \tag{11}$$

where *dk* = 1/FOV.

Once the parametric step size *dt* has been determined, we can use it to calculate the total number of points, *N*, needed to sample the sphere of radius k_{spoke}:

$$N = \frac{2}{dt} \tag{12}$$

N must be an even integer, since there are two anchor points per petal, so if necessary, its value is rounded down to the nearest even integer. The complete set of values for the parameter *t* is then determined from *dt* and *N*:

$$t_j = -1 + dt \cdot j \tag{13}$$

where *j* = 0, 1, 2…*N*-1. With this parameterization, the values t_j reside in the interval [-1,1-*dt*].

Once the t_j have been determined, they can be used to calculate the set of spherical polar angles, ϕ_j , and azimuthal angles, η_j , of the N anchor points. The parameterizations for these angles are:

$$\begin{aligned} \phi_j &= \cos^{-1}(t_j) \\ \eta_j &= \frac{\pi \cdot k_{spoke}}{dk} \sin^{-1}(t_j) \end{aligned} \tag{14}$$

The formula for polar angle, ϕ_j , yields a trajectory that follows a smooth path along the k_z dimension from the south pole ("$-k_z$") to the north pole ("$+k_z$"). In the calculation of azimuthal angle, η_j , the ratio $\frac{\pi \cdot k_{spoke}}{dk}$ controls the angular rotation rate of the trajectory about the k_z-axis. It increases for larger values of k_{spoke}, corresponding to narrow trajectories with little or no overlap and, therefore, several readouts. The angular rotation decreases for smaller values of k_{spoke}, or trajectories characterized by wide petals with high degree of overlap and relatively small number of readouts.

Starting with the set of parameterized spherical coordinates (k_{spoke}, ϕ_j, η_j) one can compute the Cartesian coordinates (kx_j, ky_j, kz_j) of the anchor points:

$$\begin{aligned} kx_j &= k_{spoke}\cos(\eta_j)\sin(\phi_j) \\ ky_j &= k_{spoke}\sin(\eta_j)\sin(\phi_j) \\ kz_j &= k_{spoke}\cos(\phi_j) \end{aligned} \tag{15}$$

As previously mentioned, these anchor points are distributed on a sphere with radius equal to the icone spoke length, k_{spoke}, corresponding to the distance in k-space that the spokes reach (Figure 20a). The distribution of these anchor points forms a smooth, spiraling path from $-k_z$ to $+k_z$ and is similar to the trajectory generated using the method developed by Wong and Roos [42] (Figure 20b).

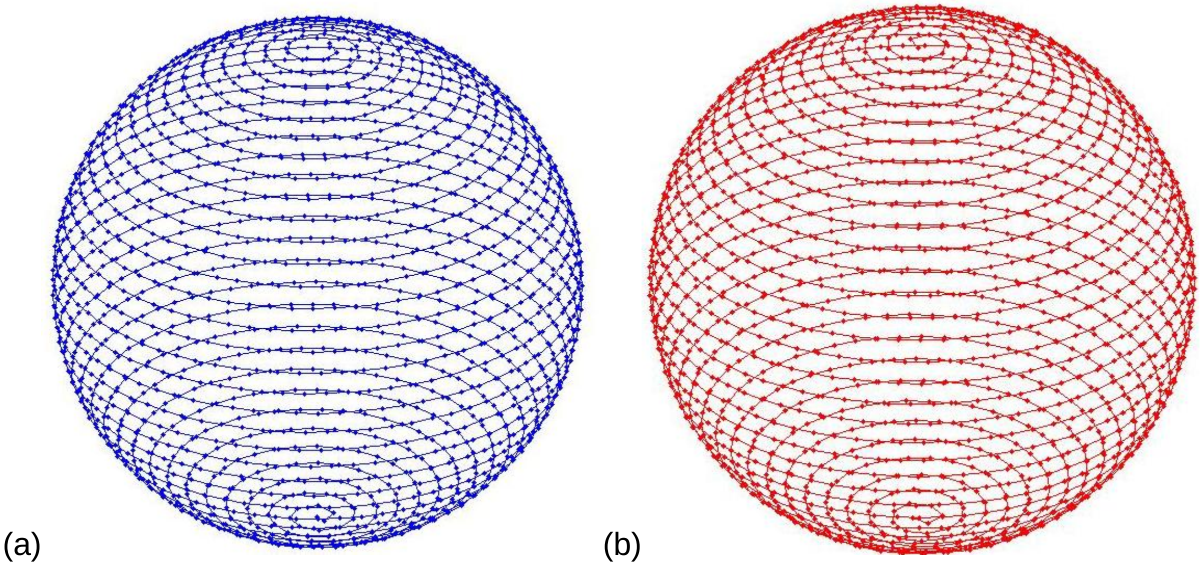
(a) (b)

Figure 20: (a) Anchor points are distributed on a sphere using equation (15). The distribution of these points resembles (b) the distribution that is generated by the method of Wong and Roos [42].

3.2.2.3 Pairing anchor points to define out-and-back paths for each TR

The anchor points generated by equation (15) are ordered sequentially and form a spiral path from $–k_z$ to $+k_z$ (Figure 20a). This sequential ordering is utilized together with the previously mentioned ‘skip’ parameter to gather the anchor points into ‘outbound’ and ‘inbound' pairs that prescribe the direction of the trajectory as it passes through that particular point of the icones petal. For each pair of anchor points, the outbound portion of the icones petal should pass through the anchor point labeled ‘outbound’, and the inbound portion of the same petal should pass through the anchor point labeled as ‘inbound’. This pairing process yields a set of N/2 readouts.

Since the anchor points have been distributed in an ordered fashion via equations (11)-(15), the process for assigning outbound and inbound anchor points becomes relatively straightforward. If we consider the anchor points as belonging to the set A = (1,2,3…,N) of positive integers, then the odd numbered anchor points are generally labeled as “outbound” and the even numbered points are generally labeled “inbound” (**Figure 21**). Some deviations from this nomenclature arise when sampling near the ±kz poles and are discussed below.

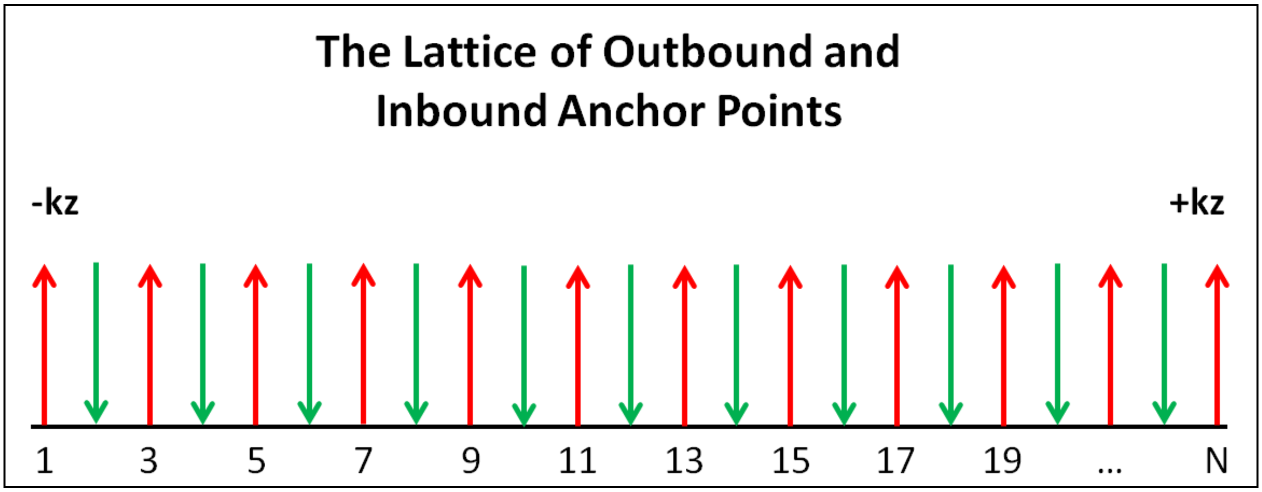

Figure 21: The one dimensional lattice of positive integers can be used to represent the collection of anchor points. The –kz pole is located at 1 and the +kz pole is located at N. With some exceptions, the outbound anchor points are the odd integers and the inbound anchors are even. In this depiction, red upward facing arrows are placed with the outbound anchor points and green, downward facing arrows are placed with the inbound anchor points.

The algorithm for pairing outbound anchor points with inbound anchor points utilizes the non-negative integer-valued *skip* (i.e. *s*) factor together with the integer indexed set of all anchor points, *A*. Given *n,* the index of an outbound anchor point the algorithm ignores the following *2*s* anchor points and yields the index of the next anchor point. More specifically, the algorithm ignores the next *s* outbound anchor points and the next *s* inbound anchor points. In mathematical terms, the index of the inbound anchor point is found by calculating the sum $n+2*s+1$, where *n* is the index of the given outbound anchor point and *s* is the value of *skip*. The unit increment yields an even-numbered index, which is the general rule for labeling inbound anchor points.

For example, if the index of a given outbound anchor point is n=7 and $s = 4$, then to determine the appropriate inbound anchor point, the algorithm skips over (i.e. ignores) the next 4 inbound anchor points, which have indices 8, 10, 12, and 14 (Figure 22). The algorithm then chooses the subsequent inbound anchor point, which has index 16, for the inbound path. Or using the mathematical formula from the previous paragraph, the index of the appropriate inbound anchor point is simply the sum n+2*s+1 = 7+2*4+1, which is 16. Notice that in this process, anchor points 9, 11, 13, and 15 were also ignored since they are labeled as “outbound” and the algorithm can only use an “inbound” anchor point for this step in the pairing process.

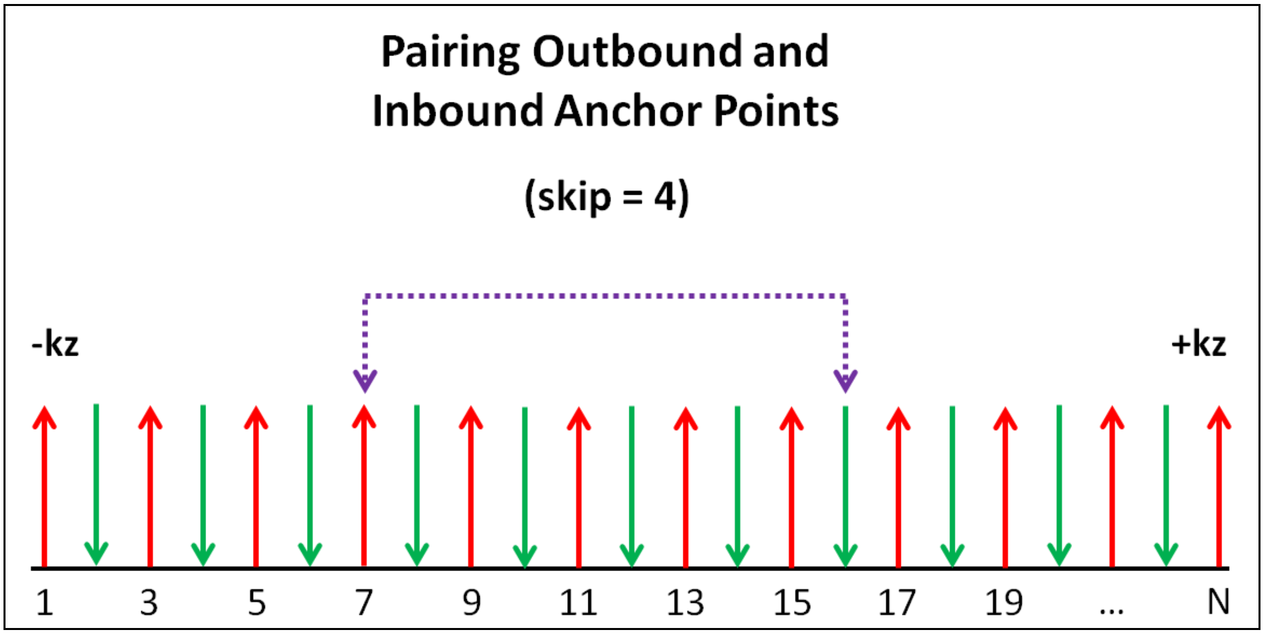

Figure 22: Schematic representation of the process given in equation (16) for pairing inbound anchor points with outbound anchor points. The goal is to determine which green inbound anchor point will be paired with the red outbound anchor point indexed by 7. Given that skip = 4, the algorithm ignores the next 4 green inbound anchor points indexed by 8, 10, 12, and 14. The inbound anchor point located at 16 is then paired with 7.

Expressed as formulas, the majority of the outbound and inbound anchor points are indexed from the set of all anchor points, *A*, and paired according to the following regime:

$$\{outbound, inbound\} = \{2j-1,\ 2j+2s\} \qquad j = 1,2,3,\ldots,\frac{1}{2}N - s \tag{16}$$

Inspection of equation (16) reveals that some of the outbound anchor points near the $-k_z$ pole and some of the inbound anchor points near the $+k_z$ pole have not been paired. The points near $-k_z$ are grouped into outbound-inbound pairs using a slightly different scheme:

$$\{outbound, inbound\} = \{2j,\ 2j+s\} \qquad j = 1,2,3,\ldots,\frac{1}{2}s \tag{17}$$

Anchor points near the $+k_z$ pole, are grouped into pairs using yet another scheme:

$$\{outbound, inbound\} = \{2j+(N-2s-1),\ 2j+(N-s-1)\} \qquad j = 1,2,3,\ldots,\frac{1}{2}s \tag{18}$$

Altogether, equations **(16)**-**(18)** are used to pair every anchor point that is generated by equation (15). There is one subtle difference between the pairs formed with equation (16) and those formed with equations **(17)** and **(18)**. Equations **(17)** and **(18)** utilize only half of the value of the *skip* parameter, thereby generating 3D icone petals that are narrower than the 3D icone petals generated with equation (16), leading to increased coverage near the poles.

3.2.2.4 Calculating 3D rotation matrices for each anchor-point pair

After all anchor points have been collected into ordered pairs, they are utilized to create the full 3D trajectory. For each outbound-inbound anchor point pair, a transformation matrix is calculated that maps the base icones petal from the k_x-k_y plane to the plane in 3D k-space defined by the outbound-inbound anchor point pair and the k-space origin

(**Figure 23**). While this transformation matrix so far has been referred to as a single mapping, it is actually the product of three distinct transformations. These three transformations and the methods for calculating them are described below.

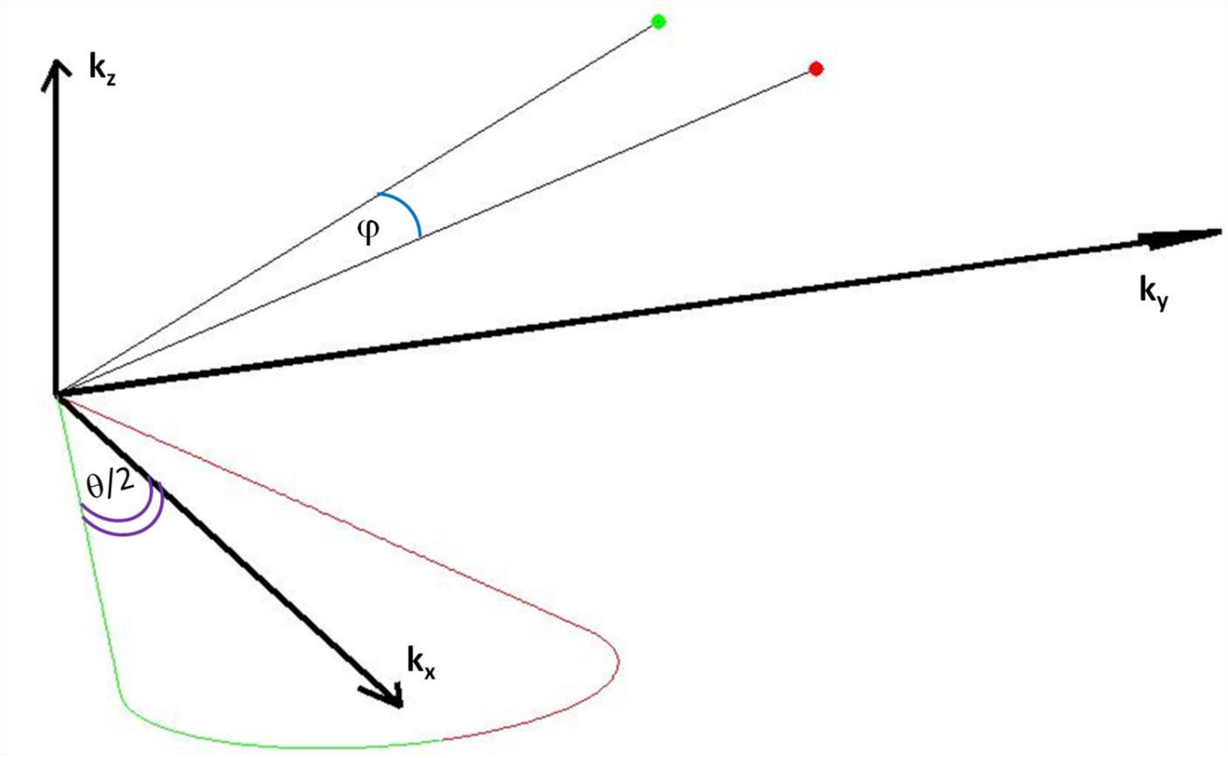

Figure 23: View of 2D icones base petal residing in the k_x-k_y plane and two paired anchor points. The outbound and inbound portions of the trajectory have been shaded in purple and pistachio, respectively. The outbound point is denoted by the red dot and the inbound anchor point is denoted by the green dot. This 2D base petal will be rotated in 3D k-space so that the (purple) outbound and (pistachio) inbound portions of the trajectory pass through the red outbound and green inbound anchor points, respectively.

Transformation 1: Narrowing the icone base petal before mapping into 3D k-space

For a distortion-free mapping of the 2D base icone petal into the plane spanned by the origin and the two anchor points the angle, φ, between the two vectors emanating from the origin to the outbound-inbound anchor point pair and the angle, θ, between the spokes of the 2D base icone petal, must be equal. This is not true in general, and in fact, φ is typically smaller than θ. Consequently, when φ ≠ θ a transformation is performed to narrow the 2D icone base petal until the angle between the spokes equals φ (Figure 24). This is achieved by scaling the y-coordinates of the 2D base petal by the factor *c*(φ,θ):

$$c(\varphi,\theta)=\frac{\sin(\varphi/2)}{\sin(\theta/2)} \tag{19}$$

This factor can be packaged into the following transformation matrix:

$$T_c=\begin{bmatrix}1 & 0 & 0\\ 0 & c(\varphi,\theta) & 0\\ 0 & 0 & 1\end{bmatrix} \tag{20}$$

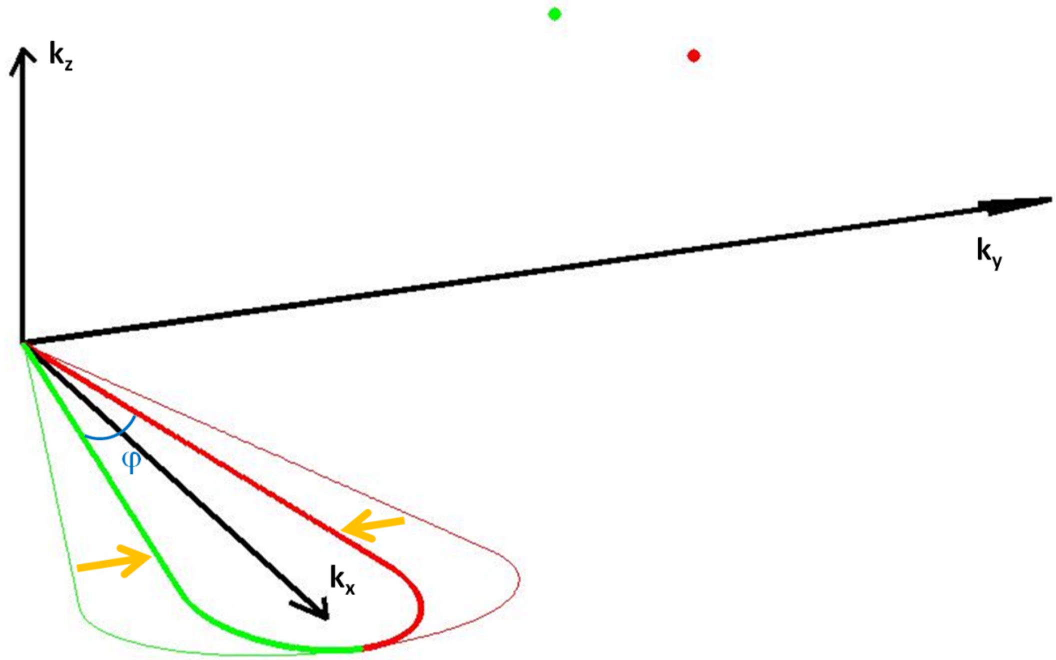

Figure 24: The k_y coordinates of the 2D base petal are scaled by *c*(φ,θ), given by equation (19)**, to reduce the petal aperture to φ, the angle between the outbound and inbound anchor point pair.**

Transformation 2: Aligning the outbound spoke with the outbound anchor point in 3D k-space

After the 2D base icone petal has been scaled with (20), it is rotated in 3D k-space so that the outbound spoke, represented by $\vec{s}_{out}$, coincides with the vector emanating from the origin to the outbound anchor point, represented by $\vec{a}_{out}$ (**Figure 25**). This rotation occurs in the two dimensional plane spanned by $\vec{s}_{out}$ and $\vec{a}_{out}$. The axis of rotation, denoted by $\vec{u}$, is determined by the vector cross product of $\vec{s}_{out}$ with $\vec{a}_{out}$. Specifically, $\vec{u} = \vec{s}_{out} \otimes \vec{a}_{out}$. This is a natural choice for the rotational axis since the vector resulting from the cross product of two vectors is always perpendicular to the two vectors generating it. The angle of rotation about $\vec{u}$ is denoted by α and is determined using the formula for the dot product of two vectors:

$$\alpha = \cos^{-1}\left(\frac{\vec{s}_{out} \cdot \vec{a}_{out}}{\|\vec{s}_{out}\| \cdot \|\vec{a}_{out}\|} \right) \tag{21}$$

While it is possible to develop an algorithm that calculates the 3D rotation matrix that would achieve the desired rotation, a perfectly suitable function already exists within the MATLAB (Mathworks, Inc) scientific programming environment. This function, ‘makehgtform’, accepts as input parameters the axis of rotation, $\vec{u}$, and the desired angle of rotation, α, to calculate the matrix which would correspond to a 3D rotation about $\vec{u}$ by angle α. We have utilized this commercial software for our purpose and denote the 3D rotation matrix that it generates as R_{out}.

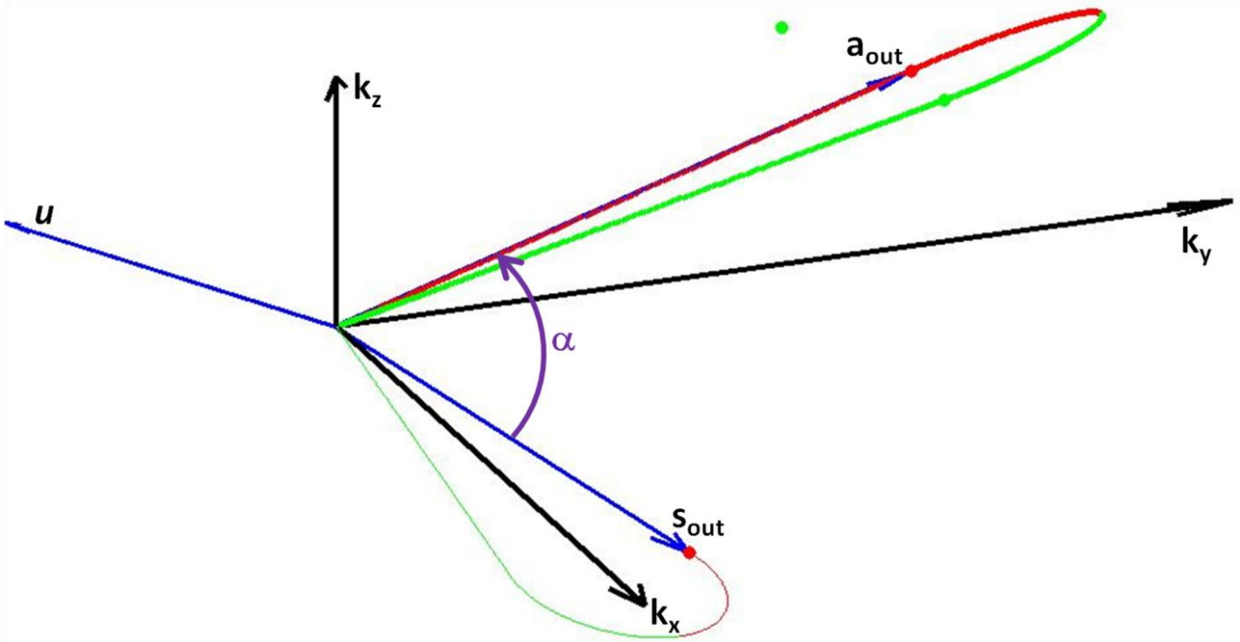

Figure 25: After scaling has been performed with the transformation given by equation (20)**, the petal is rotated about u so that the outbound spoke, denoted s_{out}, aligns with a_{out}, the vector between the origin and the outbound anchor point. The angle of rotation, α, is determined by equation** (21)**.**

Transformation 3: Aligning the inbound spoke with the inbound anchor point in 3D k-space

The transformation described by equation (20) scales the 2D base icone petal, and the transformation of equation (21) rotates the result into 3D k-space so that the outbound spoke coincides with the vector defined by the outbound anchor point. What remains is a transformation that aligns the inbound portion of the trajectory along the segment connecting the origin with the inbound anchor point, $\vec{a}_{in}$. This is achieved via rotation about $\vec{a}_{out}$.

Calculating the rotation about $\vec{a}_{out}$ is a bit involved. It requires the calculation of two useful vectors. The first vector, denoted $\vec{d}_1$, connects the outbound anchor point, $\vec{a}_{out}$, with the transformed unit-length inbound spoke, $R_{out}T_c\hat{s}_{in}$. The second vector, denoted $\vec{d}_2$, connects $\vec{a}_{out}$ with the unit-length inbound anchor point $\hat{a}_{in}$. The equations for $\vec{d}_1$ and $\vec{d}_2$ are:

$$\vec{d}_1 = R_{out} T_c \hat{s}_{in} - \hat{a}_{out} \tag{22}$$

$$\vec{d}_2 = \hat{a}_{in} - \hat{a}_{out} \tag{23}$$

In general, $\vec{d}_1$ and $\vec{d}_2$ are not perpendicular to $\vec{a}_{out}$, but they should be if they will be used to calculate an angle of rotation about $\vec{a}_{out}$. This is accomplished by projecting $\vec{d}_1$ and $\vec{d}_2$ onto the plane that is orthogonal to $\vec{a}_{out}$, and simply involves subtracting the components of $\vec{d}_1$ and $\vec{d}_2$ that are parallel to $\vec{a}_{out}$:

$$\vec{d}_1^{\perp} = \vec{d}_1 - \vec{d}_1 \cdot \hat{a}_{out} \tag{24}$$

$$\vec{d}_2^{\perp} = \vec{d}_2 - \vec{d}_2 \cdot \hat{a}_{out} \tag{25}$$

Now, $\vec{d}_1^{\perp}$ and $\vec{d}_2^{\perp}$ are both perpendicular to $\vec{a}_{out}$, and the angle, β, residing between them is the angle that is needed to align the inbound portion of the transformed icone petal with the inbound anchor point (**Figure 26**). Similar to equation (21), the angle of rotation about $\vec{a}_{out}$ can be determined by utilizing the formula for the vector dot product:

$$\beta = \cos^{-1}\left(\frac{\vec{d}_1^{\perp} \cdot \vec{d}_2^{\perp}}{\left\| \vec{d}_1^{\perp} \right\| \cdot \left\| \vec{d}_2^{\perp} \right\|} \right) \tag{26}$$

Utilization of the MATLAB function ‘makehgtform()’ yields the 3D rotation matrix for this final transformation which is denoted by R_{in}.

After the 3D rotation about $\vec{u}$ has been performed, the inbound spoke of the petal will be aligned with the segment connecting the origin and the inbound anchor point (Figure 27).

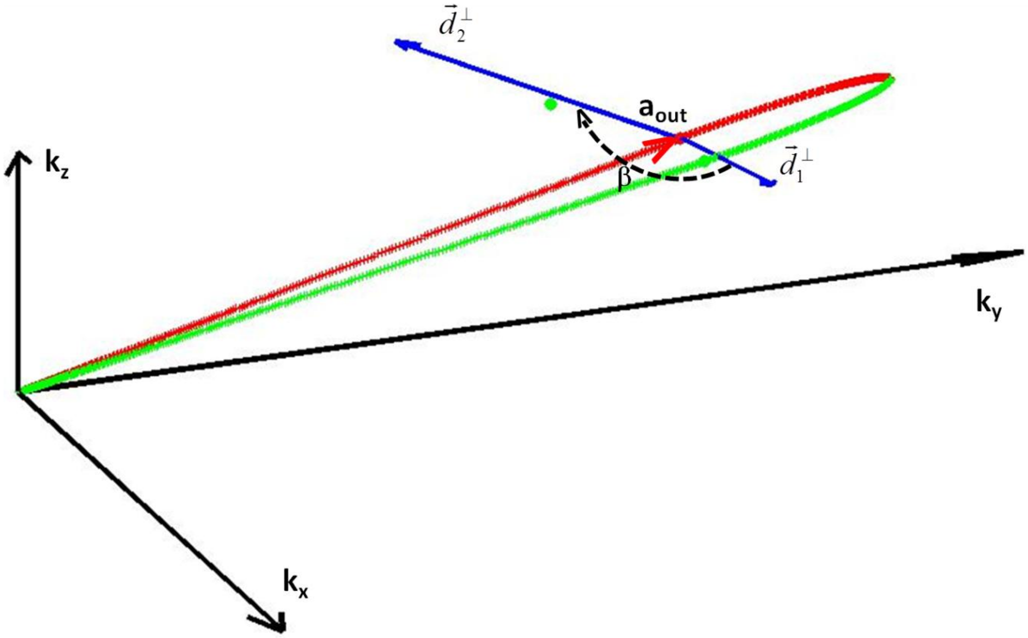

Figure 26: The third transformation is a rotation of the petal about the vector extending to the outbound anchor point, a_{out}. The angle of rotation, β, is determined by vectors $\vec{d}_1^{\perp}$ and $\vec{d}_2^{\perp}$.

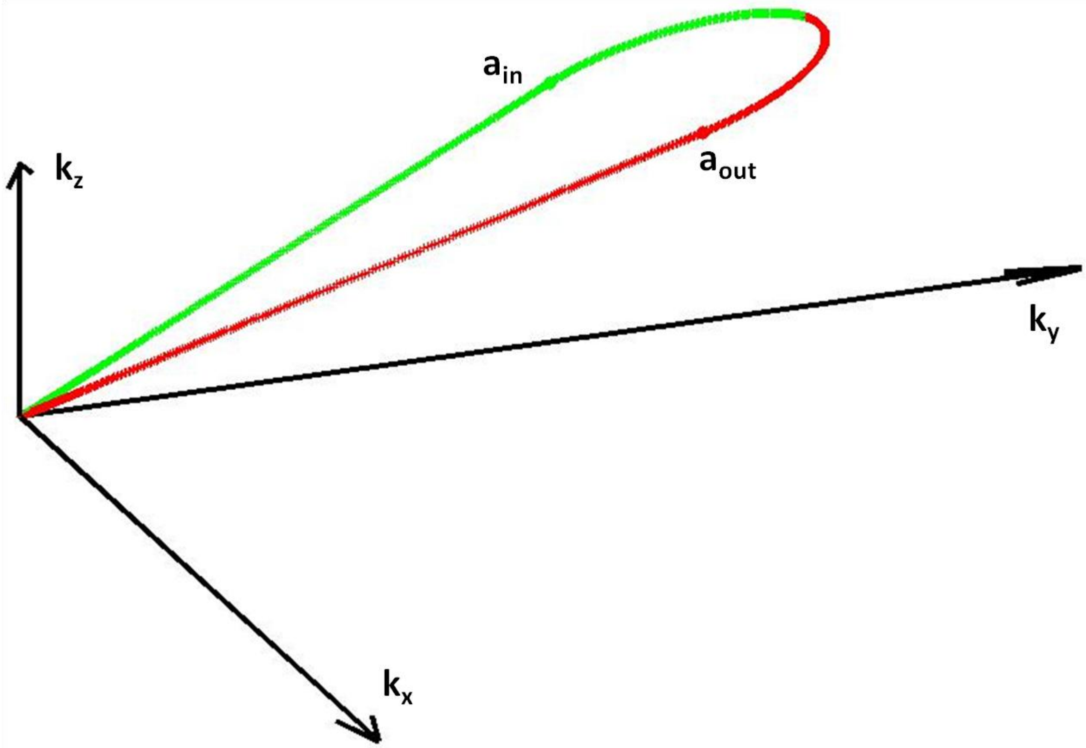

Figure 27: After all three transformations have been applied to the 2D base petal, the icone petal passes through the outbound-inbound anchor point pair.

Combining transformations to produce one final rotation matrix

For each outbound-inbound anchor point pair, sequential application of T_c, R_{out}, and R_{in} yields a single rotation matrix that maps the 2D base icones petal into 3D k-space:

$$R^{(j)} = R_{in}^{(j)} R_{out}^{(j)} T_c^{(j)}, \qquad j = 1,2,3...,N/2 \qquad (27)$$

where the super script indices, *j*, denotes that these transformations are used for the *j*th excitation. The full 3D icones sampling pattern for a dual half-echo imaging exam is achieved by application of each of these unique rotation matrices, once every TR, to the 2D icones petal. The traversal of the sphere with radius k_{max} is similar to that of the 3D radial, out-and-back VIPR trajectory. The main difference is that the icones petal punctures the sphere only once per TR; whereas, the analogous “half bow-tie” pattern of the bipolar 3D-PR trajectory samples the sphere twice per TR since it uses a point-pairing scheme along the larger sphere with radius k_{max}.

3.2.3 Implementing icones as a pulse sequence on MR scanners

Since the full 3D icones sampling pattern is generated by multiplication of 3x3 matrices with the icone base petal, it is natural to consider implementing the sampling pattern on the scanner system using an extension of this concept. This could be achieved by multiplying the 3D scanner coordinate matrix, *S*, with the 3D icones rotation matrix, $R^{(j)}$, and re-assigning the system coordinate matrix with the result (i.e., $S \cdot R^{(j)}$). This effectively rotates the two base icones encoding gradients from the logical axes onto the appropriate physical axes. An alternative method of generating the full trajectory utilizes gradient waveform memory. This method requires pre-calculating the full set of unique encoding gradient waveforms, saving all of them to the gradient waveform memory space on the scanner system, and then accessing the appropriate, unique gradient waveforms for readout. This method requires more computer memory than is available on the gradient sequencer hardware at this time and also costly waveform memory transfer delays that would extend the TR interval, so it was not implemented in this work. Consequently, the method of repeatedly re-assigning the scanner coordinate matrix to a new value was utilized here. More details on its implementation are provided next.

To rotate the encoding gradients without affecting the excitation or spoiling waveforms the pulse sequence was implemented as three modules of instructions. These modules are: (1) excitation pulses, (2) encoding gradients, and (3) the option of spoiler gradient waveforms for SPGR acquisitions, or a second set of excitation pulses for ATR acquisitions. For SSFP acquisitions that require only one excitation, modules 1 and 2 are used consecutively and together constitute one repetition time. For SPGR or ATR acquisitions, all three modules are used in consecutive order for each TR.

Approximately two hundred microseconds are reserved at the beginning of each of the pulse sequence modules for scanner system updates. This overhead time is meant for adjustments to RF and gradient waveforms, and also modifications to the scanner system coordinate matrix. In the implementation of the icones trajectory presented here, the scanner system coordinate matrix is explicitly altered during every one of the system updates. For the module corresponding to RF excitation, the scanner coordinate matrix is set to the default scanner coordinate matrix, S, that the system calculates for the prescribed imaging plane. The logical RF and gradient waveforms are properly transformed to the appropriate physical axes under S when this portion of the sequence is executed. Then, during the system update time for the module containing the encoding gradients, the scanner coordinate matrix is set to $S \cdot R^{(j)}$, the product of S and the jth unique 3D icone rotation matrix. Under coordinate matrix $S \cdot R^{(j)}$, the two basic icones encoding gradients are transformed so that the desired rotation of the 2D base icone petal is achieved in 3D k-space. For scans that utilize the third module of instructions, the scanner coordinate matrix is reset to *S* prior to waveform generation. Under *S,* the waveforms responsible for spoiling or secondary excitation are mapped to the proper physical axes. Overall, this three-module implementation achieves proper rotation of the icones encoding gradients while also preserving the excitation and spoiler waveforms.

While this three-module pulse sequence implementation is effective, it requires three times the system overhead that is required for a pulse sequence that has all waveforms and instructions contained in a single module. As previously mentioned, each module currently requires approximately 200 microseconds of overhead time to perform system updates. System overhead time is included as part of the repetition time, so any additions to the total overhead reduce the allowable time for encoding, consequently imposing an additional limit on the highest achievable spatial resolution for acquisitions with constrained repetition times.

For this particular three-module implementation of the icones pulse sequence, some reduction in overhead time can be achieved by combining the pulses from the third module (containing the pulses for spoiling and secondary RF excitation) with those of the first module (containing the primary RF excitation pulses). This combination yields a two-module implementation. The spoiler pulses (and second set of excitation pulses) would simply need to be placed before the original set of excitation pulses in order for the two-module implementation to function properly. In the case when spoiling (second excitation) are not necessary, the corresponding waveforms will have zero amplitude and duration. This modification is completely feasible and reasonable to do, because all of the pulses that are used for the excitation and spoiling rely on the same scanner coordinate matrix. Consequently, the physics governing the pulse sequences would not be affected by the two-module implementation. Furthermore, the reduction in overhead time that a two-module implementation provides could be used to acquire images with slightly higher spatial resolution than is achievable by the three-module implementation.

Eventually, the additional overhead time required of a multiple module icones pulse sequence could be eliminated to allow for a one-module implementation. This would occur once the scanner systems have been updated to provide enough gradient waveform memory to accommodate the full set of rotated icones encoding gradient waveforms.

It is worthwhile to mention that the first implementation of the icones pulse sequence was designed as a single module containing all of the excitation, encoding, and spoiling pulses. Similar to the current implementation, this scheme also relies on modification of the scanner coordinate matrix with the icones rotation matrix during the system update time (i.e. $S \cdot R^{(j)}$), but in order to avoid an unwanted rotation of the excitation and spoiler pulses this particular one-module implementation also requires a rotation of the slice selection and spoiling gradients using values that are derived from the icones rotation matrix $R^{(j)}$. The main idea is that by rotating the slice selection and spoiling gradients in the direction directly “opposite” that of the modified scanner coordinate matrix, $S \cdot R^{(j)}$, these waveforms (and the icones encoding gradients) will be mapped to the correct physical axes after application of the modified scanner coordinate matrix. As previously mentioned, this approach would have allowed all RF and gradient pulses to reside in one module of system instructions, utilizing only one unit of system overhead time and therefore yielding the maximum length of time for spatial encoding in imaging settings that involve constrained TRs. Unfortunately, this technique is troubled by unavoidable numerical rounding errors that occur during manipulation of the scanner coordinate matrix which lead to unwanted oblique slice selection. Consequently, a valid single-module implementation would require further software development than feasible at this time.

3.2.4 Compatibility with multiple contrast mechanisms

The icones gradients are self-balanced, making the sequence amenable to fully refocused SSFP acquisitions, including alternating TR methods. The trajectory may also be utilized for RF spoiled gradient recalled echo (SPGR) acquisitions to obtain T1-w images. Examples of imaging the human brain with an SPGR implementation and imaging the human knee with an FS-ATR acquisition are provided in the results section of this chapter.

3.2.5 Image Reconstruction

Image reconstruction is performed through Fourier transform after gridding. Zwart’s method [43], which combines the iterative routine developed by Pipe [44] with an optimal kernel design formulated by Johnson [45], is utilized to determine density compensation weights since they cannot be calculated analytically. The density compensation algorithm accounts for trajectory crossings as well as the high density of samples near the origin and the outer edge of k-space. To correct unwanted phase accrual and trajectory deviations caused by eddy currents, we have adapted a calibration technique that was developed by Brodsky [19] for the 3D radial VIPR acquisition.

3.2.5.1 Iterative Density Compensation

By default, the iterative density compensation routine yields coefficients that minimize the root mean squared error (RMSE) of the final reconstructed image. This is a consequence of the fact that the iterative step for conditioning the estimated density coefficients involves convolution of the weighting function: $W_{i+1} = \frac{W_i}{W_i \otimes C}$. Since convolution is a local process, the conditioning of the weights is limited by the radius of the convolution kernel, which is roughly inversely proportional to the k-space sampling interval for which sampled points are uncorrelated (1/FOV). In regions where nearest neighbors are separated by distances exceeding the kernel radius (i.e. $1/FOV$), the estimated sample densities converge to some constant value. When applied to an undersampled 3D-PR trajectory, the iterative routine generates weights that increase from nearly zero (for highly dense samples near the origin) to a maximum value for data located where sampled points are first spaced at intervals greater than 1/FOV and remain constant up to k_{max}. These under-estimated coefficients significantly reduce the impact of the increased noise associated with the (undersampled) high spatial frequency data on the final reconstructed image. Utilizing these coefficients minimizes RMSE at the expense of reduced spatial resolution.

For the icones sampling pattern, we wish to reconstruct images that exhibit the full spatial resolution of the acquired data rather than minimizing RMSE. As previously mentioned, we utilize the iterative density compensation routine developed by Zwart [43] which by default yields coefficients that lead to images with minimal RMSE at the cost of reduced spatial resolution for undersampled trajectories. Fortunately, this iterative routine can be utilized to yield coefficients which preserve the native resolution of the raw data at the cost of increased noise. This is achieved by modifying the value of the ‘effective matrix size’ parameter that it is provided. Typically, the value for the effective matrix size is the desired matrix size of the final image and is inversely proportional to the field of view. Reducing the value of the effective matrix size increases the size of the convolution kernel that the iterative algorithm creates to process the data. When utilizing the routine to provide coefficients for a 3D icones trajectory characterized by an undersampling factor of US, we reduce the effective matrix size from N to $N/\sqrt{US}$ so that radius of the convolution kernel increases from $1/FOV$ to $\sqrt{US}/FOV$. With this modification, the convolution step will include at least two sample points for all data points along the trajectory. Consequently, the impact of sparsely sampled data points will not be underestimated and the native resolution of the raw data will be preserved when the final coefficients are utilized for image reconstruction.

3.2.5.2 Correcting Unwanted Phase Accrual & Trajectory Deviations

As each gradient sampling waveform in true radial imaging is the same trapezoidal shape, rotating the trajectory only still results in the same shaped waveform on each axis. Thus the sampling waveform needs to be calibrated only once for each physical axis. This is not true in icones, as the G_x and G_y gradient shapes are quite different. Therefore, we have first adapted the extended Duyn method to correct B0 phase and trajectory deviations for the component of each rotated gradient waveform that is due to the rotation of the dominant gradient waveform, G_x, onto each physical axis. We have chosen to do this because it is faster than measuring the eddy currents for each rotated gradient waveform, which would require one to measure thousands of trajectories.

The correction scheme follows the methodology described in section 1.4.1 of this document. We make two assumptions. The first is that the resultant k-space trajectory deviations created after the G_x and G_y icone waveforms are rotated and summed onto each physical axis are primarily due to eddy currents created by the dominant icone waveform, G_x. The second assumption is that the effects of the G_y gradient are negligible and thus the G_y gradient creates no k-space deviations. These assumptions rely on the observation that the intervals of high slew rate gradients are much higher on the G_x waveform than on G_y. If these assumptions are valid, then the Duyn method will likely produce the deviations that require correction, allowing us to avoid measuring eddy current corrections for each of thousands of rotated waveform sets.

For our adapted method, we measure only the G_x waveform on the three physical axes and utilize these data to synthesize the actual k-space trajectory for each rotated icone and to make point-by-point phase corrections for each actual trajectory. The synthesized k-space trajectory is calculated using the following equation:

$$\begin{aligned} k_x(j,p) &= R_{1,1}(j)\cdot\gamma\sum_{s=1}^{p}G_{B0;x}(s)\Delta t + R_{1,2}(j)\cdot\gamma\sum_{s=1}^{p}G_y(s)\Delta t \\ k_y(j,p) &= R_{2,1}(j)\cdot\gamma\sum_{s=1}^{p}G_{B0;y}(s)\Delta t + R_{2,2}(j)\cdot\gamma\sum_{s=1}^{p}G_y(s)\Delta t \\ k_z(j,p) &= R_{3,1}(j)\cdot\gamma\sum_{s=1}^{p}G_{B0;z}(s)\Delta t + R_{3,2}(j)\cdot\gamma\sum_{s=1}^{p}G_y(s)\Delta t \end{aligned} \qquad (28)$$

where $G_{B0;x}(s)$, $G_{B0;y}(s)$, $G_{B0;z}(s)$ are the measured gradient strengths of the G_x icones waveform along the x, y, and z axes, respectively, for sample *s*. Consistent with our assumptions, we utilize $G_y(s)$, the idealized icones G_y gradient amplitude at sample *s*, when synthesizing the corrected k-space trajectory.

The first column of each rotation matrix (employed for rotating G_x) determines the appropriate fraction of the measured B0 phase data to apply in the correction process. In particular, the *j*th icones rotation data are phase corrected using the following equation:

$$\Delta\Phi_{B0}(j,p) = R_{1,1}(j)\Psi_{B0;x}(p) + R_{2,1}(j)\Psi_{B0;y}(p) + R_{3,1}(j)\Psi_{B0;z}(p) \qquad (29)$$

where $R_{1,1}(j)$, $R_{2,1}(j)$, $R_{3,1}(j)$ are the values from rows 1, 2, and 3 of the first column of the *j*th icones rotation matrix, respectively, and $\Psi_{B0;x}(p)$, $\Psi_{B0;x}(p)$, $\Psi_{B0;x}(p)$ are the measured phase accrual when the G_x icones waveform is generated on the physical x, y, and z axes, respectively, for sample p.

Problems with this method might occur when the G_y gradient becomes more prominent, which occurs for wider iCone petals. These gradients will likely require a more sophisticated correction method, such as a generalization of the technique used by Moussavi for 2D radial [16] combined with the linear system impulse response method developed by Addy [46].

3.3 Results

In the results that follow, we demonstrate the feasibility of the icones trajectory. We demonstrate pulse sequence software which utilizes iCone gradients in SPGR, SSFP, and ATR acquisitions. The measurements for the modified Duyn Method are performed as a quick calibration scan after imaging. We also demonstrate software reconstructions used to reconstruct images from the raw MR icones data. Routines for B0 and linear eddy current corrections and for utilizing the iterative density compensation routine developed by Zwart[43] are also implemented in this reconstruction software. For completeness, we provide images of the impulse response for one set of icones parameters to demonstrate the improved spatial resolution achievements from our adaptation of the iterative density compensation.

3.3.1 Examples of icones sampling patterns

Listed in **Table 2** are the readout times, average speed along trajectory, and number of readouts for several icones trajectories of increased petal width and the corresponding 3D-PR trajectory for the same degree of undersampling, field of view and matrix size. The potential advantages of the icones trajectory become evident as the petal width increases (i.e. larger θ). For wider petals, the average speed along the trajectory increases (**Figure 28**), so that even though the readout time increases, the increased coverage per readout means that fewer readouts are needed. These results indicate that the icones trajectory has the potential to acquire images with the same level of undersampling as the 3D-PR trajectory but in fewer excitations and thus less scan time.

Table 2: Readout Times, Angular Separation of Spokes, and Average Speeds along Out-and-back Trajectories of 3D-PR and 3D icones, with 18 cm FOV, 360 Matrix Size, and 3.9252x Undersampling. As the skip factor increases and the angular width of the icone petal increases, the average speed of the k-space trajectory increases and thus fewer excitations are needed.

Trajectory	Skip	Angular Width of Base Petal, θ (°)	Avg. Angle between spokes(°)	Readout Time (us)	Avg. Speed (mm^{-1}/ms)	No. Readouts
3D-PR	N/A	N/A	0.63	2,044	0.98	51,863
Icones	0	1.26	0.62	1,768	1.14	50,728
Icones	2	6.62	3.30	1,824	1.14	46,119
Icones	4	12.51	6.35	1,856	1.15	41,544
Icones	6	19.07	9.59	1,880	1.18	36,944
Icones	8	26.34	13.51	1,904	1.22	32,532

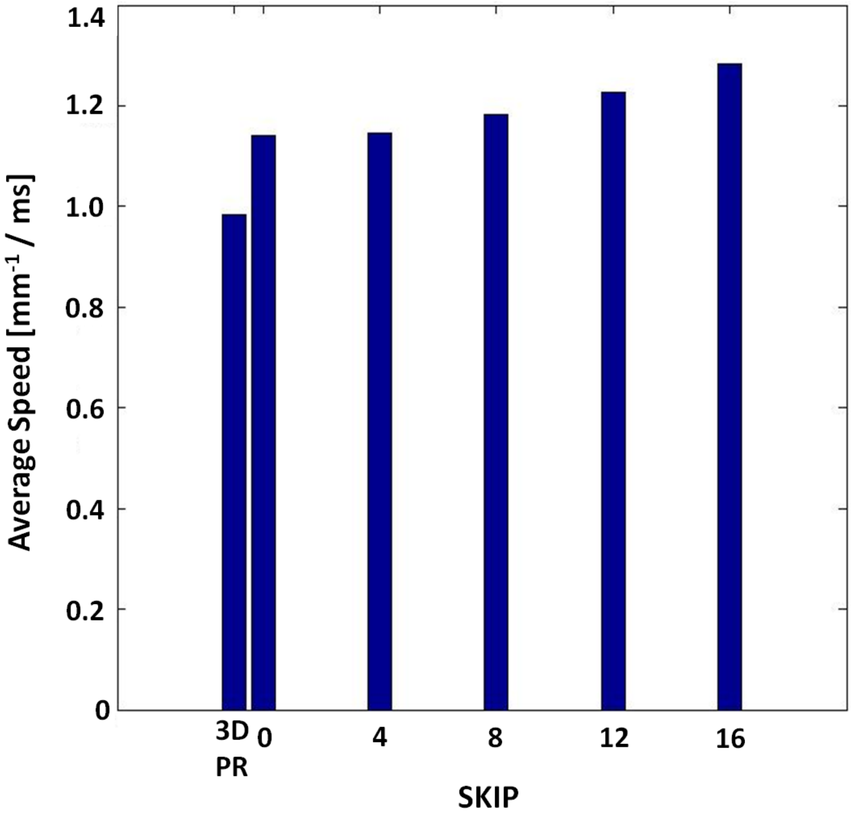

Figure 28: Average speeds along the 3D-PR and icones trajectories using several values of ‘skip’. The benefits of a curved trajectory are quite apparent: as ‘skip’ increases, the average speed along the trajectory increases.

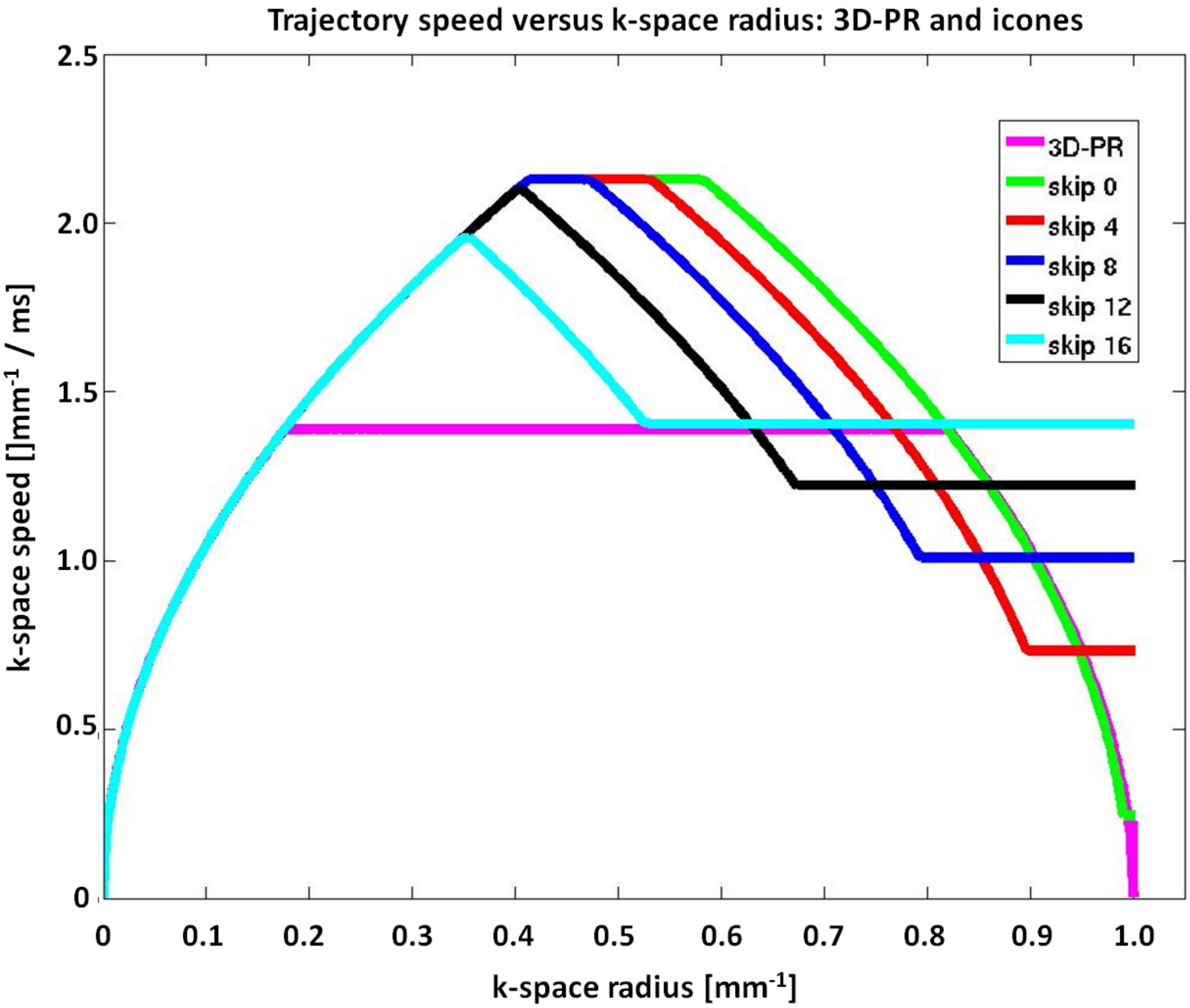

Figure 29: A comparison of the instantaneous speeds along the outbound portions of the 3D-PR trajectory and several icones trajectories of increasing skip value (i.e. petal width). The speed along each icones petal is higher than that of the out-and-back, 3D-PR trajectory at the outer edge of k-space, where the 3D-PR trajectory momentarily stops. All trajectories are designed to achieve 0.5mm isotropic resolution within an 18cm FOV using the same maximum slew rates, maximum gradient amplitudes, and sampling rate.

Instead of utilizing the increasingly higher trajectory speeds of icones to reduce the scan time for a given level of undersampling when compared to 3D-PR, it possible to maintain the scan time while reducing the level of undersampling. An example of this is provided in **Table 3**, which lists the gradient readout times, average trajectory speeds, and total number of readouts for a single 3D-PR trajectory and several icones trajectories. Just as before, all trajectories are designed to acquire images with an 18cm field of view and matrix size of 360^3. The 3D-PR trajectory, which serves as the baseline for this example, acquires images with an undersampling factor of 3.9252 using 51,863 readouts. The icones trajectory which most closely approximates this particular 3D-PR trajectory has an undersampling factor of 3.9252 and skip value of 0 (second row of Table 3). This particular icones trajectory acquires 50,728 readouts, slightly fewer than 3D-PR.

Just as before, we generate additional icones trajectories by modifying a few design parameters. First, we increase the value of skip, which in turn increases petal width and, therefore, gradient readout time. For a fixed level of undersampling, this would reduce the total number of readouts. Instead, we decrease the prescribed undersampling factor, which then keeps the total number of readouts at a value near 50,728. We perform this task several times, with the value of skip increasing by two from 0 to 22, resulting in undersampling factors that range between 3.9252 and 1.9911, respectively. The resulting trajectories are listed in **Table 3** and an illustration which shows that increasing the skip factor allows for reductions in undersampling is displayed in Figure 30. These results suggest that the icones trajectory has the potential to acquire images with lower levels of undersampling than the 3D-PR trajectory while using approximately the same number of readouts (i.e. approximately same scan time).

Table 3: The high degree of trajectory crossings and petal overlapping at the outer edge of k-space allows increased petal width and a simultaneous reduction in undersampling factor for the icones trajectory. Imaging parameters are 18 cm FOV and 360 image matrix size.

Trajectory	Under-sampling Factor	Skip	Base Petal Angle (°)	Avg. Angle between spokes (°)	k_{spoke} (m^{-1})	Readout Time (us)	Avg Speed (mm^{-1}/ ms)	No. Readouts
3D-PR	3.9252	N/A	N/A	0.63	1,000	2,044	0.98	51,863
icones	3.9252	0	1.26	0.62	989	1,768	1.14	50,728
icones	3.5989	2	6.04	2.99	947	1,816	1.13	50,728
icones	3.3305	4	10.44	5.28	911	1,848	1.14	50,728
icones	3.1006	6	14.52	7.28	879	1,864	1.15	50,729
icones	2.8994	8	18.30	9.30	850	1,880	1.16	50,728
icones	2.7247	10	21.84	11.02	824	1,888	1.17	50,729
icones	2.5658	12	25.11	12.84	800	1,904	1.18	50,778
icones	2.4324	14	28.24	14.51	779	1,912	1.19	50,788
icones	2.3008	16	31.14	16.25	757	1,928	1.19	50,703
icones	2.1895	18	33.87	17.77	739	1,936	1.20	50,777
icones	2.0919	20	36.52	19.38	722	1,944	1.21	50,729
icones	1.9911	22	38.94	20.66	704	1,952	1.21	50,673

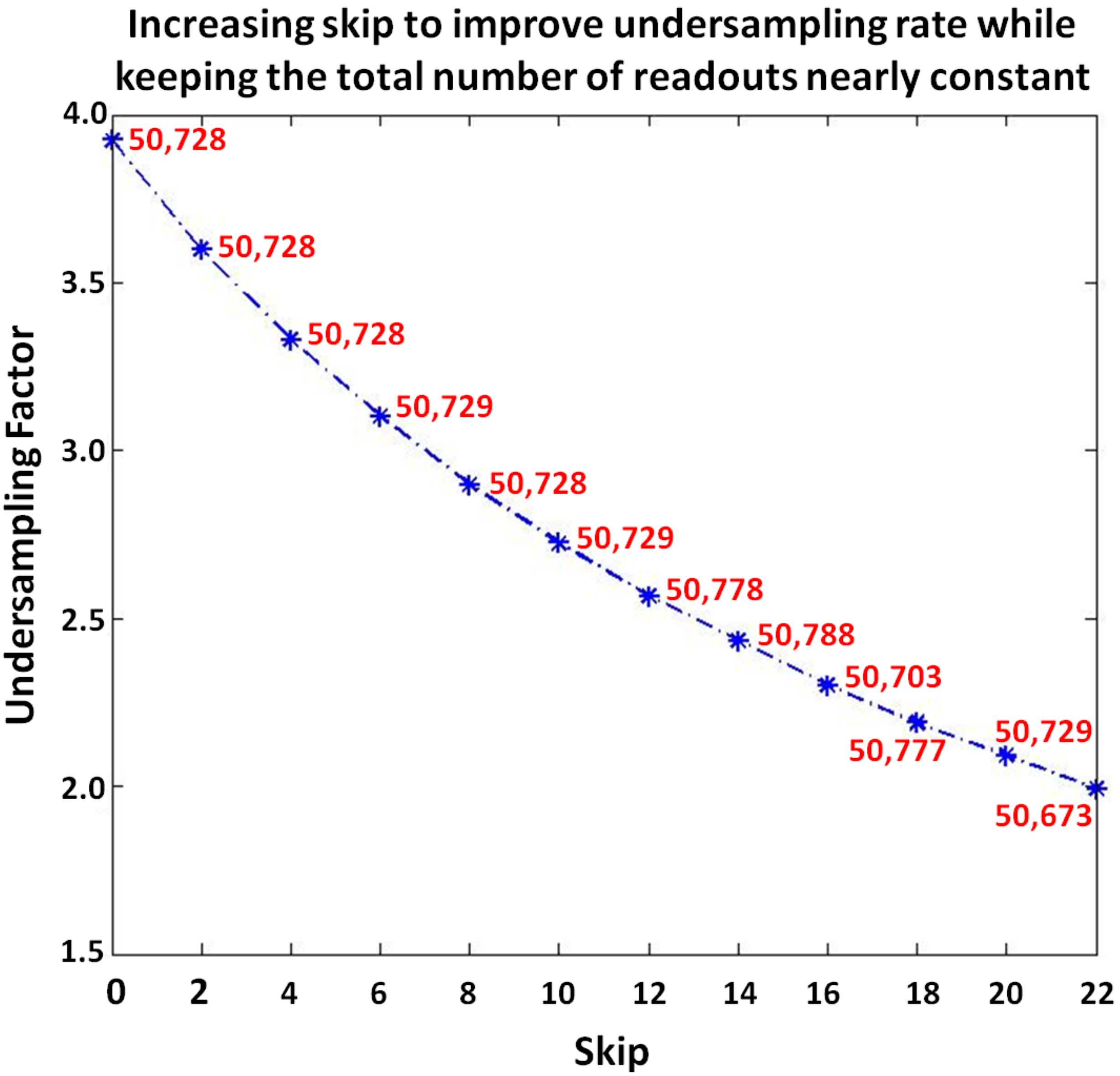

Figure 30: An ensemble of icones trajectories in which the skip factor is increased while the undersampling factor is reduced in order to keep the total number of readouts relatively constant. The red integer label next to each data point represents the total number of readouts for that particular icones trajectory.

3.3.2 Impulse Response

A good assessment of any sampling pattern is its ability to accurately image a point object, commonly referred to as the impulse response or point spread function. Trajectories and related reconstructions with narrow impulse response profiles that focus energy near the imaged test impulse will suffer from less blur and image artifact due to aliasing.

In this section, we present images of the impulse response and corresponding Fourier Space images of the gridded impulse data for two designs of the icones sampling pattern and the two corresponding 3D-PR trajectories. For two trajectories we measure the percentage of energy that is contained within the central 25% of the image pixels in order to capture the effects of the central and first lobes of the point spread function associated with each sampling pattern.

Icones Impulse Response for a Narrow Petal Design

The parameters of the first icones trajectory design and corresponding 3D k-space trajectory ensemble that we first examine are listed in the first two rows of **Table 3** and are repeated here: undersampling factor = 3.9252; FOV = 18cm; Image Matrix = 360; skip = 0 yielding θ_{base_petal} = 1.26° (θ_{avg}=0.62°); Number of excitations = 50,728; Readout time = 1.768 ms. The parameters for the corresponding 3D-PR trajectory are: undersampling factor = 3.9; FOV = 18cm; Image Matrix = 360; Average angle between spokes θ_{avg}=0.63°; Number of excitations = 51,863; Readout time = 2.044 ms. These two trajectories are compared because they should achieve the same spatial resolutions and similar levels of undersampling artifact with approximately the same number of readouts. Note that the icones and 3D-PR sampling patterns typically do not utilize exact the same number of readouts due to differences in the design algorithms of these trajectories.

The central axial, coronal, and sagittal images of the impulse response generated by these two trajectories are presented in Figure 31. These two sets of images are quite similar, as expected, since the two sampling patterns bear comparable characteristics, such as average angle between spokes, number of readouts, and readout time. Both impulse responses exhibit an alias-free region that is approximately equal to ½ FOV, which is expected for radial trajectories with undersampling factors of approximately 4. The regions that exhibit aliasing are characterized by patterns that are reminiscent of each trajectory: radial streaks for the radial, 3D-PR trajectory and overlapping spirals for the icones trajectory. One other notable difference between the two sets of images is the increased brightness of the cylindrical boundary separating the alias-free region from the rest of the images for the icones trajectory. In the axial view this boundary appears as a bright ring residing at approximately ½ FOV, and as two bright lines in the coronal and sagittal views.

For both trajectories, 89% of the total image energy is contained within the central sphere of 40-pixel diameter, where the total image energy of the impulse response is defined as the cumulative signal measured inside the central sphere with a 360-pixel diameter.

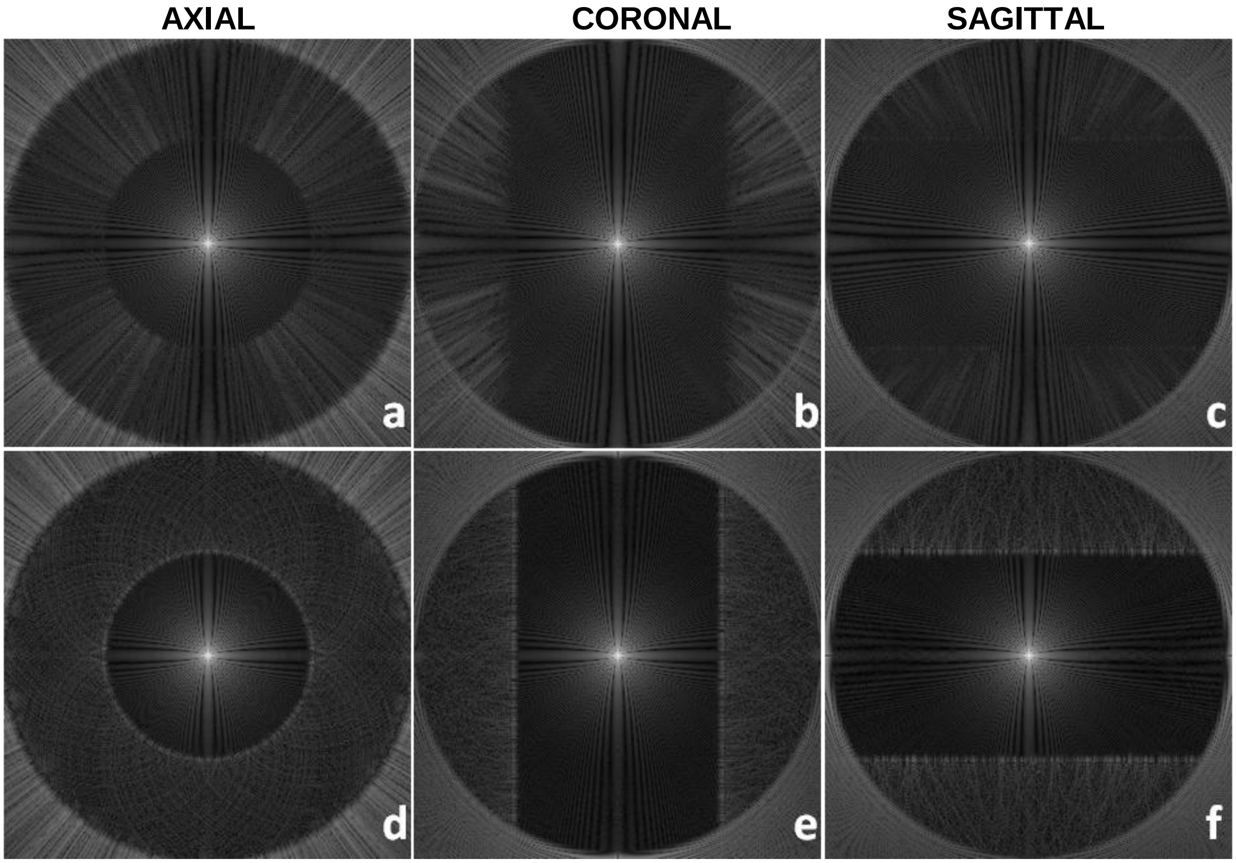

Figure 31: (a) Axial, (b) Coronal and (c) Sagittal central slices of the impulse responses produced by the out-and-back 3D-PR trajectory and icones trajectory (d-f) with equivalent imaging parameters (listed in first two rows of Table 3). The two sampling patterns yield similar results, with the possible exception of the bright ring residing at ~½FOV in the (d) axial view of the icones trajectory. For each sampling pattern, 89% of the image energy is captured within the central sphere of 40 pixels (25% of the image matrix), indicating similar levels of aliasing and therefore comparable image quality would be expected with the two trajectories.

Figure 32 contains the Fourier Space representations of the sampling patterns whose impulse responses are presented in Figure 31. These images provide a visual representation of the impulse data after interpolation onto a Cartesian grid but just before Fourier inversion. The axial views depict several out-and-back paths for the icones and 3D-PR sampling patterns, revealing that the basic 2D icones base petal and the 2D out-and-back PR trajectories are reasonably mapped into 3D k-space. These Fourier Space representations of the impulse data are very similar for this particular pair of icones and 3D-PR trajectories. One notable exception is the dark sliver of unsampled frequencies appearing in the coronal and sagittal slices of the icones images. An additional, minor difference is that for the icones trajectory the gridded data at the edge of k-space (i.e. $k = k_{max}$) appears to oscillate more in intensity (Figure 32 e,f) when compared to the corresponding surface of the 3D-PR trajectory.

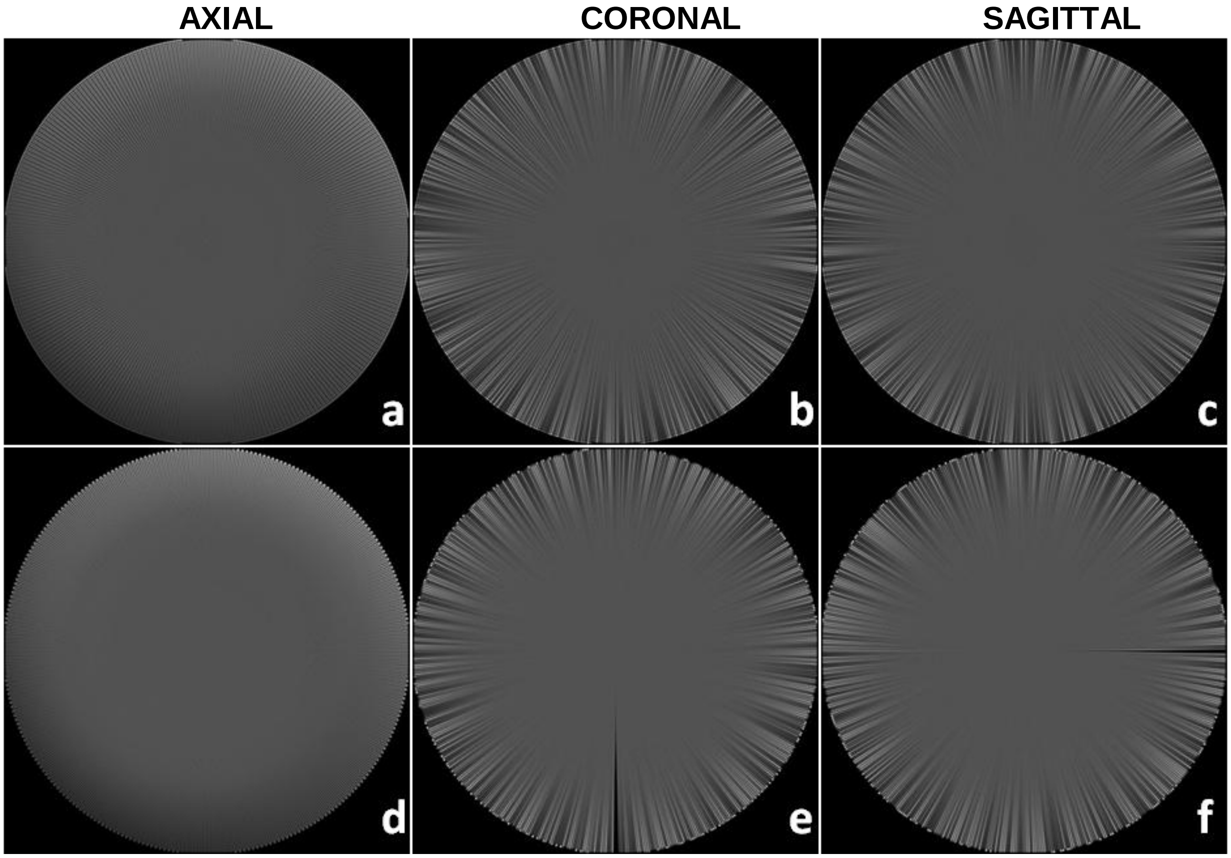

Figure 32: Central slices sampling representation (Fourier Space) after density compensation before they are transformed to yield images of the impulse response for the out-and-back, 3D-PR (a,b,c) and icones (d,e,f) trajectories made with equivalent imaging parameters (first two rows of Table 3). The corresponding axial, coronal, and sagittal images presented above are quite similar, with the exception of a dark sector of missing energy appearing in the coronal and sagittal views of the icones trajectory.

Icones Impulse Response for a Wider Petal Design

We investigate a second pair of impulse responses generated by the icones and 3D-PR trajectories. In this scenario, an icones trajectory (row 6 of **Table 2**) is designed to achieve 0.5mm isotropic resolution with an undersampling factor of 3.9, an 18cm FOV, and 360^3 image matrix size. These are the same values as in the previous setting. However, unlike in the previous example, the icones petals are interleaved so that several petals overlap in the outer edges of k-space (Figure 15d). In this case, the skip parameter is set to 8, and as a result of Equation (10) the petal width has increased, θ_{base_petal}. Additionally, the readout time per petal is increased to 1.904 ms. However, the total number of readouts decreases to 32,532, which is a reduction of 35% compared to the icones design in which petals do not overlap at all (i.e. skip = 0).

The imaging parameters of the 3D-PR trajectory remain the same as before, except that the number of readouts is reduced to 32,550 in order to closely match the number of readouts utilized with the icones sampling pattern. The parameters for 3D-PR are repeated here for comparison purposes: undersampling factor of 3.9; 18 cm FOV; 360^3 image matrix; an average angle of 0.80° between adjacent radial spokes; readout time of 2.044 ms.

The impulse responses of these two trajectories are examined and compared here, because even though they should achieve the same spatial resolutions in roughly the same number of readouts, the icones trajectory is designed to achieve a lower level of undersampling.

Images of the impulse response generated by each of these trajectories are presented in **Figure 33**. A side-by-side comparison of the three orthogonal views reveals that the two sampling patterns do not yield comparable results. The 3D-PR trajectory, which is designed with a higher undersampling factor than the icones trajectory, yields a spherical FOV that is clearly visible in all three orthogonal planes; whereas, the icones trajectory yields what appears to be a spherical FOV that is obscured by aliased energy, with the most prominent aliasing occurring in the axial view. Concentric rings of energy emanate from the center of the images corresponding to the impulse response of the icones trajectory. The impulse response of the 3D-PR trajectory does not exhibit the concentric rings of energy like the icones trajectory, but there is some energy dispersal from the center of the image out toward the edge of the spherical FOV.

The Fourier Space representations of the point spread functions from Figure 33 are shown in Figure 34. Again, these images provide a visual representation of the k-space sampling pattern after interpolation onto a Cartesian k-space grid and density compensation. Just as before, the axial views depict several out-and-back paths for the icones and 3D-PR sampling patterns, revealing that the basic 2D icones base petal and the 2D out-and-back PR trajectories are reasonably mapped into 3D k-space.

The out-and-back paths of the 3D-PR and icones trajectories appear to be evenly spaced about the k_z axis (**Figure 34** a,d), which corresponds to the center pixel of the axial images. Additionally, the intensity of the sampling patterns varies from a dark shade (bottom right quadrant) to maximum brightness (top and center) and returns to a dark shade (bottom left quadrant), indicative of the fact that the trajectories follow a spiral from the –kz pole to the +kz pole.

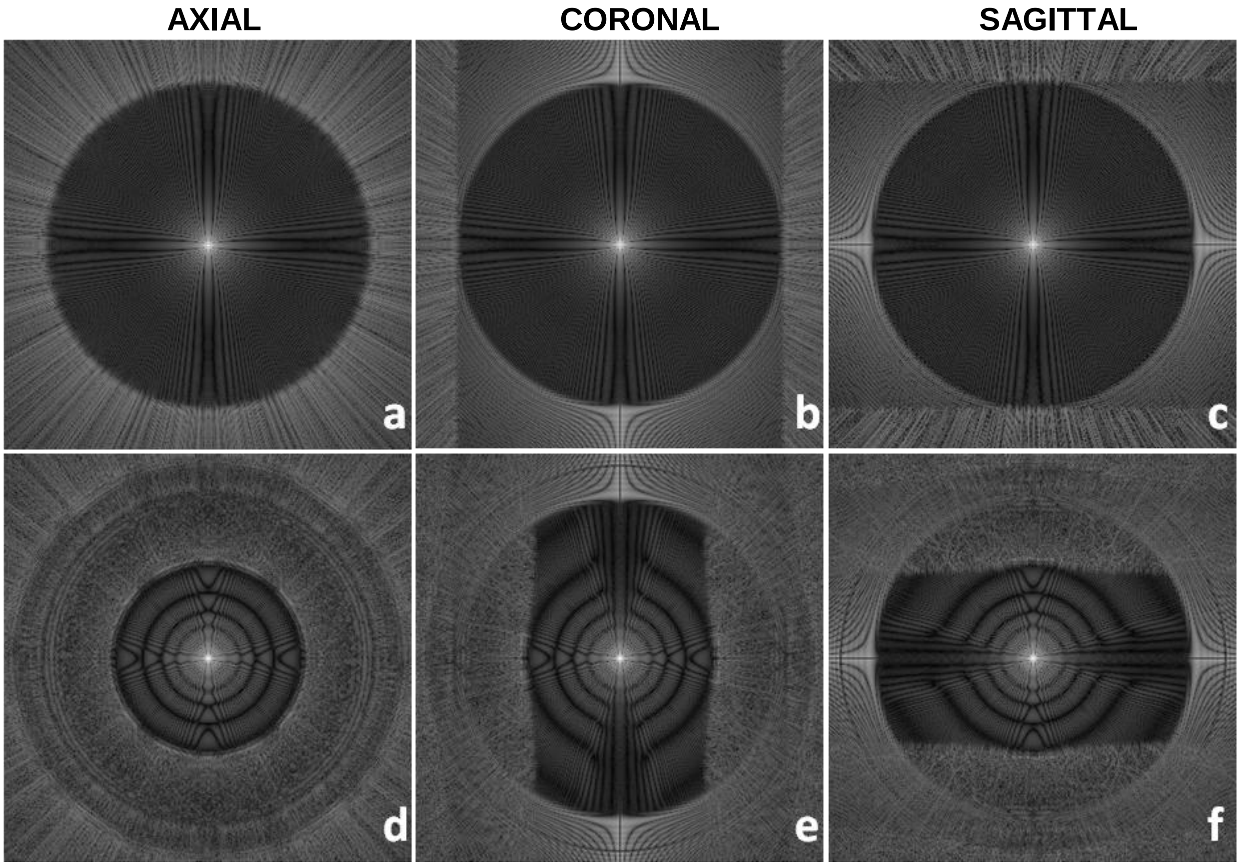

Figure 33: Central (a) axial, (b) coronal, and (c) sagittal slices of the impulse responses produced by the out-and-back 3D-PR trajectory and icones trajectory (d,e,f) with 18cm FOV and 360 pixel image matrix size. The 3D-PR trajectory is designed for 32,550 readouts (i.e., undersampling = 6.25) and the icones trajectory with 32,532 readouts and an undersampling factor of 3.93. Unlike the situation presented in Figure 31, the two sampling patterns do not yield comparable results. In fact, the 3D-PR trajectory yields a clearly visible spherical FOV, whereas the icones trajectory yields what appears to be a spherical FOV obscured by aliased energy in the three orthogonal planes.

The coronal (XZ) and sagittal (YZ) views of the 3D-PR sampling pattern (Figure 34 b,c) bear resemblance to each other. In these views, the radial lines appear to be evenly spaced, but the variation in their intensities is much more dramatic than that of the axial (XY) view (**Figure 34** a), and is also a consequence of the trajectory spiraling about the k_z axis from the –kz pole to the +kz pole.

The coronal and sagittal views of the icones sampling pattern (**Figure 34** e,f) appear similar to each other, as was the case with 3D-PR. The intensity of the radial spokes also varies in both of these views, which again is an effect of the trajectory spiraling around the k_z axis.

A significant feature of the icones trajectory is that it exhibits many unsampled spatial frequencies which appear as dark “holes” in the outer region of k-space between k_{spoke} and k_{max} (**Figure 34** d-f). These “holes” are largest at k_{spoke}, where the sampling density is minimal, and decrease in size at the edge of k-space where more petals overlap (Figure 34a).

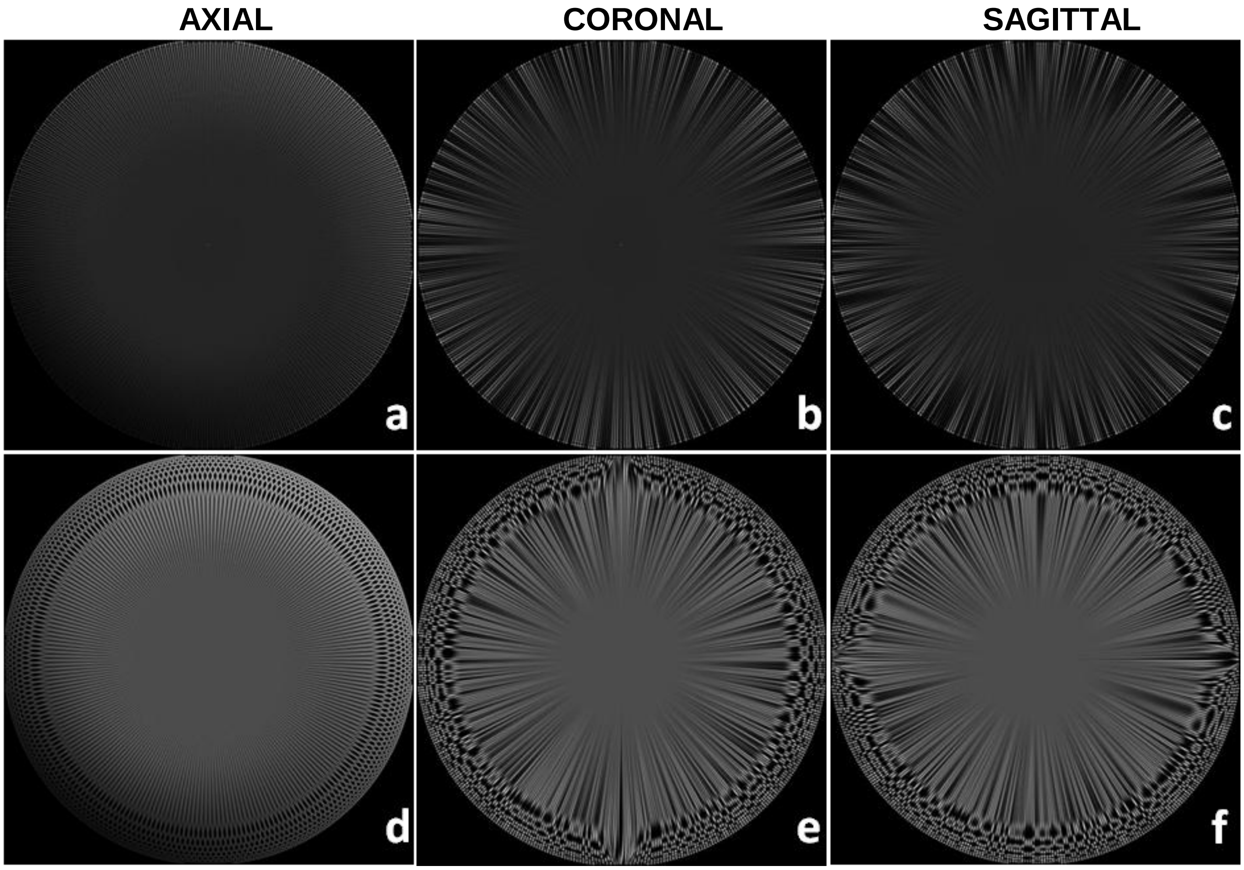

Figure 34: Central slices of the k-space sampling trajectory after gridding and density compensation for the out-and-back, 3D-PR trajectory (a,b,c) and an icones (d,e,f) trajectory, each with approximately 32,500 readouts. In all three planes the icones trajectory exhibits many unsampled spatial frequencies appearing as dark “holes” in the outer region of k-space where the trajectory turns. There are also many dark slivers that reside along the radial direction for both trajectories.

3.3.3 The Adapted Iterative Density Compensation Routine

To demonstrate the effectiveness of our adaptation of the iterative density compensation routine, we provide images of the knee () that were reconstructed from the same raw 3D Radial-ATR data but with three different sets of pre-gridding density compensation coefficients. The coefficients were generated using (a) an r-squared analytical function, (b) Zwart’s iterative routine optimized for minimal root-mean-squared-error, and (c) Zwart’s iterative method revised for high spatial resolution. The images that were reconstructed with the r-squared (gradient amplitude weighted) analytical density compensation function (a) and with the iterative routine optimized for minimal RMSE (b) both exhibit a reduction in noise at the cost of reduced spatial resolution, as expected. On the other hand, the image acquired using our previously described adaptation of the iterative density compensation routine (c) exhibit higher spatial resolution with improved depiction of the tibial and femoral cartilage surfaces and reduced blur of the synovial fluid but with increased noise across the entire image. With this simple experiment, we demonstrate that our approach for density compensation is satisfactory and will be particularly useful for utilization with the icones trajectory.

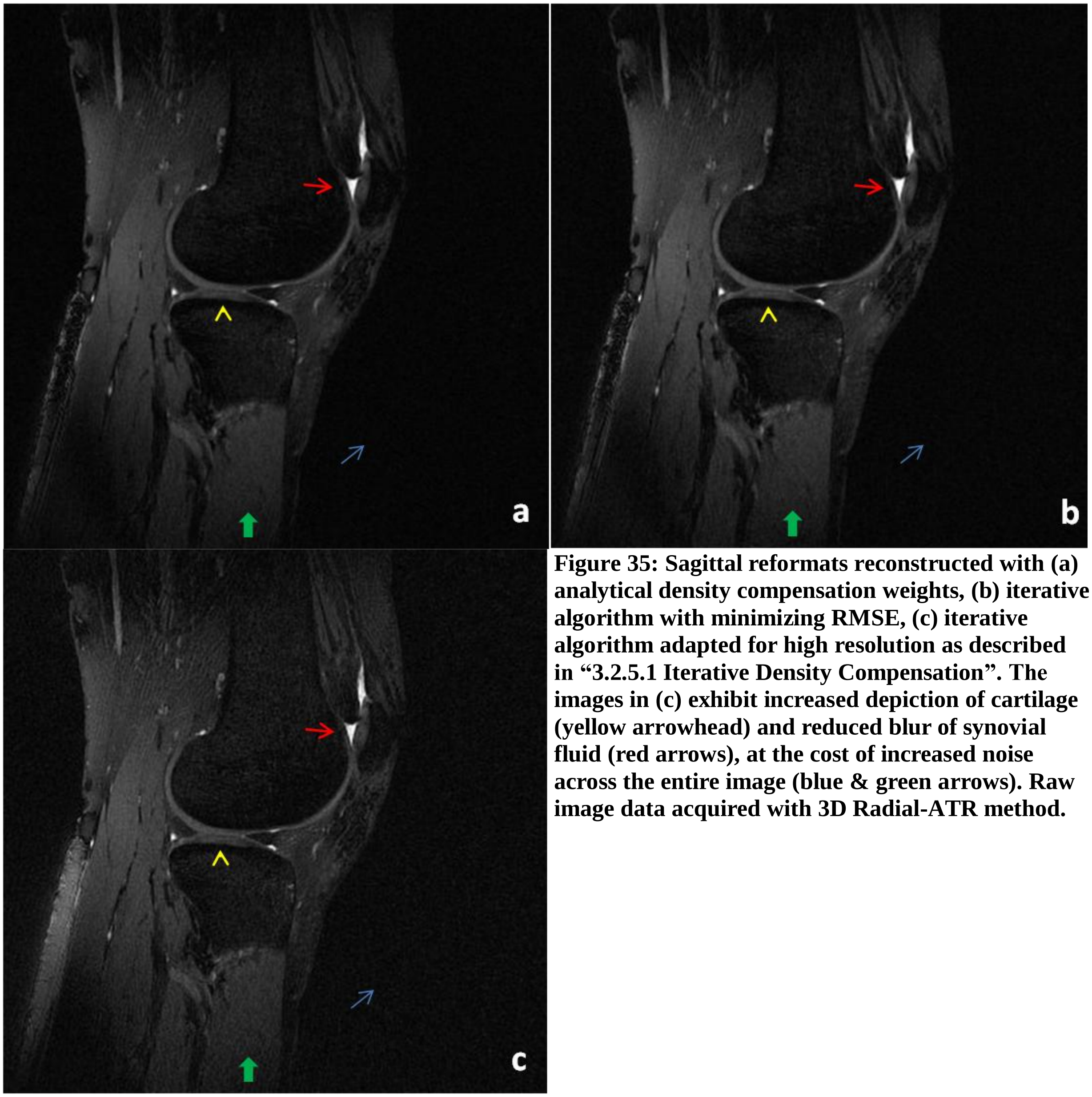

Figure 35: Sagittal reformats reconstructed with (a) analytical density compensation weights, (b) iterative algorithm with minimizing RMSE, (c) iterative algorithm adapted for high resolution as described in "3.2.5.1 Iterative Density Compensation". The images in (c) exhibit increased depiction of cartilage (yellow arrowhead) and reduced blur of synovial fluid (red arrows), at the cost of increased noise across the entire image (blue & green arrows). Raw image data acquired with 3D Radial-ATR method.

3.3.4 The Calibration Method in a Water Phantom

An icones-SPGR acquisition with an undersampling factor of 3 and skip of 0 was employed to demonstrate the effectiveness of the adapted Duyn method for the icones trajectory. In accordance with the method described in section **3.2.5.2 Correcting Unwanted Phase Accrual & Trajectory Deviations**, measurements were made by testing the icones G_x gradient (Figure 36) on all three physical axes using a single channel head coil (GE Healthcare Waukesha, WI) on a 3.0T MR750 GE Healthcare system (GE Healthcare Waukesha, WI).

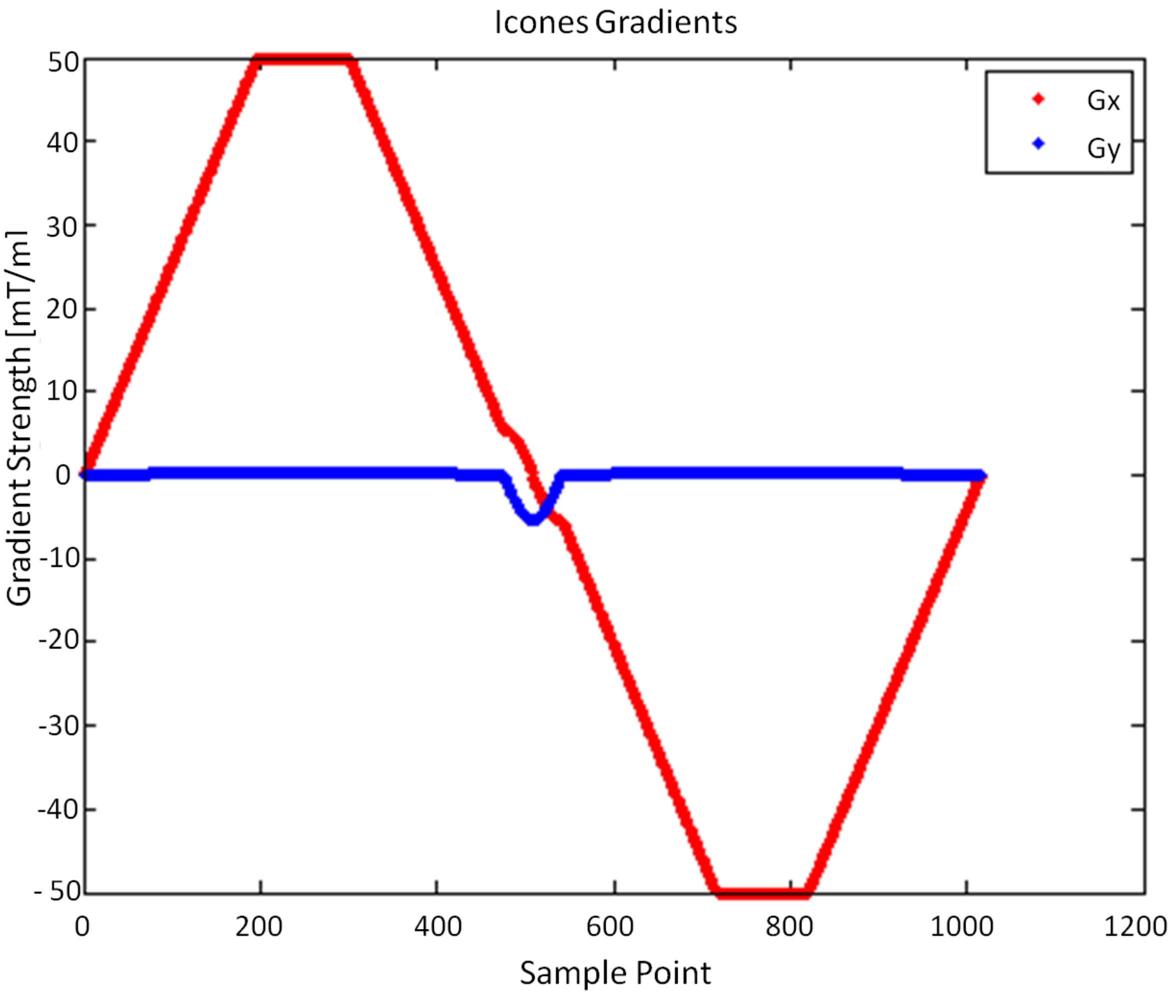

Figure 36: The Gx icone gradient displayed above was utilized as the test gradient in an adapted version of Duyn's method for correcting eddy current induced k-space trajectory deviations and phase errors. This pair of icones gradients was designed to achieve an undersampling factor of 3, skip =0, 15cm FOV, maximum gradient amplitude of 50mT/m, maximum slew rate of 128mT/m/ms, and ±125kHz bandwidth.

The point-by-point k-space deviations and phase errors due to eddy currents arising from the G_x icone gradient are displayed in Figure 37. The average trajectory deviations along all three physical axes (**Table 4**) reside within 0.60 of a step-size in k-space, with the largest deviations occurring along the Z axis. While correcting the k-space trajectory to account for these deviations improves image quality, the most significant improvements arise from correcting the phase errors observed in Figure 37b & c, which exhibit total variations of 90° and 179° along the x- and y-axes, respectively. Since phase errors exceeding 55° typically lead to noticeable degradations in image quality, correcting the phase accrual observed in Figure 37b & c leads to significant improvements in image quality (Figure 38). These phase reduced the blurring manifested in the high frequency "comb-like" structure (green arrows) and along the rounded edges of the phantom (yellow and red arrows). Additionally, the phase correction technique removed the blur and apparent signal loss occurring within the central regions of large structures (blue ovals). These results validate the utility of our method for correcting phase errors.

Table 4: k-space deviations along each physical axis.

Axis	Avg $\lvert\Delta k\rvert$ $[m^{-1}]^*$	Max $\lvert\Delta k\rvert$ $[m^{-1}]$	Total Variation† $[m^{-1}]$
X	0.419	0.988	1.687
Y	0.275	0.800	1.245
Z	0.579	1.311	2.105

*$\Delta k = k_{meas} - k_{ideal}$

†Total Variation = max(Δk) – min(Δk)

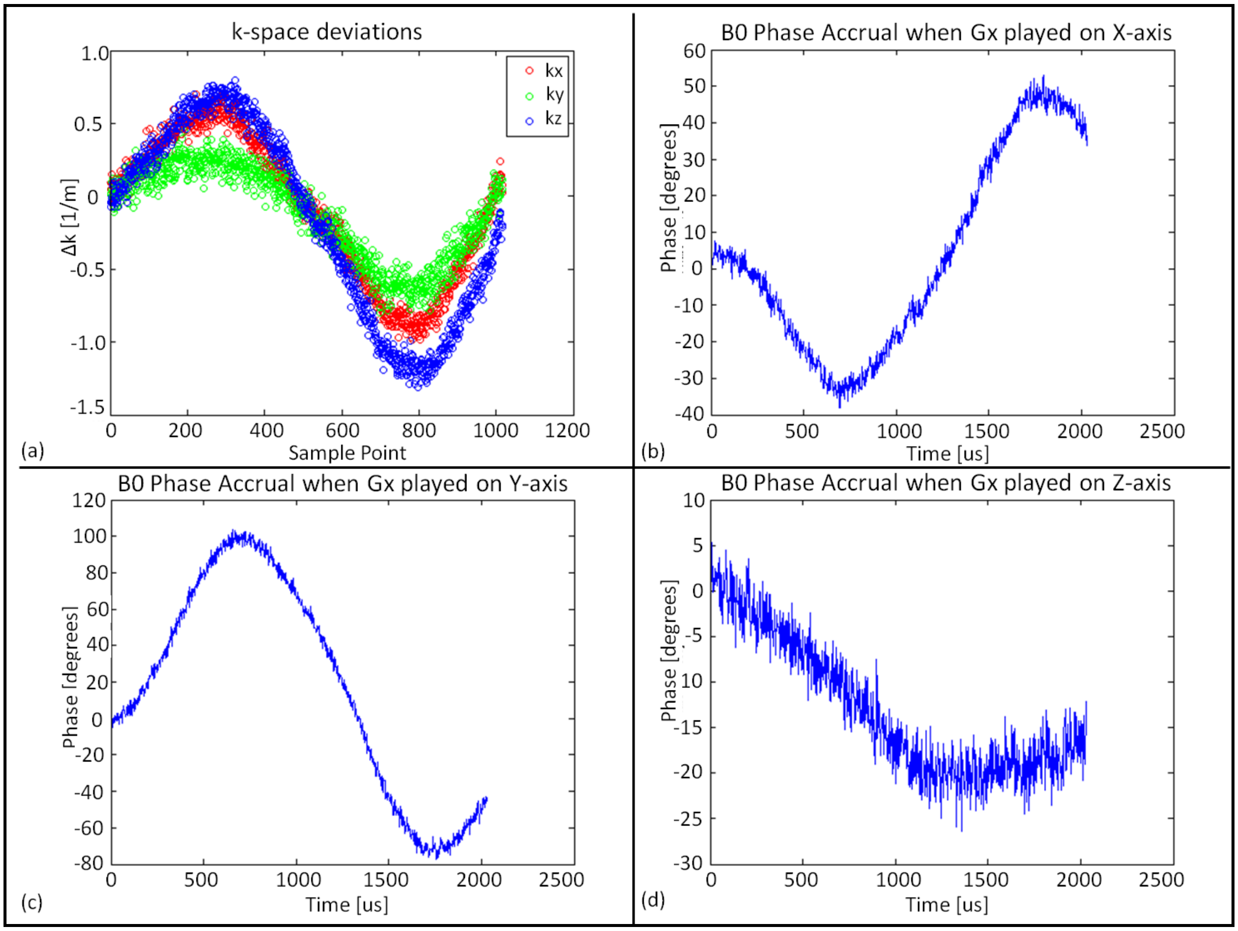

Figure 37: Calibration data acquired with Duyn's method, utilizing the Gx icone gradient on all three physical axes. The (a) k-space deviations due to eddy currents when the Gx gradient is tested on the physical x, y, and z axes. The accrued phase error due to B0 eddy currents is significant when the Gx icone gradient is generated on the physical (b) x and (c) y axes, since the total variation in phase exceeds 55°. Generating the Gx icone gradient on the physical (d) z axis does not introduce significant phase error.

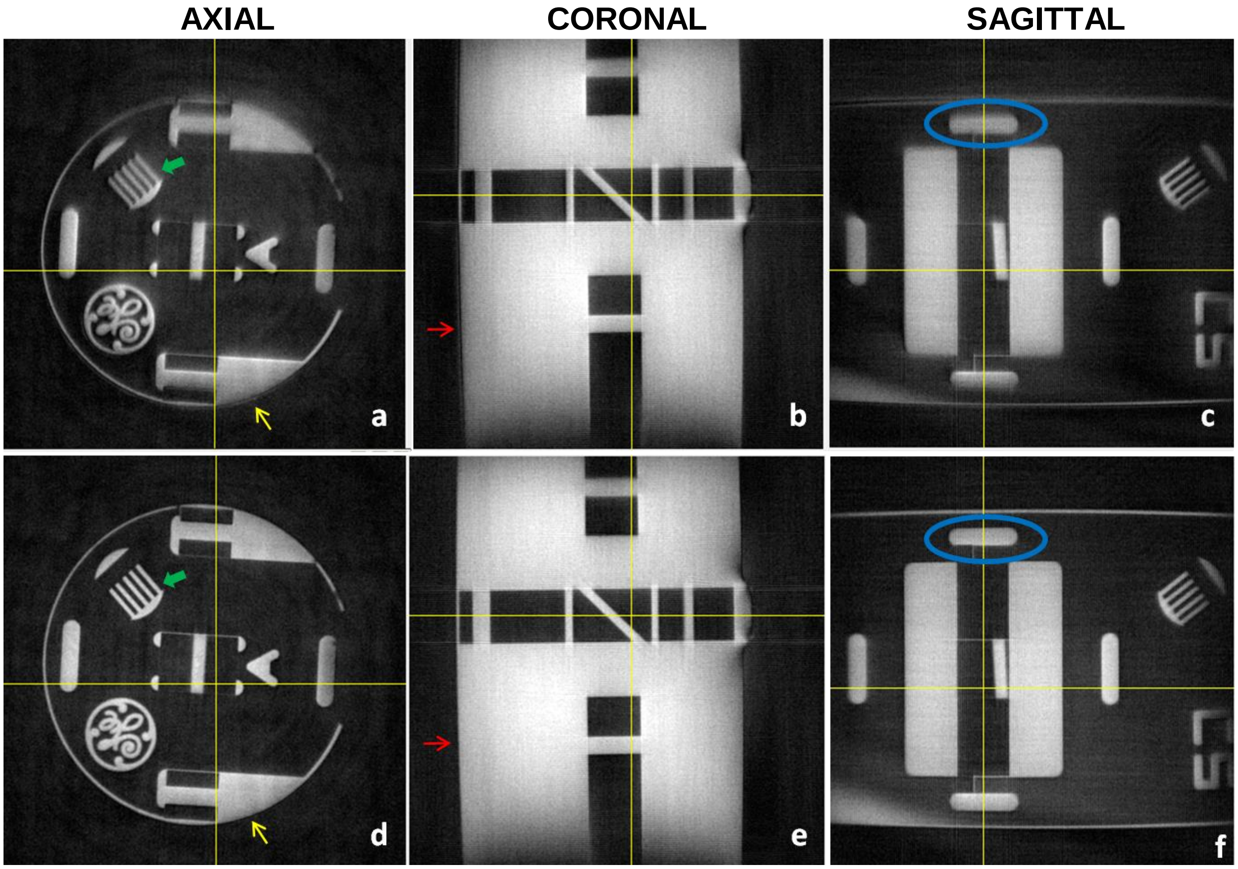

Figure 38: (a) Axial, (b) Coronal, and (c) Sagittal images of a GE Resolution Phantom acquired with an icones-SPGR method (skip=0) prior to application of B0 phase corrections. This technique eliminates the blurring (d, e, f) of high frequency structures (thick green arrow), particularly along the edges (yellow and red arrows) of the phantom, and (f) low spatial frequency content (blue ovals) as well.

3.3.5 T2-like Acquisition of the Human Knee

We have combined three version of the dual, half-echo icones trajectory with the fat-suppressed ATR method (TR = 4.6 ms) to produce 0.5mm isotropic resolution images. All images were acquired with an 18 cm FOV, 360^3 image matrix, BW=±125 kHz; 15° flip angle, G_{max}=50mT/m, and S_{max}=128 T/m/s. The three icones sampling patterns that we tested were the following:

(1) 3.9x undersampling factor; skip=0; $\theta = 1.26°$; 50,728 readouts; 3.75 mins

(2) 3.9x undersampling factor; skip=8; θ = 26.34°; 32,532 readouts; 2.5 mins

(3) 2.9x undersampling factor; skip=8; θ = 18.30°; 50,728 readouts; 3.75 mins

Images were also acquired using the out-and-back, 3D-Radial ATR method with 51,863 readouts and the same gradient system and imaging parameters that were used for the icones-ATR method. Imaging was performed on a healthy volunteer using a 3.0T Discovery MR750 and 8-channel extremity coil.

Icones-ATR and 3D Radial-ATR provide bright fluid, intermediate cartilage signal, and reasonable fat suppression (Figure 39). The images also demonstrate excellent fluid-cartilage and bone-cartilage contrast. Excellent depiction of cartilage is observed in the three orthogonal planes, with clear separation of the femoral and tibial cartilage surfaces, for 3D Radial-ATR (Figure 39b) and the two icones-ATR acquisitions (Figure 39e&h) that utilize 50,728 readouts. These two icones-ATR methods—one with 3.9x undersampling factor and skip=0, and the other with 2.9x undersampling factor and skip of 8 –demonstrated the best depiction of cartilage (Figure 39d,e,j,k), outperforming 3D Radial-ATR possibly due the increased sampling density of high frequencies by these icones trajectories. The image quality between these two trajectories is comparable even though they were designed for two undersampling factors (2.9 versus 3.9) that have the potential to demonstrate noticeable differences in undersampling artifact. The images acquired with the 3.9x undersampled, skip=8 icones design (Figure 39g-i) had the worst image quality, with substantial blurring of the cartilage and synovial fluid. In some places, the blur was so prominent that the cartilage was hardly visible.

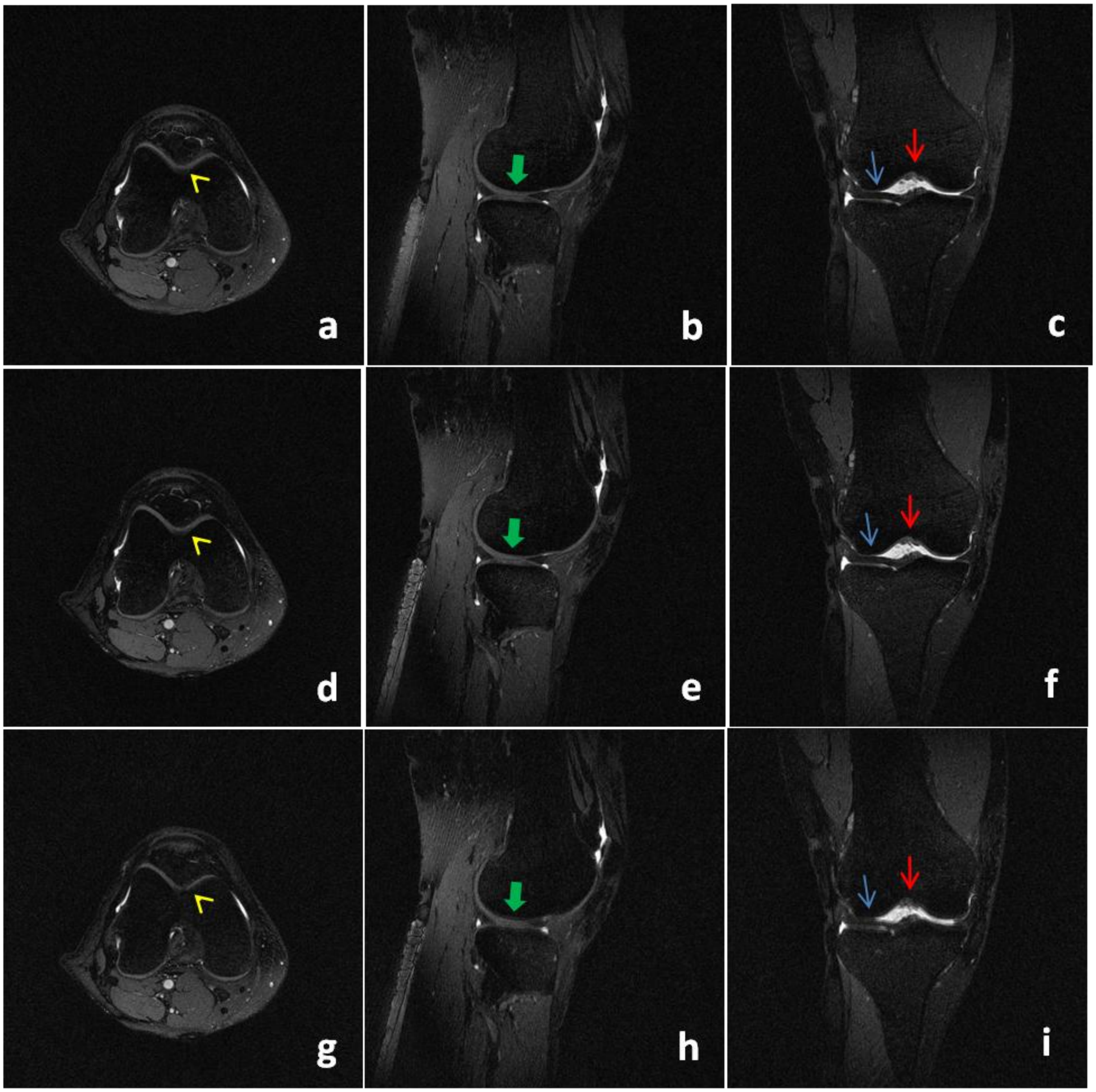
a
b
c
d
e
f
g
h
i

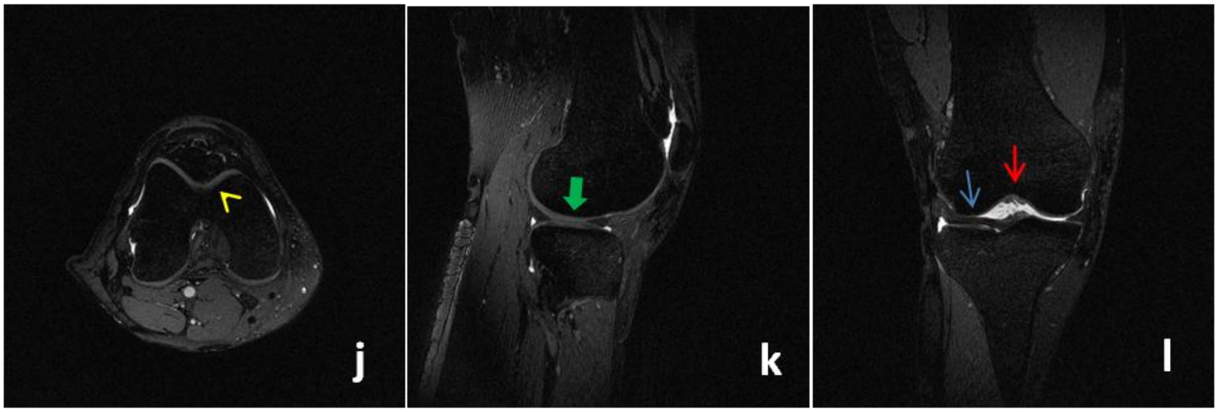

Figure 39: Images of the human knee acquired with four different trajectories using the ATR fat suppression method. (a) Axial, (b) sagittal, and (c) coronal views acquired with the out-and-back, 3D Radial-ATR (3.9x undersampling) yield excellent depiction of the articular surfaces of the cartilage and excellent cartilage-fluid contrast in 4 mins. The (d,e,f) icones-ATR method with 3.9x undersampling and skip =0 yields the best image quality in 4mins, including improved depiction of cartilage (d, yellow arrow) compared to 3D-Radial. The icones-ATR method with 3.9x undersampling and skip = 8 (2.5 mins) exhibits so much blur (g-i; yellow, green, red arrows) that the cartilage is hardly visible in some views (i, blue arrow). The icones-ATR method with 2.9x undersampling and skip = 8 yields images in 3.75 mins with some blurring of the cartilage surface (j; yellow arrow).

3.3.6 T1-w Acquistion of the Human Brain

The icones trajectory was utilized as an SPGR acquisition to obtain 0.69 mm isotropic resolution images in 4.75 minutes (TR= 3.8 ms) with: FOV = 22cm; 320 isotropic image matrix; axial scan plane; 76,861 excitations; undersampling factor of 1.15; skip=14; θ_{iCone}=13.4°; BW =±125 kHz; flip=5°; G_{max}=50 mT/m; S_{max}=128 T/m/s. Imaging was performed on a healthy volunteer using a 3.0T Discovery MR750 and 8-channel birdcage coil. For comparison, images were also acquired with the 3D-PR trajectory as an SPGR acquisition with similar imaging parameters. The 3D-PR utilized 76,800 excitations, nearly the same number used for the icones acquisition, leading to an undersampling factor of 2.65.

Axial and sagittal reformatted images (Figure 40) demonstrate feasibility of the icones-SPGR method. Images acquired with the out-and-back, 3D-PR demonstrate clear delineation of the edges of the skull and of the various folds of the brain (Figure 40a,b). The icones trajectory, however, suffers from blur and a “haze” of aliased energy across the entire image that. Consequently, some edges of the skull and various folds of the brain tissue are either difficult to see or are absent. The grey, noise-like “haze” is prominent in the nasal cavity (Figure 40d); in comparison, the nasal cavity of the image acquired with 3D-PR appears dark.

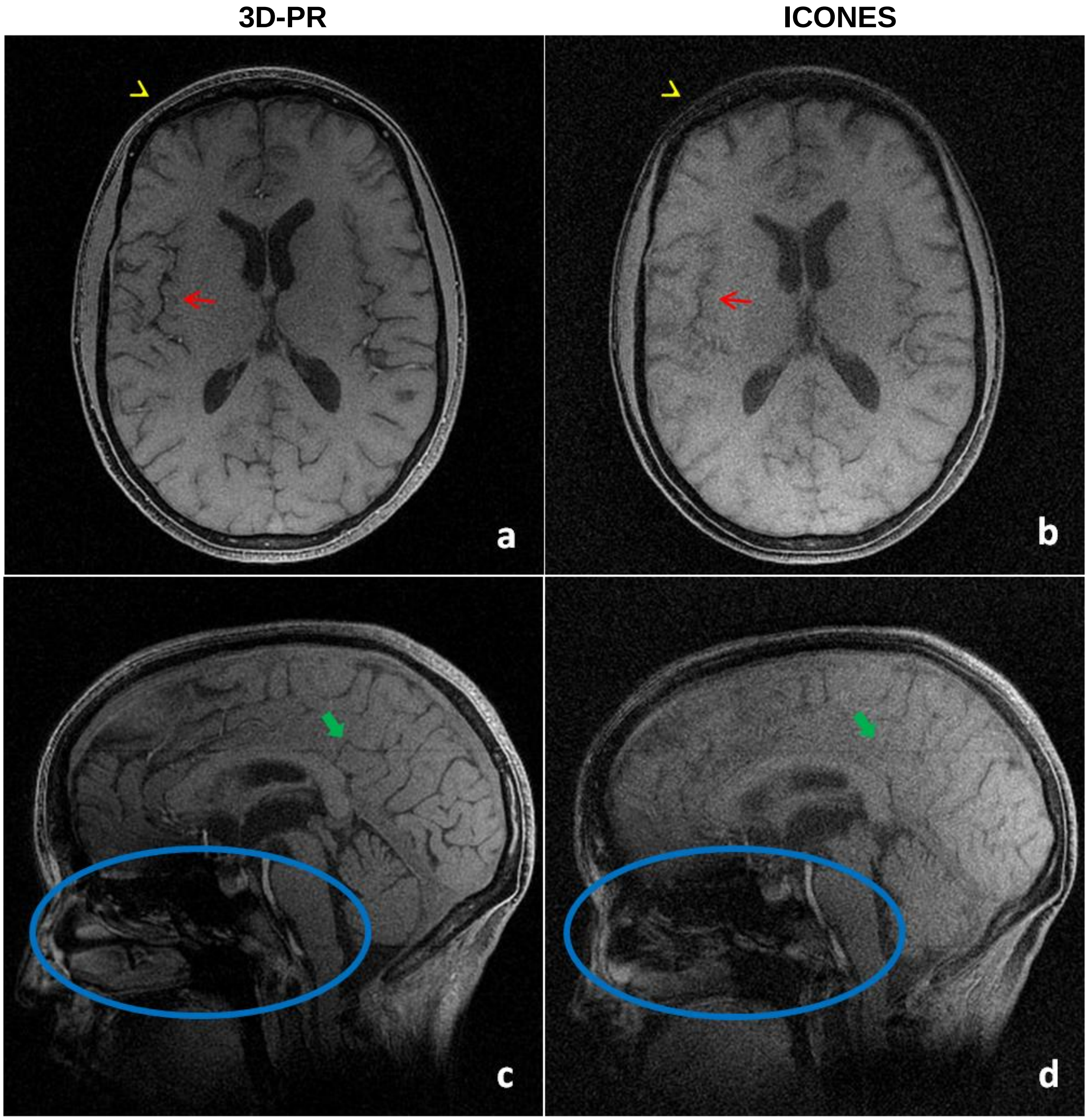

Figure 40: Axial images acquired with (a) 3D-PR SPGR and (b) icones-SPGR methods. Sagittal reformats (c,d) are created using the same acquisition data. The icones trajectory (skip =14) suffers from blurred edges (yellow arrowhead, red arrow, green thick arrow) and aliased energy (blue oval), as expected due to the wide central lobe of the impulse response similar to Figure 33.

3.4 Discussion

Our first two developments of icones have been for the brain and the knee. We have chosen these anatomical regions because they can be imaged at isocenter with a reasonable field of view, 18cm for the knee and 22cm for brain, thereby minimizing off-axis acquisition complications. Additionally, they provide opportunity to employ the sequence with different contrast mechanisms, T2-w for knee and T1-w for brain. These two anatomical regions serve as good testing grounds for two future applications of the icones trajectory: ATR imaging of the hip joint, and bilateral T1-w breast imaging, both of which require large FOVs (and associated off-axis effects).

We have demonstrated feasibility of the 3D icones rosette-like trajectory and obtained high quality, high isotropic resolution images of the knee and brain at 3.0T. Preliminary success in the brain and knee indicates that the trajectory might be applied successfully to T2-like ATR acquisitions of the hip joint and T1-w acquisitions of the breast, barring further refinements to the icones algorithm. While we demonstrate feasibility, we have not yet conducted comparisons with the VIPR trajectory.

3.4.1 Examples of icones trajectories

Two ensembles of icones trajectories were presented in Table 2 and Table 3, with each depicting a separate advantage to using this sampling method. With the ensemble presented in Table 2, the results indicate that by allowing the icones petals to widen and also overlap at the outer edges of k-space, the sampling density at the outer edges of k-space increases in a way that could permit reductions in the total number of readouts for a given level of undersampling. This is possibly due to the fact that longer curved portions of the trajectory allow for higher average speeds that compensate for increases in readout length. The results of **Table 3** indicate that the icones petal width can be increased to reduce levels of undersampling while holding the total number of readouts approximately constant. While these two advantages of the trajectory are significant and could be useful in clinical applications of the knee, the impulse response and *in vivo* images of the knee and brain presented in this work indicate that the algorithm for generating the icones trajectory needs additional refinements in order to achieve these distinct advantages. At this point in time, the icones trajectory holds *potential*.

3.4.2 Icones Impulse Response for a Narrow Petal Design

The icones and 3D-PR trajectories of Figure 31 and Figure 32 achieve similar-looking images of the impulse response in all three orthogonal planes. This is not surprising since both trajectories are designed with nearly comparable image acquisition parameters (Table 2), and the icones sampling patterns with skip=0 should resemble the 3D-PR trajectory.

The increased intensity of the cylindrical boundary in the point spread function for the icones trajectory of Figure 31 may be due to the fact that the icones sampling pattern samples half the number of frequencies at the outermost edge of k-space that the 3D-PR samples, thereby leaving larger “holes” of unsampled image energy. This new structure of “holes” resides on a sphere at the spatial frequency corresponding to k_{max}.

For the icones trajectories with skip=0 and the corresponding 3D-PR trajectory, 89% of the total image energy is contained within the central sphere of 40-pixel diameter, where the total image energy of the impulse response is defined as the cumulative signal measured inside the central sphere with a 360 pixel diameter. These comparable energy measurements indicate that the two trajectories would be expected to achieve similar image quality when utilized for an *in vivo* application and was verified with images of the knee (Figure 39a-f), showing promise for the icones trajectory.

3.4.3 Icones Impulse Response for a Wider Petal Design

The fact that the 3D-PR trajectory yields an impulse response with a clearly visible spherical FOV in all three orthogonal planes (Figure 33), despite its higher undersampling factor, and that the icones trajectory yields the hint of a spherical field of view that is plagued by aliased energy, indicates a problem with the design of the icones trajectory. This complication with the trajectory is also manifested in Figure 34d-f, in which the gridded k-space data corresponding to the icones trajectory is characterized by dark “holes” of unsampled spatial frequencies in the outer regions of k-space between k_{spoke} and k_{max}.

It has already been mentioned in this work that as the amount of petal overlap increases (as specified by an increased ‘skip’ parameter), more holes appear at the edge of k-space between k_{spoke} and k_{max} (Figure 34d), with holes of the same size residing at the same radial distance from the center. It is possible that the collection of “holes” residing at a particular radial distance in 3D k-space exhibits enough periodic structure to produce an aliasing pattern in the impulse response. When all holes at all radii are considered together, their collective structure might produce the high degree of aliased energy that both obscures the spherical FOV and also forms concentric “rings” about the center pixels in Figure 33 d-f. This aliasing artifact and the presence of holes is a problem that is strongly manifested by icones trajectories with overlapping petals (i.e. nonzero skip values), as these issues are not observed in the 3D-PR trajectory. The “ring” of aliased energy present in Figure 31d may be a slight manifestation of this issue for the icones trajectories that do not cross over themselves (i.e. skip = 0). Additional work is needed to address this problem.

3.4.4 Adaptation of Iterative Density Algorithm

We presented three images of the knee that were acquired with the 3D Radial-ATR method. All images were reconstructed with the same raw MR data and utilized the same reconstruction process with the only exception being a different set of pre-gridding density compensation weights for each image. The images reconstructed with the analytical density compensation function and the iterative routine optimized for minimal RMSE exhibited a smoothening of noise at the cost of spatial resolution, which led to image blurring. The image reconstructed using our adapted version of the iterative routine exhibited the highest spatial resolution at the cost of increased noise, as expected from our analysis. The results of this experiment indicate that this approach for generating density compensation weights for the icones trajectory is justified. Furthermore, where applicable, comparisons of the 3D-PR trajectory and the various icones ensembles in this work are made using images that were reconstructed with density compensation weights produced by this adapted iterative routine.

3.4.5 Calibration Method

The results presented in Figure 38 demonstrate the effectiveness of our proposed method for correcting k-space trajectory deviations and phase accrual due to linear and B0 eddy currents, which we assume are primarily generated by the G_x icone gradient. The phase error corrections yielded substantial improvements to the images for both low and high spatial frequencies. The phase accrual was largest when the test gradient was generated on the y-axis, with accumulations of 100° for some samples, and measurements along the x-axis revealed substantial phase accruals of 50°. In our correction method, we assumed that a predictable combination of these phase accruals are present during each readout, because the two base icones gradients are rotated onto each physical axis during imaging. The improved depiction of the edges and of the comb-like structure of the phantom (Figure 38) suggests the assumptions of our phase correction method are reasonable for the gradients under examination.

While images that demonstrate the improvements attributed purely to k-space trajectory deviations were not presented in this work, those improvements are implied by the fact that the final images incorporating the trajectory corrections and phase corrections exhibit fairly good image quality (Figure 38).

3.4.6 T2-like Images of the Knee

The icones-ATR method is capable of generating high isotropic 0.5mm resolution images (Figure 39) with bright fluid, intermediate cartilage signal, and reasonable fat suppression in four minutes. All methods also demonstrate excellent fluid-cartilage and bone-cartilage contrast. Excellent depiction of cartilage (Figure 39 d-f, j-l) is observed in the three orthogonal planes for the two icones trajectories that acquired 50,728 readouts (2.9x undersampling factor, skip =8 and 3.9x undersampling factor, skip=0) and for the 3D Radial-ATR method (Figure 39 a-c) which acquired 51, 863 readouts.

Depiction of the cartilage surfaces was comparable for these two icones trajectories and better than that of Radial-ATR, possibly due to the increased sampling of high spatial frequencies by the icones trajectories. The icones trajectory with 3.9x undersampling and skip=8 performed worst for cartilage conspicuity. Some of the cartilage surfaces in these images were obscured by a high degree of blur, which was expected from the high degree of aliasing artifact present in the impulse response (**Figure 33**d-f).

It is somewhat surprising that the image quality produced by the trajectory designed for an undersampling factor of 2.9 and skip=8 was comparable to the icones trajectory designed for a 3.9x undersampling factor and skip=0. While not revealed in this document, the impulse response of the 2.9x undersampled trajectory exhibits hazing and rings of energy about the central pixel with much less severity than what is displayed in **Figure 33**d-f.

Given that the image quality of the 3.9x undersampled, skip=8 trajectory was much worse (i.e. substantial blur) than the other methods presented here, but in agreement with the point spread function of **Figure 33**d-f, we seek an explanation for why the image quality of the 2.9x, skip=8 trajectory was comparable to that of the 3.9x, skip=0 trajectory when their corresponding impulse responses would predict otherwise. Perhaps for these two icones trajectories, which have the same number of readouts and comparable readout times, the image quality in these acquisitions of the knee **Figure 39**is similar as a result of the relative differences in the distributions of sampled spatial frequencies between the trajectories. Consider the fact that the spacing between the spokes for the 2.9x undersampled, skip=8 trajectory is 0.54°; whereas, the spacing between spokes of the 3.9x undersampled, skip =0 trajectory is 0.63°. Consequently, perhaps the distribution of spatial frequencies that are sampled by the 2.9x undersampled trajectory, with its more tightly spaced spokes (and hence higher density of low frequencies) and much greater density of high frequencies (reduced high frequency noise), allow this version of icones to perform as well as the 3.9x undersampled, skip=0 version in the knee despite the qualitative differences in impulse response between the two trajectories.

3.4.7 T1-w Images of the Brain

In this experiment the icones trajectory was designed with a lower undersampling factor (1.15x) than the 3D-PR trajectory (2.65x), and the petals of the trajectory were allowed to overlap (skip=14). Since it was already known at the time of the experiment that the impulse response for this specific icones trajectory design exhibits a fair amount of aliased energy and has a wide central lobe, we did not expect the icones trajectory to outperform or even fare comparably to the 3D-PR method, which has a narrow impulse response. The substantial blurring of the skull and several folds of the brain in Figure 40b&d confirm our expectations.

The images of the brain are provided to merely demonstrate that the icones sequence can be employed as an SPGR acquisition. After the problem in the design of the icones trajectory has been determined and corrected, the sequence can be tested again to observe reductions in blur and to compare image quality with 3D-PR.

3.4.8 Limitations of icones

The images of the point spread function (Figure 31, Figure 33), the human knee (Figure 39g-l), and the human brain (Figure 40d-f) demonstrate that the 3D icones trajectory requires further refinements in order to outperform the 3D-PR trajectory. In addition, there are three other limitations to this sampling pattern which are mentioned below:

1. The gradients and rotation matrices are generated external to the G.E. scanner, are specific to each set of imaging and hardware parameters, and require that the executable file be compiled and downloaded to the scanner whenever a change in any of these parameters is desired. This is a relatively modest limitation as software could be developed to perform the waveform generation on the scanner itself.

2. Phase accrual and trajectory deviations due to eddy currents may become more complicated as the role of G_y increases. Unlike the VIPR sequence which employs linear combinations of three trapezoidal pulses to yield a 3D radial trajectory, icones utilizes rotation matrices to transform two distinct waveforms into three imaging gradients. At smaller values of the ‘skip’ parameter, the G_y gradient will have small peak amplitudes and low slew rates. In these cases, the trajectory errors will be primarily determined by the G_x gradient. The penalty for ignoring trajectory errors due to G_y will likely be minimal. As the ‘skip’ parameter increases, the role of G_y increases and trajectory errors due to the interaction of the G_x and G_y gradients as they combine on

each physical axis will grow. A novel and efficient correction scheme may be needed for wider petals.

3. Density compensation requires a several-hours iterative routine for each set of imaging parameters. Fortunately, the result only needs to be calculated once and can be re-used.

3.4.9 Potential Advantages of icones

Once the icones algorithm has been optimized, the icones trajectory could provide the following advantages over the 3D-PR trajectory:

1. Up to 30% reduced undersampling artifact compared to out-and-back, 3D radial for a given scan time.
2. Alternatively, reduced scan time for a given undersampling factor compared to out-and-back, 3D-PR.
3. Amenable to multi-echo acquisitions, particularly the ATR and IDEAL water/fat separation methods.

The ability to utilize the trajectory with the multi-echo ATR water/fat separation method has been demonstrated in the human knee (Figure 39 d-l). We have shown that the first two potential advantages have not been fully realized and that the icones algorithm requires further refinements. As soon as the icones algorithm is revised to achieve the desired improvements over 3D-PR, then *in vivo* studies of the human knee, hip, and bilateral breast with healthy volunteers can be performed to compare these two trajectories.

Chapter 4 Summary and Future Work

This chapter provides an overview of my contributions to and possible future directions of the work presented here.

4.1 Summary of contributions

The body of work presented here is comprised of two main projects: (1) a preliminary study of the efficacy of the 3D Radial-ATR sequence for detecting cartilage lesions and other abnormalities of the human hip joint during contrast enhanced MR arthrography, and (2) the development of a novel, 3D, rosette-like sampling pattern, termed icones, that was invented to improve upon the inefficiencies of the 3D Radial out-and-back trajectory.

Efficacy of 3D Radial-ATR for MR Arthrography of the Hip Joint

I executed the clinical evaluation of a volumetric, steady-state, T2-like sequence for isotropic evaluation of the entire hip joint using contrast-enhanced MR arthrography. The sequence featured a capability for inherent suppression of the bright fat signal present in steady-state sequences. I was responsible for all aspects of the imaging, including scanner calibration, data transfer, image reconstruction, and quantitative image analysis.

3D Icones Trajectory

The primary emphasis of this work is the development and implementation of the 3D icones sampling pattern. The original algorithm that generates the icones trajectory base gradient waveforms, and extension to 3D was created by our collaborator, Pablo Irrarazaval. I successfully reduced the icones concept to practice, which previous to my contribution was only simulated in 2D imaging. I made contributions in altering the process to rotate the 2D icone to fill the 3D space that substantially improved the impulse point spread function. For the specific settings mentioned in Section 3.3.1: ***Icones Impulse Response for a Narrow Petal Design***, the energy contained within the first 25% of the FOV increased from 57% of the nominal value to 89%, matching the 3D-PR trajectory.

I also developed a memory efficient implementation of the icones trajectory on several GE Healthcare scanner systems, including the MR 750, MR 750w, and HDxt Signa Excite scanner systems. This implementation, based on continually updating the scanner system coordinate matrix with an appropriate icones rotation matrix, avoids the need for considerable waveform memory, which the scanner systems lack, and the additional time required for the system to access this type of waveform memory, which would have imposed additional limitations on the maximum achievable spatial resolution for the ATR method. As previously mentioned, the sequence was implemented as three distinct modules: (1) excitation pulses, (2) imaging gradients, and (3) a choice between (a) spoiling pulses for SPGR acquisitions or (b) second set of excitation pulses for the ATR method. To improve efficiency in the future, one possible solution would be a two-module implementation with the same functionality of the three-module implementation. This method would merge the excitation and rewinder/spoiler components. I also successfully developed a calibration scan as an adapted version of Duyn’s method for correcting phase accrual errors and k-space trajectory deviations caused by B0 and linear eddy currents, respectively. The method demonstrated that only the dominant gradient in the icones scheme needs to be compensated, essentially making the method feasible by making the calibration time possible in seconds rather than tens of minutes.

4.2 Future Work

3D Radial-ATR for MR Arthrography of the Hip Joint

For the MR arthrography study comparing 3D Radial-ATR with conventional clinical MR sequences with 20 patients who underwent surgical arthroscopy, specificities and sensitivities for detecting cartilage lesions were calculated for the 3D Radial-ATR sequence and the conventional, clinical sequences. To obtain a better estimate of these measures, one could increase the sample size from 20 to about 200. Furthermore, it would be worthwhile to measure the sensitivities and specificities for detecting labral tears. With the current sample, all sequences exhibited 100% sensitivity for detecting labral tears; specificity could not be calculated. An increased sample size of around 200 would provide better estimates of these sensitivities and specificities.

3D Icones Trajectory

It is evident that the icones sampling pattern requires additional work to realize the goals for which it was designed. The impulse response for icones trajectories with nonzero skip values are characterized by a broad central lobe and concentric “rings” of aliased energy (**Figure 33**) emanating from the central pixel, whereas the impulse response of the 3D-PR trajectory is characterized by a narrow central lobe with a spherical, alias-free region that covers the central 1/2 FOV. It is possible that the current method for pairing the anchor points in k-space can be improved, since the typical icones petal after rotation has a width that is only about half that of the base icones petal (**Table 2**). Perhaps an alternative pairing scheme which allows the rotated icones petals to achieve the full width—or nearly the full width—of the base petal, would improve the impulse response.

Once the algorithm for the icones trajectory has been altered such that the base petal and method to rotate the petal through 3D space work in concert to create an improved impulse response function, the following experiments could be conducted:

(1) *In vivo* measurements of reduced undersampling with comparison to out-and-back, 3D-PR

This effort would center on comparing the undersampling produced by icones and out-and-back, 3D-PR at comparable scan times but with an icones sampling pattern that is designed to be 30% less undersampled than out-and-back, 3D-PR. To measure reduced undersampling artifact of the icones trajectory with respect to the out-and-back 3D radial trajectory, one would utilize the image data sets from repeated, 5-minute axial scans of a brain using each trajectory as an SPGR acquisition with 0.5mm isotropic resolution. Data from each sequence would be acquired twice using a single channel head coil to provide a somewhat homogeneous coil sensitivity profile. The two trajectories would use nearly the same number of excitations, the same values for transmit and receive gain, and an adjusted reconstruction gain factor to account for any inherent differences in signal level from the two trajectories. By using a sufficiently large ROI residing within a region of the brain that exhibits homogenous signal intensity such as the ventricles, certain assumptions about the noise characteristics, trajectory aliasing patterns, and MR signal component would likely hold true within those ROIs and an estimate of the signal variance due to aliasing could be estimated for each trajectory.

(2) ATR hip cartilage study with healthy volunteers at 3.0T: icones vs 3D-PR

Utilizing icones within an ATR pulse sequence could potentially allow high resolution sampling of k-space to be performed more rapidly or with less undersampling than a simple out-and-back, 3D-PR trajectory while meeting the TR constraint of the ATR method. One could exploit these capabilities in assessing hip cartilage morphology and compare image quality to the out-and-back, 3D Radial-ATR trajectory. We would conduct a study on the hip joints of ten healthy volunteers using icones-ATR and other currently used MR sequences for studying the cartilage of the hip, including 3D-PR-ATR, T1-w FSE, and IDEAL-SPGR. Signal-to-noise measures of cartilage, synovial fluid, tendon, and bone will be recorded. Additionally, CNR between fluid & cartilage, fluid & tendon, fluid & bone, and fluid & muscle would be determined. Paired t-tests would be utilized to compare differences in SNR and CNR values between sequences. If these results are encouraging, the icones-ATR sequence may be utilized in future research studies of symptomatic patients undergoing MRA for suspected hip joint damage, including: cartilage lesions, labrum tears, tendon tears, and ligament tears.

[3] T1-w bilateral, non-contrast enhanced breast study with asymptomatic volunteers at 1.5T

The icones trajectory could be utilized in various T1 and T2-like implementations of bilateral volumetric breast imaging. A dual, half-echo icones-SPGR sequence with 0.8mm isotropic resolution would be compared to other currently used sequences for breast MRI examination, including 3D-PR-SPGR, and SPGR-IDEAL. Quantitative measures would include SNR and CNR comparisons to demonstrate whether icones provides reductions in undersampling artifacts.

References

[1] T. Cukur, D.G. Nishimura, Fat-water separation with alternating repetition time balanced SSFP, Magnetic resonance in medicine : official journal of the Society of Magnetic Resonance in Medicine / Society of Magnetic Resonance in Medicine, 60 (2008) 479-484.
[2] A.V. Barger, W.F. Block, Y. Toropov, T.M. Grist, C.A. Mistretta, Time-resolved contrast-enhanced imaging with isotropic resolution and broad coverage using an undersampled 3D projection trajectory, Magn Reson Med, 48 (2002) 297-305.
[3] M.A. Bernstein, K.F. King, X.J. Zhou, Handbook of MRI Pulse SEquences, 1st ed., Elsevier Academic Press, Boston, MA, 2004.
[4] S.B. Reeder, A.R. Pineda, Z. Wen, A. Shimakawa, H. Yu, J.H. Brittain, G.E. Gold, C.H. Beaulieu, N.J. Pelc, Iterative decomposition of water and fat with echo asymmetry and least-squares estimation (IDEAL): application with fast spin-echo imaging, Magn Reson Med, 54 (2005) 636-644.
[5] G.E. Gold, B.A. Hargreaves, S.B. Reeder, W.F. Block, R. Kijowski, S.S. Vasanawala, P.R. Kornaat, R. Bammer, R. Newbould, N.K. Bangerter, C.F. Beaulieu, Balanced SSFP imaging of the musculoskeletal system, Journal of magnetic resonance imaging : JMRI, 25 (2007) 270-278.
[6] R. Kijowski, A. Lu, W. Block, T. Grist, Evaluation of the articular cartilage of the knee joint with vastly undersampled isotropic projection reconstruction steady-state free precession imaging, Journal of magnetic resonance imaging : JMRI, 24 (2006) 168-175.
[7] S.B. Reeder, N.J. Pelc, M.T. Alley, G.E. Gold, Rapid MR imaging of articular cartilage with steady-state free precession and multipoint fat-water separation, AJR.American journal of roentgenology, 180 (2003) 357-362.
[8] S.S. Vasanawala, J.M. Pauly, D.G. Nishimura, Fluctuating equilibrium MRI, Magn Reson Med, 42 (1999) 876-883.
[9] S.S. Vasanawala, J.M. Pauly, D.G. Nishimura, Linear combination steady-state free precession MRI, Magnetic resonance in medicine : official journal of the Society of Magnetic Resonance in Medicine / Society of Magnetic Resonance in Medicine, 43 (2000) 82-90.
[10] H. Al Saleh, L. Hernandez, K.S. Lee, H.G. Rosas, W.F. Block, R. Kijowski, Rapid isotropic resolution cartilage assessment using radial alternating repetition time balanced steady-state free-precession imaging, J Magn Reson Imaging, (2013).
[11] C.J. Moran, E.K. Brodsky, L.H. Bancroft, S.B. Reeder, H. Yu, R. Kijowski, D. Engel, W.F. Block, High-resolution 3D radial bSSFP with IDEAL, Magn Reson Med, 71 (2014) 95-104.
[12] L. Hernandez, J.L. Klaers, W.F. Block, R. Kijowski, MultiPlanar Assessment of the Elbow Joint Using Isotropic Resolution VIPR-ATR Imaging, in: 19th Annual Meeting of the ISMRM, Montreal, Canada, 2011.
[13] J.L. Klaers, E. Brodsky, W. Block, R. Kijowski, High Resolution Cartilage and Whole Organ Knee Joint Assessment: 3D Radial Fat-Suppressed Alternating TR SSFP, in: 18th Annual Meeting of the ISMRM, Stockholm, Sweden, 2010.
[14] A. Lu, E. Brodsky, T.M. Grist, W.F. Block, Rapid fat-suppressed isotropic steady-state free precession imaging using true 3D multiple-half-echo projection reconstruction, Magn Reson Med, 53 (2005) 692-699.
[15] N.G. Papadakis, A.A. Wilkinson, T.A. Carpenter, L.D. Hall, A general method for measurement of the time integral of variant magnetic field gradients: application to 2D spiral imaging, Magn Reson Imaging, 15 (1997) 567-578.

[16] A. Moussavi, M. Untenberger, M. Uecker, J. Frahm, Correction of gradient-induced phase errors in radial MRI, Magn Reson Med, 71 (2014) 308-312.
[17] E.K. Brodsky, J.L. Klaers, A.A. Samsonov, R. Kijowski, W.F. Block, Rapid measurement and correction of phase errors from B0 eddy currents: impact on image quality for non-Cartesian imaging, Magn Reson Med, 69 (2013) 509-515.
[18] J.H. Duyn, Y. Yang, J.A. Frank, J.W. van der Veen, Simple correction method for k-space trajectory deviations in MRI, J Magn Reson, 132 (1998) 150-153.
[19] P. Gurney, J. Pauly, D.G. Nishimura, A Simple Method for Measuring B0 Eddy Currents, in: 13th Annual Meeting of ISMRM, Miami, FL, 2005, pp. 866.
[20] H.T. Nielsen, E.W. Olcott, D.G. Nishimura, Improved 2D time-of-flight angiography using a radial-line k-space acquisition, Magn Reson Med, 37 (1997) 285-291.
[21] C.B. Ahn, J.H. Kim, Z.H. Cho, High-speed spiral-scan echo planar NMR imaging-I, IEEE Trans Med Imaging, 5 (1986) 2-7.
[22] D.C. Noll, Multishot rosette trajectories for spectrally selective MR imaging, IEEE Trans Med Imaging, 16 (1997) 372-377.
[23] F.E. Boada, J.S. Gillen, G.X. Shen, S.Y. Chang, K.R. Thulborn, Fast three dimensional sodium imaging, Magn Reson Med, 37 (1997) 706-715.
[24] E.K. Bucholz, J. Song, G.A. Johnson, I. Hancu, Multispectral imaging with three-dimensional rosette trajectories, Magn Reson Med, 59 (2008) 581-589.
[25] I. Zaltz, B.T. Kelly, C.M. Larson, M. Leunig, A. Bedi, Surgical treatment of femoroacetabular impingement: what are the limits of hip arthroscopy?, Arthroscopy, 30 (2014) 99-110.
[26] B. Bittersohl, H.S. Hosalkar, T. Hesper, C.J. Tiderius, C. Zilkens, R. Krauspe, Advanced Imaging in Femoroacetabular Impingement: Current State and Future Prospects, Front Surg, 2 (2015) 34.
[27] A.E. Li, S.T. Jawetz, H.G.t. Greditzer, A.J. Burge, D.H. Nawabi, H.G. Potter, MRI for the preoperative evaluation of femoroacetabular impingement, Insights Imaging, 7 (2016) 187-198.
[28] M.A. Bredella, E.J. Ulbrich, D.W. Stoller, S.E. Anderson, Femoroacetabular impingement, Magn Reson Imaging Clin N Am, 21 (2013) 45-64.
[29] R.J. Macfarlane, F.S. Haddad, The diagnosis and management of femoro-acetabular impingement, Ann R Coll Surg Engl, 92 (2010) 363-367.
[30] T.C. Mamisch, C. Zilkens, K.A. Siebenrock, B. Bittersohl, Y.J. Kim, S. Werlen, MRI of hip osteoarthritis and implications for surgery, in: Magn Reson Imaging Clin N Am, United States, 2010, pp. 111-120.
[31] C.N. Petchprapa, K.S. Dunham, R. Lattanzi, M.P. Recht, Demystifying radial imaging of the hip, in: Radiographics, Rsna, 2013., United States, 2013, pp. E97-E112.
[32] K.S. Rakhra, A.M. Sheikh, D. Allen, P.E. Beaule, Comparison of MRI alpha angle measurement planes in femoroacetabular impingement, Clin Orthop Relat Res, 467 (2009) 660-665.
[33] P.R. Knuesel, C.W. Pfirrmann, H.P. Noetzli, C. Dora, M. Zanetti, J. Hodler, B. Kuehn, M.R. Schmid, MR arthrography of the hip: diagnostic performance of a dedicated water-excitation 3D double-echo steady-state sequence to detect cartilage lesions, in: AJR Am J Roentgenol, United States, 2004, pp. 1729-1735.
[34] D.G. Blankenbaker, S.R. Ullrick, R. Kijowski, K.W. Davis, A.A. De Smet, K. Shinki, A. Munoz del Rio, J.S. Keene, MR arthrography of the hip: comparison of IDEAL-SPGR volume

sequence to standard MR sequences in the detection and grading of cartilage lesions, Radiology, 261 (2011) 863-871.
[35] J.C. McCarthy, P.J. Glassner, Correlation of magnetic resonance arthrography with revision hip arthroscopy, Clin Orthop Relat Res, 471 (2013) 4006-4011.
[36] T. Magee, Comparison of 3.0-T MR vs 3.0-T MR arthrography of the hip for detection of acetabular labral tears and chondral defects in the same patient population, Br J Radiol, 88 (2015) 20140817.
[37] C.P. Ho, N.D. Ommen, S. Bhatia, A.J. Saroki, P. Goljan, K.K. Briggs, M.J. Philippon, Predictive Value of 3-T Magnetic Resonance Imaging in Diagnosing Grade 3 and 4 Chondral Lesions in the Hip, Arthroscopy, (2016).
[38] R. Sutter, V. Zubler, A. Hoffmann, N. Mamisch-Saupe, C. Dora, F. Kalberer, M. Zanetti, J. Hodler, C.W. Pfirrmann, Hip MRI: how useful is intraarticular contrast material for evaluating surgically proven lesions of the labrum and articular cartilage?, AJR Am J Roentgenol, 202 (2014) 160-169.
[39] J. Leupold, J. Hennig, K. Scheffler, Alternating repetition time balanced steady state free precession, Magnetic resonance in medicine : official journal of the Society of Magnetic Resonance in Medicine / Society of Magnetic Resonance in Medicine, 55 (2006) 557-565.
[40] K.M. Friedrich, G. Reiter, B. Kaiser, M. Mayerhofer, M. Deimling, V. Jellus, W. Horger, S. Trattnig, M. Schweitzer, E. Salomonowitz, High-resolution cartilage imaging of the knee at 3T: basic evaluation of modern isotropic 3D MR-sequences, European Journal of Radiology, 78 (2011) 398-405.
[41] J. Carballido-Gamio, T.M. Link, X. Li, E.T. Han, R. Krug, M.D. Ries, S. Majumdar, Feasibility and reproducibility of relaxometry, morphometric, and geometrical measurements of the hip joint with magnetic resonance imaging at 3T, J Magn Reson Imaging, 28 (2008) 227-235.
[42] S.T. Wong, M.S. Roos, A strategy for sampling on a sphere applied to 3D selective RF pulse design, Magn Reson Med, 32 (1994) 778-784.
[43] N.R. Zwart, K.O. Johnson, J.G. Pipe, Efficient sample density estimation by combining gridding and an optimized kernel, Magn Reson Med, 67 (2012) 701-710.
[44] J.G. Pipe, P. Menon, Sampling density compensation in MRI: rationale and an iterative numerical solution, Magn Reson Med, 41 (1999) 179-186.
[45] K.O. Johnson, J.G. Pipe, Convolution kernel design and efficient algorithm for sampling density correction, Magn Reson Med, 61 (2009) 439-447.
[46] N.O. Addy, H.H. Wu, D.G. Nishimura, Simple method for MR gradient system characterization and k-space trajectory estimation, Magn Reson Med, 68 (2012) 120-129.